Material Transfer Associated with the Contact Between Polymer and Silicon Surfaces

by

Nandini Iyer

B.Eng., Mechanical Engineering, University of Bath, 1996

Submitted to the Department of Mechanical Engineering
in Partial Fulfillment of the Requirements for the Degree of

MASTER OF SCIENCE IN MECHANICAL ENGINEERING

at the

MASSACHUSETTS INSTITUTE OF TECHNOLOGY

June 1998

/

Author: _____

Department of Mechanical Engineering
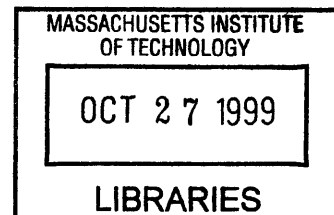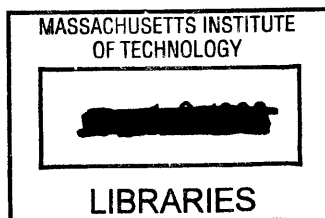May 8, 1998

Certified by: _____

Nannaji Saka
Principal Research Scientist and Lecturer
Thesis Supervisor

Certified by: _____

Jung-Hoon Chun
Associate Professor of Mechanical Engineering
Thesis Supervisor

Accepted by: _____

Ain A. Sonin
Chairman, Department Graduate Committee

Material Transfer Associated with the Contact Between Polymer and Silicon Surfaces

by

Nandini Iyer

Abstract

Material transfer due to the contact of surfaces is encountered in a wide variety of engineering applications. One of these is the backside contamination of silicon wafers due to contact with polymer vacuum chucks during spin coating. The present research investigates material transfer associated with this contact. The contact between the silicon wafer and the vacuum chuck was idealized as pin-on-flat interaction and an experimental apparatus was fabricated based on this model. Material transfer from a variety of solid polymers (UHMWPE, Teflon, KEL-F, PMMA, PEEK, and Nylon 66) was studied and characterized by Scanning Electron Microscopy, Atomic Force Microscopy, Optical Microscopy and computer image analysis. This was augmented with studies of material transfer from polymeric films (Polyethylene, Teflon, and Kapton) and ceramics (quartz, sapphire and ruby).

The variables of interest for the material transfer phenomenon were identified using analysis of elastic contacts (Hertzian) and adhesion. Experimental results suggest that the material transfer was affected by the contact area that forms between the polymer and the silicon substrate and by the contact pressure at the surface asperities. At low loads, contact area and pressure decreases causing less transfer. There is a linear relationship between the total particle area and the Hertzian contact area. For elastic contacts, the effect of surface roughness is not pronounced. Friction and surface energy also appear to be weak variables in the material transfer phenomenon. The Young's moduli of the polymers also affect material transfer. The number of particles transferred and the total particle area decreased with an increase in Young's modulus. No material transfer was observed with Kapton, quartz, sapphire and ruby. Material transfer was also inhibited with the use of a small amount of lubricant.

Thesis Supervisor: Nannaji Saka
Title: Principal Research Scientist and Lecturer

Thesis Supervisor: Jung-Hoon Chun
Title: Associate Professor of Mechanical Engineering

Acknowledgments

Contents

5

List of Figures

List of Tables

Chapter 1

Introduction

Touching one solid surface by another can result in material transfer from one of the surfaces to the other. This material transfer phenomenon is often neglected in standard theoretical treatments of nominal contact between solid bodies. This practice is justified by the assumption that the forces acting at the interface are too weak to cause a separation of material from one solid body to the other. Evidence of material transfer after contact between two surfaces indicates, however, that this assertion breaks down at some point. The study of the details of the geometry and the mechanics of the contacting surfaces that includes surface forces at the appropriate scale may determine how and when material transfer occurs.

Material transfer due to contact is encountered in a wide variety of engineering applications. For example, surface contamination because of material transfer is critical in the semiconductor manufacturing industry [Parks, O'Hanlon, 1967]. The contact of silicon wafers with fixtures and mechanical handling devices in particular, results in material transfer on to the silicon surface [Bowling and Davis, 1994; Moinpour, et al., 1995]. The phrase coined to refer to this problem is "backside contamination", where backside refers to the unpolished surface of the silicon waer that comes in contact with the fixture.

1.1 Surface Contamination During Spin Coating

One of the manufacturing areas where backside contamination is prevalent is during the spin coating operation. The spin coating operation is a part of the microlithography process for constructing three- dimensional microelectronic devices. The silicon wafers that are used in semiconductor manufacturing are repeatedly spin coated with a photoresist film, about one micrometer thick. This film is used to produce the desired microelectronic circuit geometry. This is done by irradiating the film through a mask that contains the desired pattern. The radiation beam can be electrons, photons, ultraviolet or x-rays. This process of applying the photoresist coating and imaging the desired feature is repeated until the required number of layers has been

12

formed.

During this process, the wafers (200 mm in diameter) are held by vacuum chucks made of Polymeric materials on the backside (unpolished side) while the photoresist film, which is composed of a polymer base, photosensitizer and solvent, is applied onto the polished side. It has been observed that the vacuum chuck contaminates the silicon wafers. Micrometer sized polymer particles have been detected on the backside of the silicon wafers. This is attributed to the material transfer from the chuck to the silicon wafer due to the contact between the surfaces.

This particulate contamination on the silicon wafer is unacceptable for it introduces defects in the manufacture of microelectronic devices. The semiconductor industry is continuously striving to design smaller, more efficient devices with tighter tolerances. As the design rule shifts from 0.80 μm to 0.35 μm line-width, stringent requirements are being placed on the size and coverage of the contaminant particles.

1.2   The Spin Coating Operation
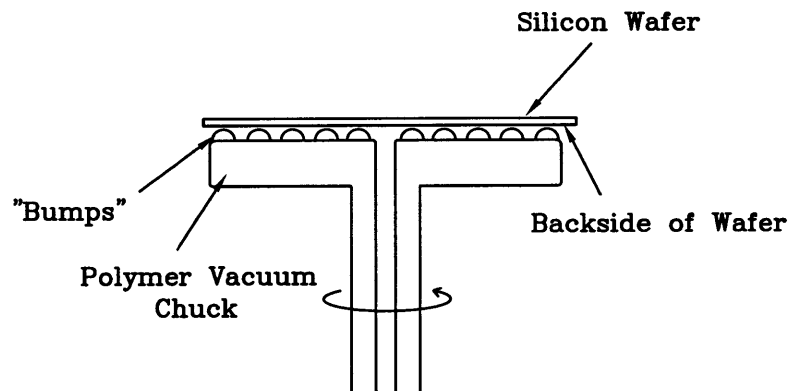
Figure 1-1: Schematic of the spin coating operation.

The vacuum chuck that is used in the spin coating operation is covered with "bumps" (Figure 1-1). The silicon wafer rests on these bumps during spin coating. Satisfactory coating is achieved under the following operating conditions.

- Spin chuck fabricated from a chemically inert material. Hence most metals cannot be used for the vacuum chuck.

- The distribution of the normal force on the wafer must be uniform so that the wafers it is held flat and firm.

- Vacuum must be sustained for all values of spin speeds and accelerations. The maximum spin speed of the chuck can be up to 7,500 rpm and maximum acceleration of the chuck up to 30,000 rpm/s^2.

Calculations have been carried out to estimate the forces on the vacuum chuck during the spin coating operation. The dimensions of the chuck and the number and geometry of the bumps were measured on a prototype chuck. The total normal force is estimated to be 235 N. The number of bumps is about 870. Hence, the force on each bump, for uniform distribution of the normal load, is 0.27 N (27 g). Realistically, however, there may be an unequal distribution of forces on the chuck and some of the bumps may be loaded more heavily than the others.

1.3   Effects of Contamination

To ensure satisfactory transfer of the mask pattern on the photoresist film, there must be uniformity in the thickness of the photoresist film so that a constant level of exposure can be obtained across the wafer during imaging. There must be no local or global deviations in the depth of focus during the imaging process. Any non-uniformity can result in a loss of optical stepper control when alignment marks are being sensed beneath the photoresist film, and non-uniformity also affects the reflectivity of the photoresist film [Derksen, 1997]. Due to backside contamination, the silicon wafer is prevented from from resting completely flat during the transfer of the mask pattern onto the photoresist. Consequently, the thickness of the photoresist coating on the wafer appears non-uniform.

Contamination of the backside of the silicon wafer therefore results in the production of defective microelectronic devices. This decreases productivity, increases downtime and produces undesirable scrap. The present limits for backside contamination are specified to be fewer than 200 particles of size greater than $0.2 \mu m$ on a 200 mm silicon wafer.

1.4   Backside Contamination in Industry

In view of the increasing demand for higher performance microelectronic devices, attempts have been made to eliminate, if not, at least reduce, the levels of contamination encountered. Backside contamination is attributed to the adhesion of particles on the silicon wafer [Ranade, 1987]. It is speculated that molecular interactions, Van der Waals forces and electrostatic forces may be responsible. Because the exact nature of the material transfer phenomenon remains unknown, attempts to control backside contamination have been focused on identification and characterization of the contaminants using analytical techniques such as Scanning Electron Microscopy (SEM), Atomic Force Microscopy (AFM) and X-Ray Photoelectron Spectroscopy (SAXPS) have been employed. In some cases, molecular analysis of the contaminants has been carried out using Fourier Transform Infrared Microspectroscopy (FTIR) and Secondary Ion Mass Spectroscopy (SIMS). Once the source of contamination has been identified, attempts are made to improve the particular manufacturing processes that contribute to backside contamination.

Wafer chucks and handlers were investigated for the release of particulate matter and metallic contamination on to the backside of silicon wafers [Kroninger, et al., 1993]. Electrolytic Metal Tracer (ELYMAT) measurements showed an identical imprint of the chuck on the backside of the wafer. The metallic impurities on the wafer have been analyzed by Total Reflection X-Ray Fluorescence Spectroscopy (TXRF) and by Atomic Absorption Spectroscopy (AAS) after vapor phase decomposition of the surface oxide. A similar study was carried out by researches at Intel [Moinpour, et al., 1995]. Two cases of backside contamination were studied; one involving tungsten deposition while the wafer rested on a chuck during wafer coating, and the other during the transportation of wafers on a moving belt. The two case studies demonstrated that backside contamination contributed to depressed yield, increased equipment downtime, and to the allocation of considerable resources to understand and characterize the contamination mechanism.

Steps have been taken to eliminate backside contamination by minimizing the contact of wafers with fixtures [Ranade, 1987]. Mechanical equipment and processes were so redesigned that the level of mechanical wafer handling was reduced. For example, the vacuum chuck used for spin coating is covered with bumps on which the silicon wafer rests. This is a redesign of the previous chuck where silicon wafer rested on a the flat face of the polymer chuck.

Several reviews on the evolving role of defects and contamination in semiconductor manufacturing have been carried out. The cleaning procedures used in the semiconductor manufacturing industry is reviewed by Parks and O'Hanlon (1993). At present, wet chemistries are utilized for cleaning, and this has the effect of promoting the formation of oxide in the areas that are being cleaned. Accordingly, dry cleaning measures are being investigated such as the use of anhydrous hydrogen fluoride and hydrogen fluoride vapor. Also, the use of etching techniques to replace wet processes are being investigated. However, this cannot successfully remove heavy metal contamination. Other methods of cleaning proposed are shock waves and argon ice cleaning. Despite these investigations into the different types of cleaning mechanisms, the authors make clear that eliminating contamination is the best way to increase productivity and yield. Contaminant-Free Manufacturing (CFM) is the technology that emphasizes the importance of controlling, if not mitigating, contamination during semiconductor manufacturing [Bowling and Davis, 1994]. Areas of interest for contamination control are storage of silicon wafers, transportation of wafers to processing sites and wafer processing equipment. While attempts to mitigate backside contamination have successfully reduced the level of contamination, the problem still remains, and the levels of contamination currently encountered in industry are above the acceptable limits.

1.5 Problem Statement

At present, the material transfer associated with two solid bodies in contact is not well understood. This is the primary shortcoming for successful mitigation procedures. An understanding of the mechanics of the contact between the surfaces and the nature of the attractive forces is required before further attempts are made to minimize backside contamination. The objective of this research is to study the material transfer associated with the contact of polymer and silicon surfaces. The task is to identify the variables of interest that affect material transfer and discover any trends. These parameters are identified using the theory of contact mechanics and adhesion.

The material transfer between the polymer vacuum chuck and silicon wafer is idealized as a classic pin-on-flat interaction (Figure 1-2). The contact between a 200 mm silicon wafer and the vacuum chuck is reduced to that between a polymer pin and a silicon substrate. This simulates a single wafer contact site which is that between a single bump on the vacuum chuck and the silicon wafer. Experimental studies of the material transfer from different polymers were carried out and the transferred fragments have been analyzed using analytical techniques such as optical microscopy, Scanning Electron Microscopy (SEM) and Atomic Force Microscopy (AFM). Finally, with the understanding obtained from the experimental work, mitigation procedures have been proposed and tested. The results of this research do not exclusively hold for interactions between polymer and silicon surfaces, but for all solid surfaces that come in nominal contact and result in material transfer.
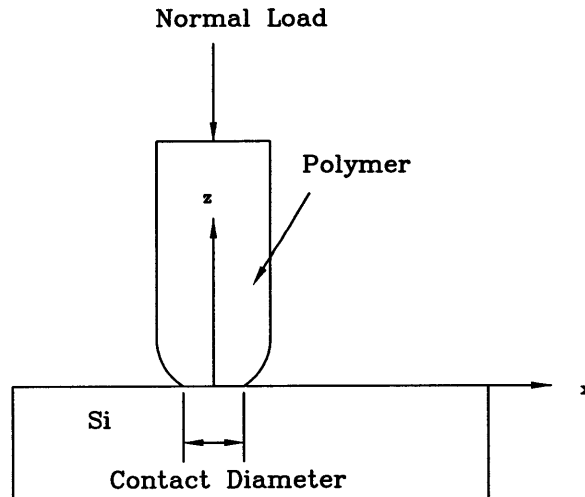
Figure 1-2: Pin-on-flat idealization of contact between polymer and silicon.

1.6 Thesis Organization

This introductory chapter is followed by *Chapter 2*, in which the theoretical framework used in this research is presented. These are the Hertzian elastic contact theory and adhesion. In *Chapter 3*, a description of the experimental methods used is provided, and the variables that affect the material transfer phenomenon are stated. The preliminary experimental results that characterize the material transfer are contained in *Chapter 4*. Video images of the contact area and material transfer are presented. The results obtained from SEM and AFM are also presented. In *Chapter 5*, the experimental results and trends identified by studying the parametric space are presented. The effect of load, surface energy, surface roughness, friction, Young's moduli and hardness are shown. This is followed by *Chapter 6* in which the proposed mitigation procedures are presented. Results from experiments with polymeric films such as Polyetylene, Teflon and Kapton are shown. Also, results from the use of ceramics is shown. The effect of using a small amount of lubricant on the material transfer phenomenon is presented. Finally, in *Chapter 7*, the conclusions arrived at as a result of this research are presented.

Chapter 2

Theoretical Framework

When two bodies touch, a contact is formed. The shape and size of the contact are characterized by the load applied, the geometry of the contacting bodies, surface topography, and the physical properties of the materials in contact. This branch of study is called contact mechanics.

In this chapter, the theoretical concepts that are used to model the material transfer phenomenon are presented. The topics covered include Hertzian elastic contacts, the effects of friction and surface roughness on the elastic contact, and adhesion. The variables of interest that govern material transfer are identified and presented at the end of this chapter.

2.1 Hertzian Elastic Contact

The contact between two smooth elastic bodies was investigated by Heinrich Hertz [Hertz, 1882; Timoshenko and Goodier, 1951]. He demonstrated that the size and shape of the contact zone is governed by elastic deformation of the bodies. A complete set of equations that determines the size and shape of the contact zone, and the stresses at the contact and in the interior of the bodies during nominal contact was formulated (Figure 2-1). Hertz himself verified the equations experimentally by measuring the contact area between two glass spheres under normal load using an optical microscope. The experimental values were found to be in close agreement with those calculated by Hertzian analysis.

For two spheres of radii R_1 and R_2 pressed together by a normal load N, the Hertzian contact radius, a, is given by

$$a = \left(\frac{3NR}{4E^*}\right)^{\frac{1}{3}},\tag{2.1}$$

where

18
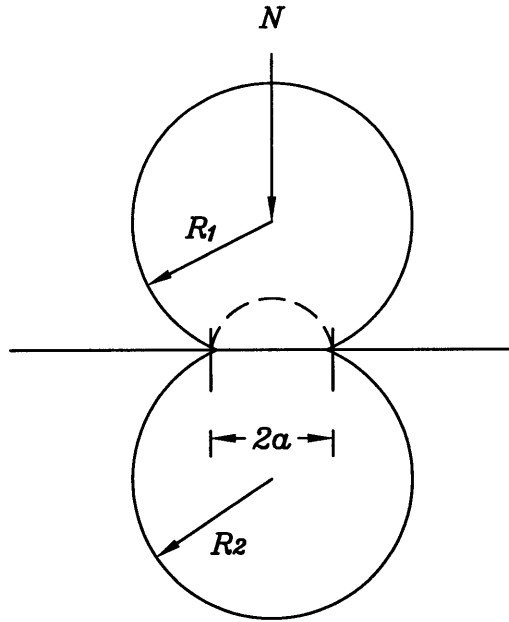
- - - - p, **Hertzian pressure distribution**

Figure 2-1: Hertzian elastic contact between two smooth, frictionless bodies.

$$\frac{1}{E^*} = \frac{1 - \nu_1^2}{E_1} + \frac{1 - \nu_2^2}{E_2},$$

and

$$\frac{1}{R} = \frac{1}{R_1} + \frac{1}{R_2}.$$

Here, E_1 and E_2 are the Young's moduli of the materials of the spheres and ν_1 and ν_2 are the Poisson's ratios. For a sphere on flat geometry, $R = R_1$ and $R_2 = \infty$.

The maximum Hertzian contact pressure p_0 is given by

$$p_0 = \frac{3}{2} \cdot \frac{N}{\pi a^2}. \tag{2.2}$$

The maximum value of shear stress τ_{MAX} may be written as

$$\tau_{MAX} = 0.31 p_0,$$

which occurs at $r = 0$ and $z = 0.48a$.

19

The key assumptions of this theory are that the contact is frictionless and that the contacting surfaces are smooth. Realistically, contacting surfaces may be rough and subject to interfacial friction. The Hertz analysis must therefore be extended to include the effects of friction and surface roughness.

2.2 Elastic Contact with Friction and Surface Roughness

Goodman (1962) extended the Hertzian equations to include the effect of friction at the interface of the elastic contact. When contact occurs between elastically dissimilar materials, the difference in the tangential displacements of the surface, causes microscopic slip. This occurs in a narrow annulus at the edge of the contact region. However, if the coefficient of friction between the two bodies is large enough, slip can be prevented. Where there is slip, the tangential traction q is related to the normal pressure p by

$$q = |\mu p|. \tag{2.3}$$

For small values of μ, the tangential traction is larger. The direction of q opposes the direction of slip. For surfaces with small friction coefficients, the tangential traction is not large enough to prevent slip. Material transfer in the form of wear particles may occur in the slip regions.

When the contacting surfaces are rough, contact occurs at a number of discrete asperities (Figure 2-2). The behavior of rough surfaces is determined primarily by the statistical distribution of asperity heights and secondarily by their mode of deformation; elastic or elastoplastic. The contact of rough surfaces has been investigated by Greenwood and Williamson (1966) and Greenwood and Tripp (1967).
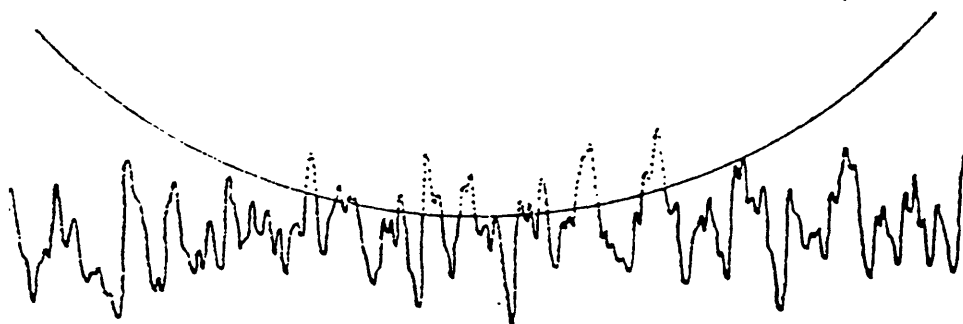
Figure 2-2: Schematic of the contact between a rough flat and a smooth sphere. Contact occurs at the tips of the asperities [Greenwood and Tripp, 1967].

In the Greenwood-Williamson (1966), the contact between rough surfaces is frequently plastic. The real area of contact is the sum of the areas of the individual asperity contacts which undergo plastic deformation. The overall stresses in the body fall within the elastic range but the local stresses at the contacting asperities cause plastic deformation.

In the Greenwood-Tripp model it is assumed that the tips of the asperities are spherical and that the they deform elastically. The latter assumption is reconciled with the Greenwood-Williamson model with the following argument. As the behavior of rough surfaces depends more on the statistical distribution of heights rather than on the mode of deformation, pure plastic deformation of the asperity tips would introduce no new features. The Greenwood-Tripp model is still valid even if some of the asperities on the surface undergo plastic deformation.

For a given load, surface roughness increases the contact radius compared with that calculated using Hertzian analysis. Consequently, the maximum contact pressure is smaller than that estimated using Hertzian analysis. An effective contact radius, a^* and pressure $p(r)$ which include parameters that characterize the topography of the rough surfaces are defined. The distribution of the asperity heights, the density of the asperities and the curvature of the asperities must be known *a priori* to calculate a^* and $p(r)$.

However, Hertzian elastic contact can still be used for rough surfaces with a small error if the nondimensional roughness parameter , α, is less than about 0.05 [Johnson, 1985]. The parameter α depends on the topography of the surfaces, the load and the elastic constants of the materials. It is expressed by

$$\alpha = \theta_S \left(\frac{16RE^{*2}}{9N^2} \right)^{\frac{1}{3}} .$$ (2.4)

where θ_S is the standard deviation of the asperity heights. Since the parameter α decreases with an increases in load it is found that Hertzian results are valid for high loads, but for low loads the effective pressure $p(r)$ is much lower than the Herzian. Figure 2-3 compares the differences in the pressure distribution for contact between rough surfaces. However, at very large loads, the Hertzian analysis breaks down as plastic deformation is initiated.

Plastic yielding at the contact occurs when the stresses in the body exceed the yield point of the softer material. The criterion that determines the onset of plastic yielding is the shear strength, τ_Y. When the maximum shear stress, τ_{MAX}, exceeds the shear strength of the softer material, plastic flow takes place. The shear strength, τ_Y is approximated by

$$\tau_Y = \frac{\sigma_Y}{2},$$

21

where σ_Y is

$$\sigma_Y = \frac{H}{3}.$$

σ_Y and H, respectively, are the tensile yield strength and hardness of the material.
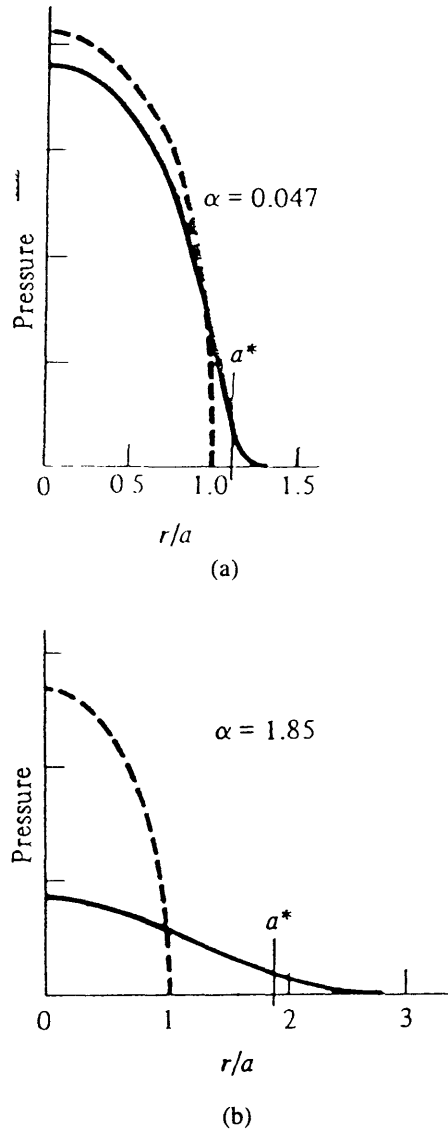
Figure 2-3: Influence of surface roughness on the pressure distribution. - - - Hertzian pressure distribution. (a) At high loads pressure distribution agrees well with Hertzian. (b) At low loads pressures are much lower than Hertzian and spread over a larger area. a^* is the effective contact radius [Johnson, 1985].

2.3 Adhesion
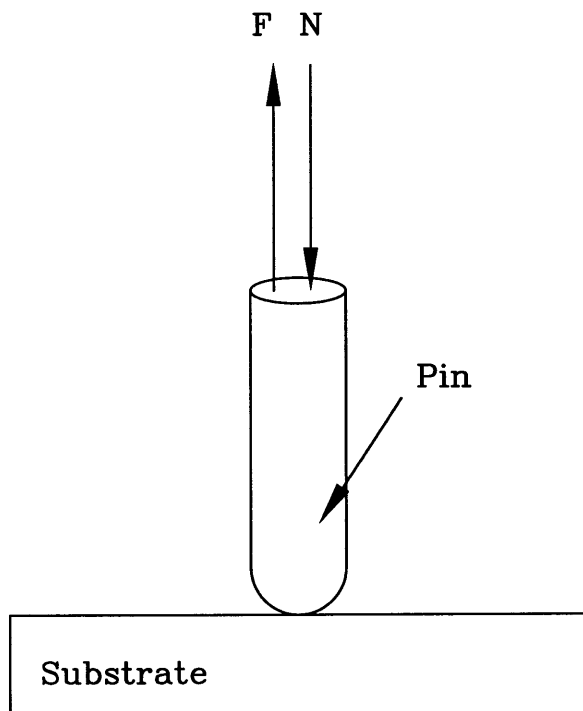
Figure 2-4: Adhesion between pin pressed on flat, pressed together with load N. A tensile force, F is required to separate the contacting surfaces.

After two surfaces are pressed together, a tensile force is required to separate these surfaces. This is the force of adhesion (Figure 2-4). Bowden and Tabor (1950) used the concept of "adhesion" to explain friction. It was proposed that the asperities of two bodies that are in contact form junctions. Frictional force, therefore, was postulated to be the force required to shear these junctions as one body slides over the other. In later years, developments in contact mechanics suggested other theories for friction.

Attempts have been made to measure the force of adhesion. The force of adhesion measured by Tomlinson (1928) between two glass spheres of radius 2.5 mm was reported as being 3.6×10^{-3} N. Krupp (1967) reports a value of 2.23×10^{-6} N for the force of adhesion between a gold sphere of radius 3 μm and a plastic film. Even at large values of the radius of curvature, the force of adhesion is low. For instance, Tabor (1977) reports that the force of adhesion measured between a rubber sphere of radius 2.2 cm pressed against a rubber flat was about 5.4×10^{-3} N. The adhesive force in most cases is small and it is assumed that this force cannot cause a separation of material from one body to another.

The Hertz model for elastic contact was modified to account for adhesion. Interaction between the surfaces due to differences in surface energy was included in

the Hertz analysis to account for the deviations in contact radius and stresses due to adhesion (Figure 2-5) [Johnson, Kendall, and Roberts, (JKR), 1971].
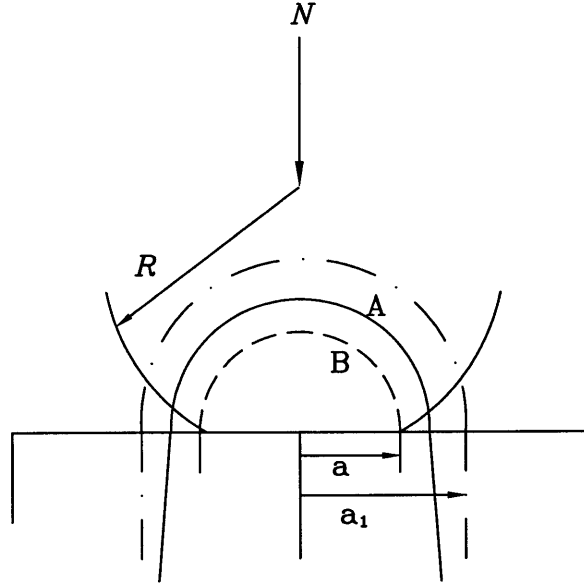
Figure 2-5: Contact between two smooth elastic solids - JKR Theory. A is the Hertzian stress and distribution B is that obtained with the modified JKR equations.

The surface energy interaction produces a contact radius, a_1, which is give by

$$a_1 = \frac{3R}{4E^*} \left(N + 3\pi\gamma R + \sqrt{6\pi\gamma N R + (3\pi\gamma R)^2} \right), \qquad (2.5)$$

where

$$\gamma = \gamma_p + \gamma_{Si} - \gamma_{p/Si}.$$

The terms γ_p, γ_{Si}, and $\gamma_{p/Si}$ refer to the surface energies of polymer, silicon, and the interfacial energy between polymer and silicon, respectively.

The JKR theory predicts that for a given normal load N, the contact radius formed is larger than that predicted by Hertzian. This increase is attributed to the attraction between the surfaces due to surface energy interactions. The effect on the contact radius due to the surface energy term is similar to that of increasing the normal load, N. When $\gamma = 0$, the relationship for the contact radius given above (Equation 2.5) reverts to that given by Hertzian analysis (Equation 2.1). Figure 2-6 compares the contact radius as calculated by Hertzian analysis with that by JKR theory. The JKR theory predicts that even when the normal load, N, is zero, there is still contact between the surfaces. Using Equation 2.5, when $N = 0, a_1 \neq 0$. This is attributed to the attraction between the surfaces.

The force of adhesion , F, required to separate the surfaces is given by
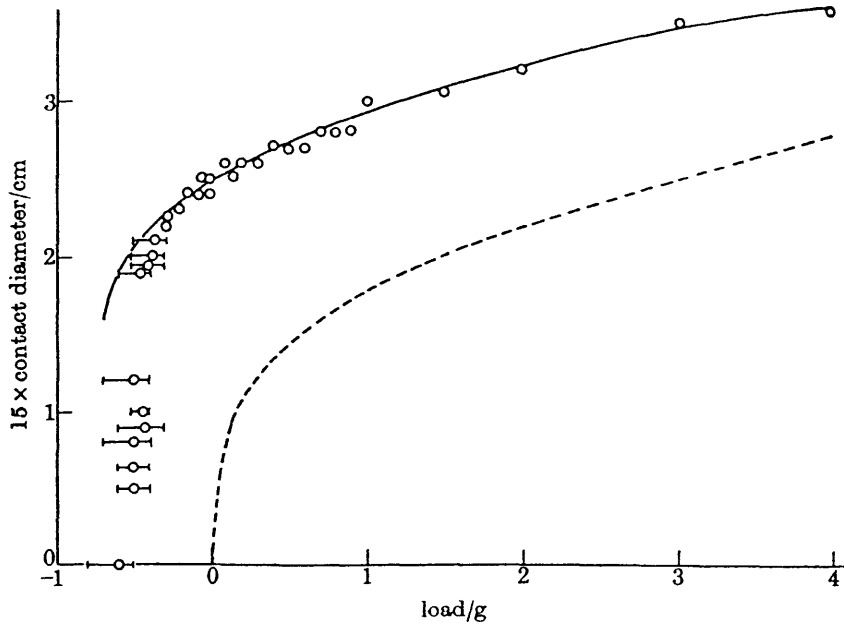
Figure 2-6: Contact radii calculated using Hertzian analysis and JKR theory. Results are for a rubber sphere ($R = 2.2$ cm) in contact with rubber flat. - - - , Hertz theory; ——, JKR theory. [Johnson et al., 1971]

$$F = -\frac{3}{2} \cdot \pi\gamma R. \tag{2.6}$$

The force of adhesion is dependent only on the geometry of the contacting surfaces and the surface energy term.

Further investigations on adhesion have indicated that the force of adhesion varied with temperature and humidity [Krupp, 1967; Ketkar, et al., 1975]. The effects of friction and surface roughness, too, have been investigated [Savkoor et al., 1977; Tabor, 1977]. In both cases, it was found that adhesion is most prominent when the contacting surfaces are smooth and have low frction. This is because the force of adhesion is easily "masked" by friction and surface roughness. The surface energy of solids varies with temperature and humidity. Hence variations in temperature and humidity could cause variations in the force of adhesion between two solid bodies.

2.4　Variables of Interest

The theoretical framework outlined above is used to set the variables that may be responsible for the material transfer that occurs at the the contact between two solids, polymer and silicon, in the case of backside contamination. It is postulated that the contact consists of two stages. First, formation of a contact area with the relevant stress and second, attraction of particles from the chuck to the wafer. Hence, the parameters that govern the problem are those that affect both stages. The variables of interest in the problem of backside contamination during the spin coating process may be listed as:

- Normal Load (N)

- Radius of Curvature (R)

- Young's Modulus (E)

- Tensile Yield Strength (σ_Y) or Hardness (H)

- Surface Energy (γ)

- Friction Coefficient (μ)

- Surface Roughness (R_a)

- Humidity ($H\%$)

- Temperature (T)

Chapter 3

Experimental Methods

This chapter provides a description of the experimental apparatus, the materials tested, and the experimental procedure adopted in this investigation. It also includes details of the image processing and data analysis that have been carried out.

3.1 Apparatus

The apparatus was modeled after a standard Tribology pin-on-flat friction tester. It simulates the contact between a bump on the vacuum chuck and the silicon wafer. The material transfer associated with the contact between these surfaces was reproduced by the application of normal load on a polymer pin. The polymer pin was held by a holder in a loading arm. The pin made contact with a silicon substrate when the arm was loaded normally. Removal of the normal load caused the loading arm to swing back to its initial position, thereby breaking the contact between the polymer pin and the silicon substrate. The application and removal of the normal load on the arm was done using a motorized vertical slider mechanism. After the contact was broken, the transferred material was observed by an optical microscope. The image of the polymer particles on the surface of the silicon was captured by a CCD camera (Techni-Quip) that interfaced with a computer via a framegrabber card (FlashPoint 128). The captured CCD image was then analyzed using an appropriate image analysis software (Image ProPlus 2 Series 3.1).

The temperature and humidity of the environment during experimentation was measured by a panel mounted temperature/humidity sensor (OMEGA RHCN-1). The experimental apparatus was housed inside a vertical laminar flow hood (Series 412 Clean Air Products). The HEPA filter in the hood is 99.99% efficient for trapping particles of size 0.3 μm and larger. This maintained a clean, contaminant free environment in which the experiments were carried out. The schematic of the apparatus is shown Figure 3-1. A magnified schematic of the pin holder and silicon substrate is depicted in Figure 3-2. Figure 3-3 is a photograph of the facility.
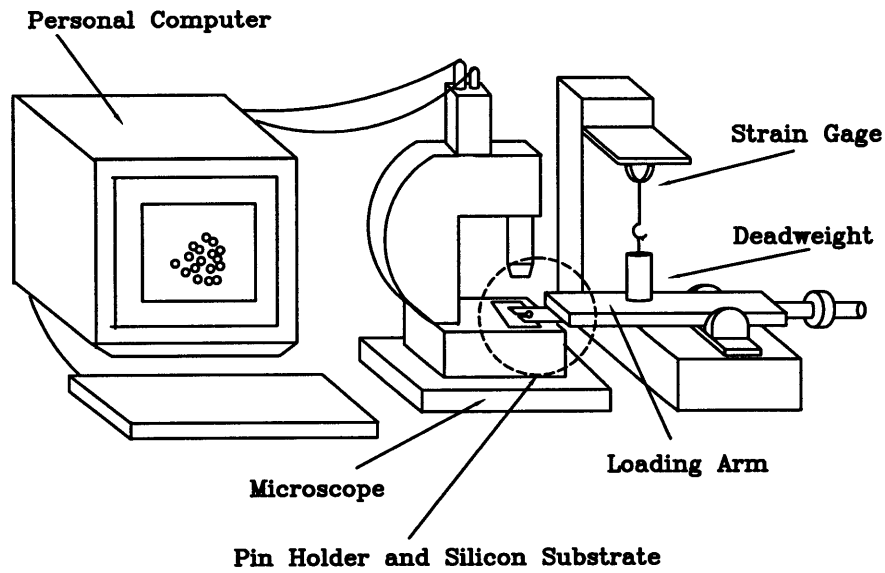
Figure 3-1: Schematic of the backside contamination experimental facility.
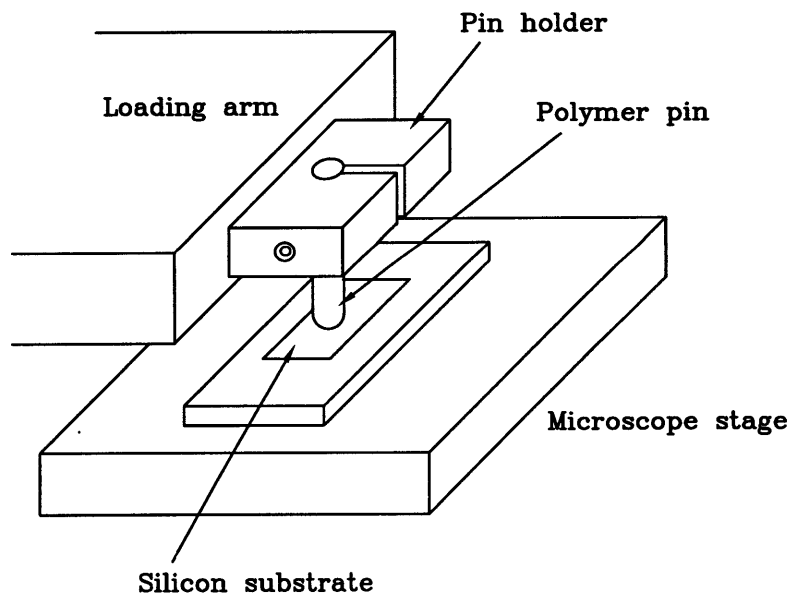
Figure 3-2: Schematic of pin holder, polymer pin and silicon substrate.
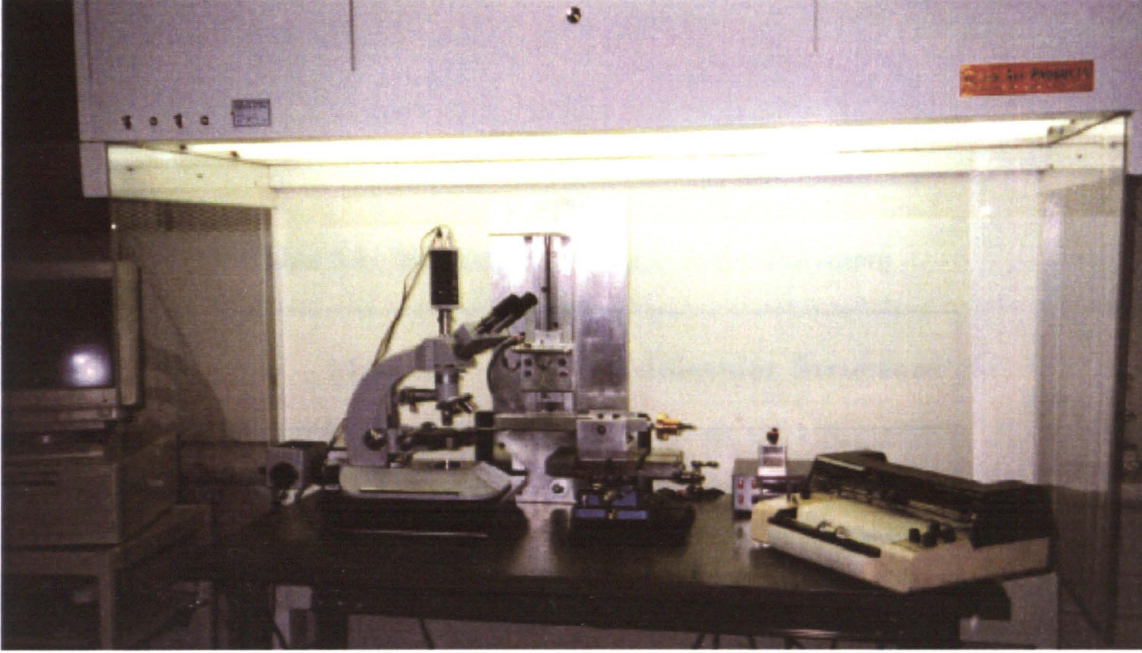
Figure 3-3: Photograph of experimental facility.

3.2   Materials

Several factors were considered in the selection of the polymers for testing. First, the polymers selected are those that are commonly used in the manufacturing industry. Hence these materials are easily machined and readily available. Second, information about the physical and chemical properties of these polymers can be readily obtained. Tables 3.1 and 3.2 list the molecular structures and the physical properties of the polymers used. The Poisson's ratio, ν, of these polymers is assumed to be 0.33. The Young's Moduli of some of the polymers were determined experimentally. The hardness, H, was measured using a Vickers hardness tester, and the tensile yield strength, σ_Y, was approximated by

$$\sigma_Y = \frac{H}{3}.$$

The hardness of UHMWPE could not be measured accurately because of the roughness of its surface. In cases where experimental measurements were not carried out, the physical properties were obtained from property handbooks [Alexander et al., 1996; Askadskii, 1996; Hunt, 1992].

The polymers were fabricated into pins of approximately 5 mm long and 6.35 mm in diameter and a radius of curvature of 3.175 mm. Initially, the polymer stock was turned down to a 6.35 mm radius rod. The spherical tip was manually machined using a radial cutter on a lathe. The spherical tips of the pins were polished with a plastic polish (Novus Plastic Polish 2). These pins were then ultrasonically cleaned

29

Table 3.1: Molecular Structure of the Polymers

Material	Molecular Structure
Ultra High Molecular Weight Polyethylene (UHMWPE)	[Polyethylene]
Polytetrafluoroethylene (TEFLON)	
Polychlorotrifluoroethylene (KEL-F)	
Polymethylmethacrylate (PMMA)	
Polyhexamethylene adipaide (NYLON 66)	
Polyetheretherketone (PEEK)	

Table 3.2: Physical properties of polymers.

Material	Young's Modulus E (GPa)	Tensile Yield Strength σ_Y (MPa)	Hardness H (MPa)	Surface Energy γ (J/m^2)
Ultra High Molecular Weight Polyethylene (UHMWPE)	1.62 ± 0.50	32.10	96.3	0.029
Polytetrafluoroethylene (Teflon)	0.53 ± 0.02	28.24	84.7 ± 6.3	0.017
Polychlorotrifluoroethylene (KEL-F)	1.65	37.41	112.2 ± 11.5	0.028
Polymethylmethacrylate (PMMA)	2.94 ± 0.08	68.00	204.0 ± 18.0	0.037
Polyhexamethylene adipaide (Nylon 66)	2.32 ± 0.21	75.34	226.0 ± 21.0	0.038
Polyetheretherketone (PEEK)	3.75 ± 0.13	60.72	182.2 ± 16.9	0.048

Table 3.3: Physical properties of silicon.

Silicon	
Melting Point (^{0} C)	1410
Young's Modulus, E (GPa)	156.7
Poisson's Ratio, ν	0.28
Hardness (MPa)	9800
Surface Energy, γ (J/m^2)	1.27

in water and dried at room temperature before being used for experiments.

The substrate used in all the experiment was a P-Type (boron doped) silicon wafer oriented in the [100] direction (Diameter = 100 mm). These wafers were scribed into squares (10 mm × 10 mm) and bonded onto microscopy slides using adhesive tape. This was done as it is easier to handle microscopy slides compared with silicon samples which break easily. Also, the samples could be conveniently stored in plastic microscope slide cases after testing. The silicon samples were cleaned using isopropyl alcohol before being used in a test. In Table 3.3 the physical properties of silicon are listed. These properties were obtained from Properties of Silicon [Ma, 1987; Hardy, 1986].

3.3 Normal Load

In the previous chapter, the normal force per bump was calculated to be 0.27 N if the force on the chuck is distributed uniformly. Using Hertzian analysis, it has been calculated that the loading per bump lies in the elastic regime. However, realistically, the force distribution on the chuck may not be uniform due to surface irregularities. There may be a concentration of forces on some bumps and these may be plastically loaded. In the experiments conducted, the loads applied were kept below the maximum required for plastic deformation to be initiated. The central idea was to reproduce the conditions on the vacuum chuck. Hence, globally, the polymer pins were subject to elastic deformation. However, locally, depending on the topography of the surfaces, there may be plastic deformation at the asperity tips.

The load that was applied on the loading arm in any one experiment was measured using a strain gage and a chart recorder. Tables 3.4 to 3.6 list the Hertzian elastic contact parameters for the polymers for a range of loads from 0.2 N to 5.0 N. The applied normal load is measured using a strain gage which consists of four resistors to make up a full Wheatstone bridge circuit. The output of the strain gage is displayed

on a strip chart recorder which was calibrated to measure the value of the normal load being applied on the loading arm.

Table 3.4: Hertzian contact radius, a (μm)

Material	Load (N)						
	0.2	0.5	1.0	2.0	3.0	4.0	5.0
Ultra High Molecular Weight Polyethylene (UHMWPE)	64.8	88.06	110.9	139.8	160.01	176.1	189.7
Polytetrafluoroethylene (TEFLON)	93.0	126.2	159.0	200.3	229.3	252.4	271.8
Polychlorotrifluoroethylene (KEL-F)	63.8	86.6	109.1	137.5	157.4	173.3	186.6
Polymethylmethacrylate (PMMA)	52.8	71.7	90.3	113.7	130.2	143.3	154.4
Polyhexamethylene adipaide (NYLON 66)	57.1	77.4	97.6	123.0	140.7	154.9	166.8
Polyetheretherketone (PEEK)	48.8	66.2	83.4	105.1	120.3	132.5	142.7

Table 3.5: Hertzian contact pressure, p_0 (MPa)

Material	Load (N)						
	0.2	0.5	1.0	2.0	3.0	4.0	5.0
Ultra High Molecular Weight Polyethylene (UHMWPE)	22.7	30.8	38.8	48.9	56.0	61.6	66.3
Polytetrafluoroethylene (TEFLON)	11.0	15.0	18.9	23.8	27.2	30.0	32.3
Polychlorotrifluoroethylene (KEL-F)	23.5	31.8	40.1	50.5	57.8	63.6	68.6
Polymethylmethacrylate (PMMA)	34.3	46.4	58.6	73.9	84.5	93.0	100.1
Polyhexamethylene adipaide (NYLON 66)	29.3	40.0	50.1	63.1	72.4	80.0	85.8
Polyetheretherketone (PEEK)	40.1	54.5	68.6	86.5	99.0	108.8	117.2

Table 3.6: Maximum Shear Stress, $\tau_{MAX} = 0.31 p_0$ (MPa)

Material	Load (N)						
	0.2	**0.5**	**1.0**	**2.0**	**3.0**	**4.0**	**5.0**
Ultra High Molecular Weight Polyethylene (UHMWPE)	7.0	9.5	12.1	15.2	17.4	19.1	20.6
Polytetrafluoroethylene (TEFLON)	3.4	4.7	5.9	7.4	8.4	9.3	10.0
Polychlorotrifluoroethylene (KEL-F)	7.3	9.9	12.4	15.7	18.0	19.7	21.3
Polymethylmethacrylate (PMMA)	10.6	14.4	18.2	22.9	26.2	28.8	31.0
Polyhexamethylene adipaide (NYLON 66)	9.1	12.4	15.5	19.6	22.4	24.8	26.6
Polyetheretherketone (PEEK)	12.4	16.9	21.3	26.8	30.7	33.7	36.3

3.4 Calibration

An important calibration that needs to be carried out is the one that confirms that the particles imaged are indeed fragments from the pin. In the early stages of the research, an experimental run was carried out using a pin fabricated from KEL-F. Before the experiment, the surface of the substrate was carefully examined to ensure that no abnormal deposits were present on the surface. The polymer pin was then brought into contact with the substrate. After the contact was broken, the silicon substrate was again viewed and it was observed that some transfer had occurred from the pin onto the surface. The silicon substrate was subsequently analyzed by Scanning Electron Microscopy (SEM) and Energy Dispersive X-Ray Spectroscopy (EDX). The EDX spectrum (Figure 3-4) clearly identified the transferred fragments to be composed of chlorine which is a component of KEL-F. Hence, it was clear that the transferred fragments viewed on the silicon surface were indeed coming from the polymer pin.

In the course of subsequent experimentation, a similar procedure was adopted. Just before the polymer pin made contact with the silicon surface, the surface was carefully examined to ensure that it was free of contaminants. The EDX analysis was not carried out for each polymer. The initial verification with KEL-F was sufficient proof that transferred fragments did indeed originate from the polymer.

3.5 Image Analysis

A digitized image of the material transfer was captured by a CCD camera. Digitization is the process by which an image is divided into a array of small elements or pixels. Each pixel of the image is individually sampled and quantified in terms of its intensity. The image analyzer uses these different values of pixel intensity to carry out the counting and sizing operations. The spatial resolution of the analysis is determined by the width and length of each pixel by calibrating the software.

The spatial resolution of the software has to be so set that all length and area measurements reported by the software are accurate. This was done by viewing a thin wire of known diameter through the optical microscope using the lenses of the same magnification as those used to view the silicon substrate. The image of this wire was loaded on the image analysis software and the diameter was measured in pixel units. Hence the number of pixels that corresponds to a specific length is known and the exact measurement that corresponds to a specific number of pixels can be easily determined henceforth. The spatial resolution of the software was set at 1.5 μm for the lower magnification lens (EPI 6.3) and 0.8μm for the higher magnification lens (EPI 12.5). The lens that were used to view and capture the image was noted and the appropriate spatial resolution applied during image analysis.

X-RAY: 0 - 20 keV   Window : ATW
Live: 30s Preset: 30s Remaining: 0s
Real: 58s   48% Dead

C O F   N
              a

                              C   K

< .0   2.563 keV   5.1 >
FS= 1K   ch 138=   54   cts
MEM1:9707162   /MEM2

(a)

X-RAY: 0 - 20 keV   Window : ATW
Live: 33s Preset: 30s Remaining: 0s
Real: 66s   50% Dead

        O   N   K
   C   a   C
        F   l

< .0   2.563 keV   5.1 >
FS= 1K   ch 138=   220   cts
MEM1:9707161   /MEM2
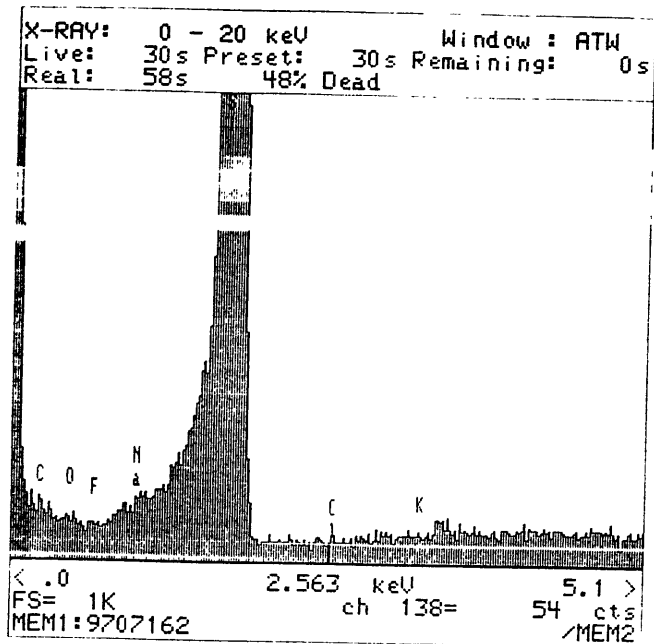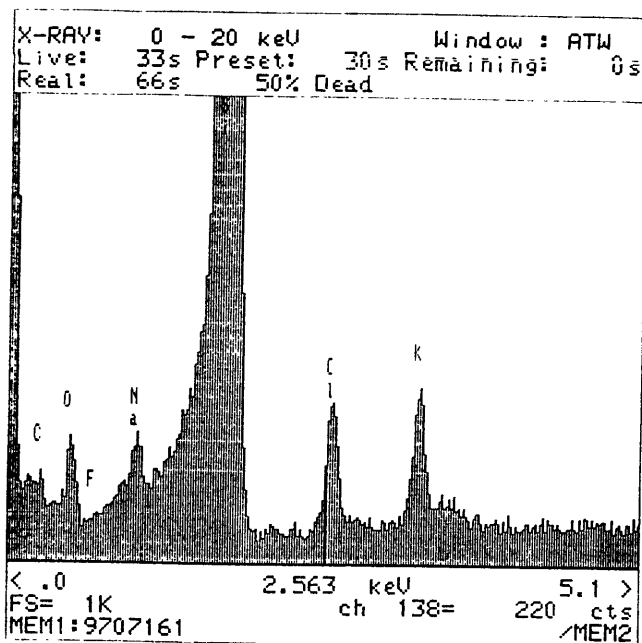
(b)

Figure 3-4: EDX Spectrum of KEL-F particles on silicon surface. Figure (a) is the EDX analysis of an area on the silicon where there were no particles. Figure (b) is the spectrum of an area where there were KEL-F particles. Traces of chlorine appear in spectrum (b) only, indicating that particles have chlorine in their molecular structure.

37

3.6 Measured Quantities

The software had the capability to furnish the number of particles, maximum and minimum area of the particles, and maximum and minimum diameter of the particles. Figure 3-5 is a photograph of the Image Analysis interface.

A quantity defined as the experimental radius was measured for each image. This was done by measuring the radius of a circle enveloping the particles. The number of particles in the image captured by the CCD camera is identified by counting the number of individual objects that are made up of pixels of above a certain intensity called the threshold value which is set by the user.

The area of each particle was measured by the area of the pixels that make up the particle. Hence, the smallest area reported is always the area of a single pixel which is set by the spatial resolution of a pixel. A particle that is smaller than a pixel area is reported to be of one pixel. Therefore, particles smaller than 2.25 μm^2 cannot be detected when the lower magnification lens is used. Similarly, particles smaller than 0.64 μm^2 cannot be detected if the higher magnification lens is used.

Also, it was observed that in many cases, the area of a small cluster of particles was reported to be that of one large particle. This had the effect of skewing the value of the mean particle size. The mean value reported was large because of this. The median is a more meaningful statistical quantity in this case as the value of the 50th percentile is not effected by these few large particles. Hence, the median value for the particle area is used to represent the size of the transferred fragments for a particular experiment.

The maximum and minimum diameter of an object is obtained by reporting the length of the longest and shortest line that passes through the centroid of each object. Thus, particles whose diameters are smaller than a pixel are assigned zero values and were discarded during data analysis.

Outlined below are the quantities calculated for each experiment. These quantities were used for analysis of the results.

- Experimental Radius

- Number of Particles

- Particle Density (Number of Particles / Hertzian Contact Area)

- Median Particle Size

- Total Particle Area

- Area Fraction (Total Particle Area / Hertzian Contact Area)
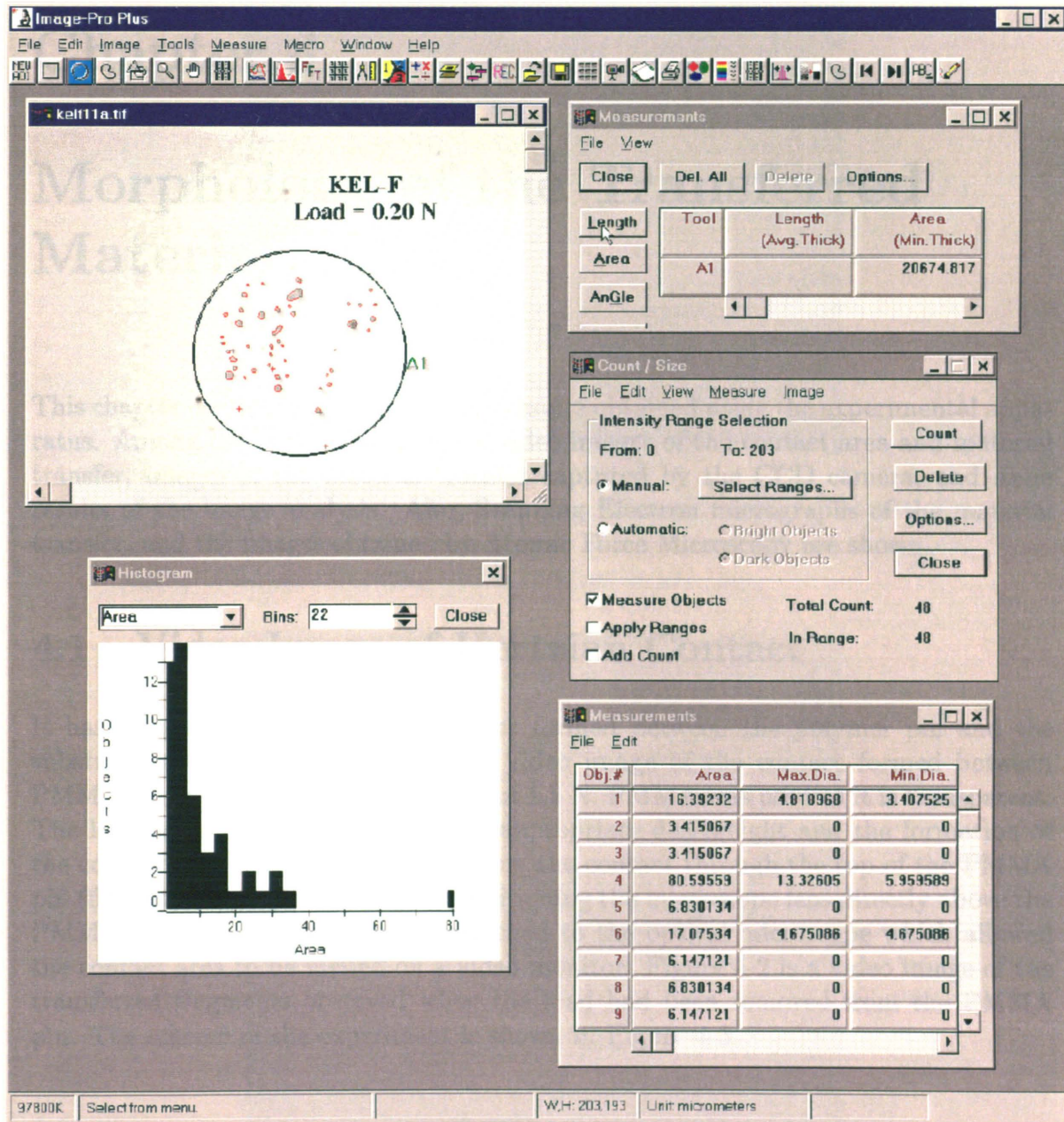
Figure 3-5: Image ProPlus 2 Analysis Window. Depicted are the various tool boxes for the counting and measuring operations.

Chapter 4

Morphology of the Transferred Material

This chapter contains some preliminary results obtained using the experimental apparatus. Among the items presented are video images of the contact area and material transfer, images of the material transfer captured by the CCD camera, and some results of the image analysis. Also, Scanning Electron micrographs of the material transfer, and the images obtained by Atomic Force Microscopy are shown.

4.1   Video Image of Hertzian Contact

It has been confirmed that the contact formed between the polymer pin and the substrate is circular. Figure 4-1 is a video image of the contact formed between PMMA and silicon with a normal load of 1.5 N. PMMA was used as it is transparent. The loading arm was loaded with the appropriate deadweight and the formation of the contact area was observed by viewing the contact through the top of the PMMA pin (flat surface). This was done by positioning the microscope lens directly above the PMMA pin. A CCD camera was attached to the optical microscope which allowed the contact area to be viewed on a video monitor. Figure 4-2 is a video image of the transferred fragments observed when the load had been removed from the PMMA pin. The scheme of the experiment is shown in Figure 4-3.
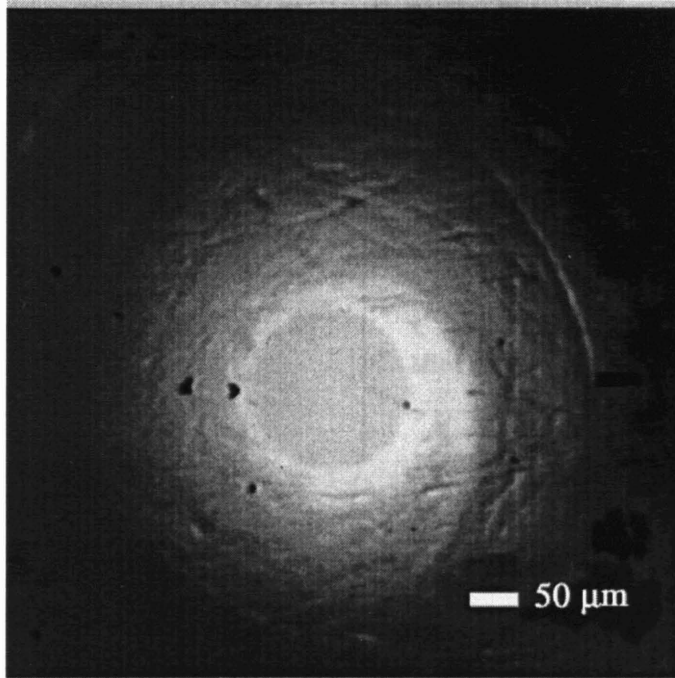
Figure 4-1: Video image of contact area. Normal load: 1.50 N. Pin material: PMMA, Radius of curvature of pin = 1 mm. Measured contact radius = 70 μm. Hertzian contact radius = 104 μm.
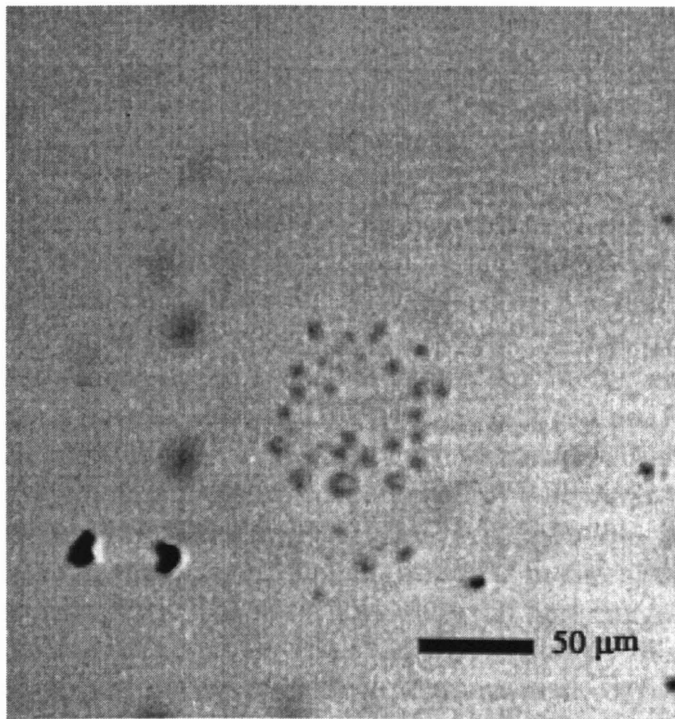
Figure 4-2: Video image of material transfer. Average particle diameter $\approx$ 8 μm.

View Contact Through PMMA Pin

Microscope Lens

PMMA Pin

Si
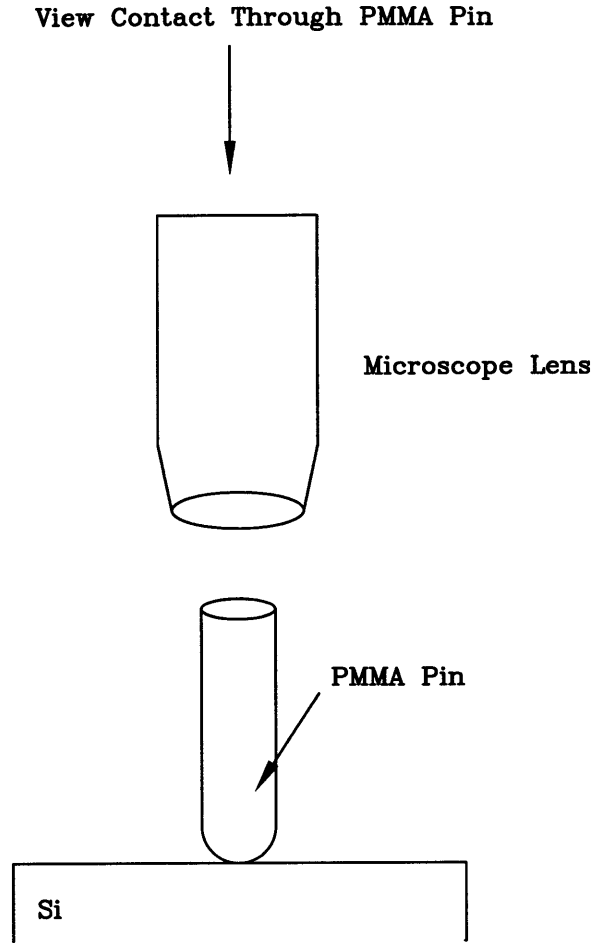
Figure 4-3: Schematic of experiment with PMMA pin.

The contact radius was measured at small increments of the normal load applied on the loading arm. This was done during loading and unloading. In Figure 4-4, the experimentally measured contact radius during loading and unloading are plotted together with the theoretical Hertzian contact radius. In this case, for the contact between PMMA and silicon under a normal load of 1.5 N, the experimentally measured contact radius is smaller than the Hertzian contact radius. However, the shape of the experimental curve is similar to that of the Hertzian contact. There are some differences in the contact area measured during loading compared with that measured during unloading. Theoretically, since the loads were kept low, so that the contact formed would be elastic, there should be no variations in the measured contact area during loading and unloading. The variations observed here suggest that the PMMA pin was subject to some deformation, changing its geometry. This probably occured at the higher loads. Hence, during unloading, the measured contact area was not the same as that during loading.

x 10^2
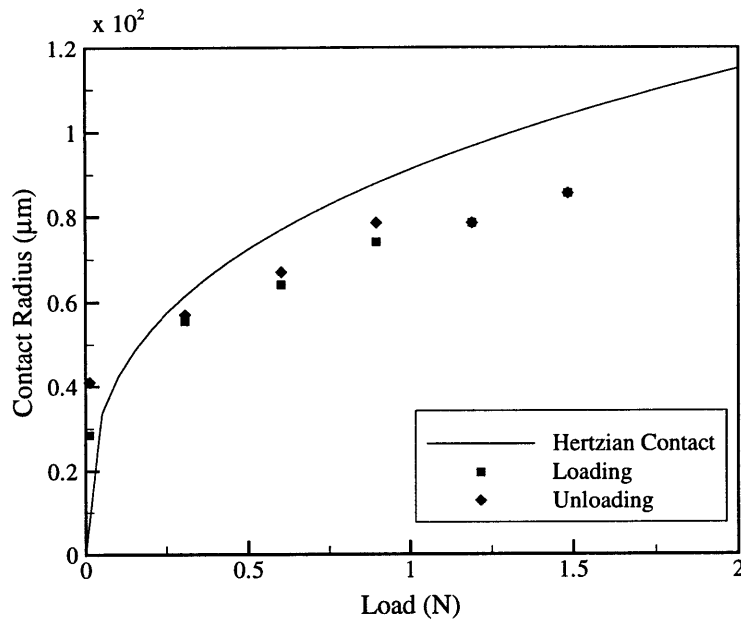
Figure 4-4: Experimental contact radius compared with Hertzian contact radius.

4.2 Images and Analysis of Transferred Fragments

Figures 4-5 to 4-10 are the representative images of the particles transferred from pins fabricated from UHMWPE, Teflon, KEL-F, PMMA, Nylon-66, and PEEK respectively. In all cases the applied normal load was 1.1 N. The distribution of the particle area is shown in the corresponding histograms. Table 4.1 lists the statistics of the particle area for each polymer used.
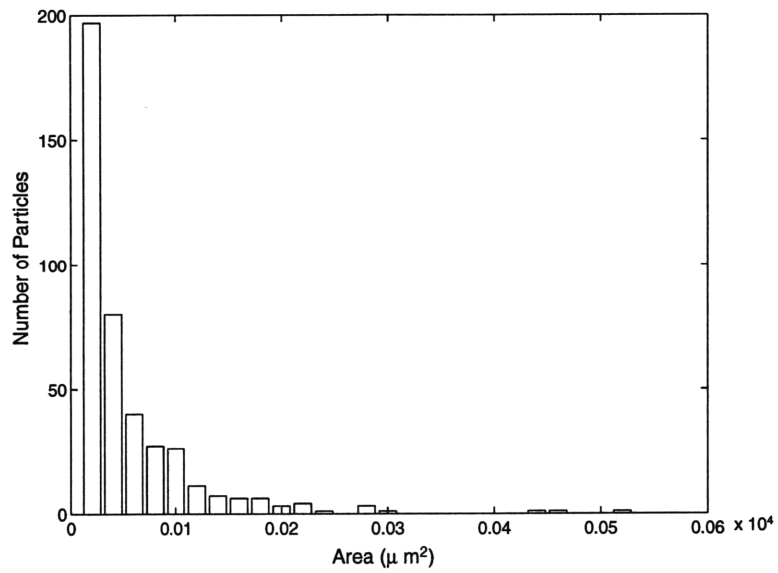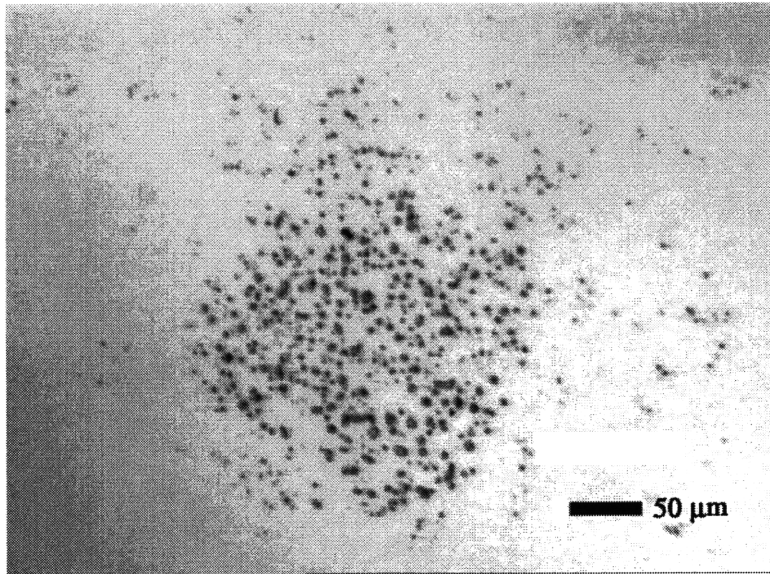
Figure 4-5: Material transfer from UHMWPE. Load = 1.1 N.
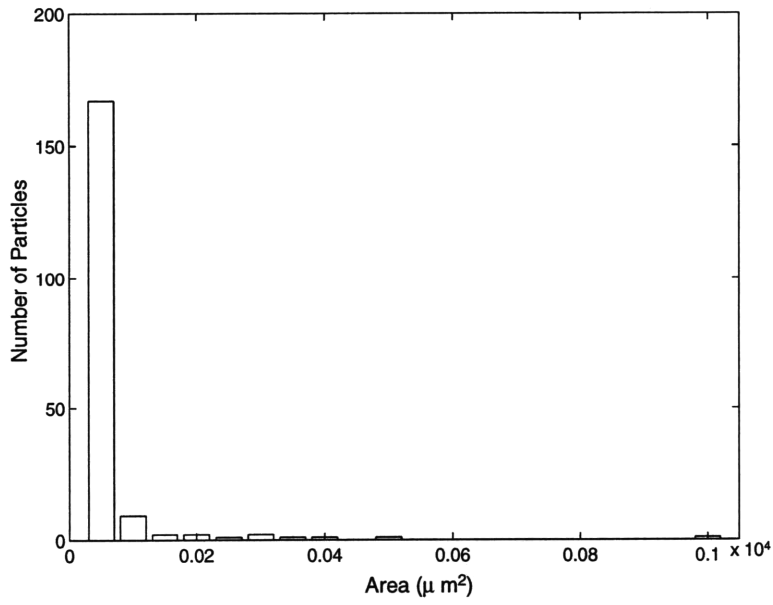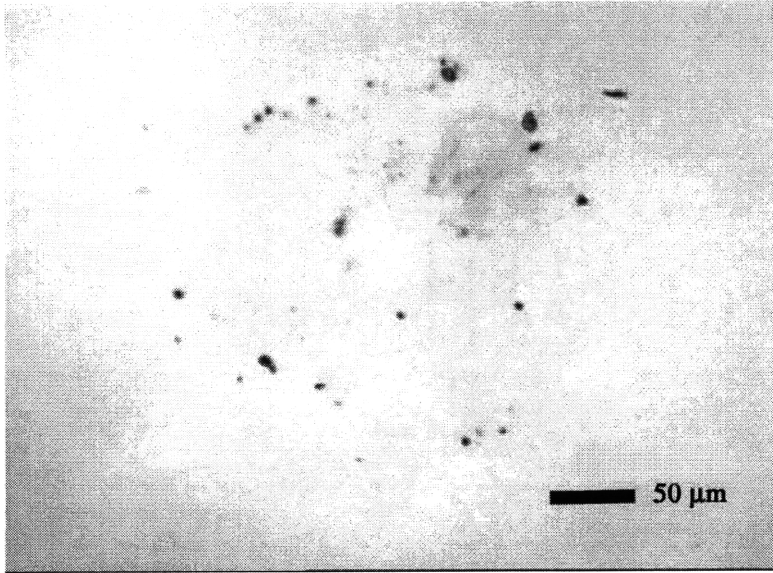
Figure 4-6: Material transfer from Teflon. Load = 1.1 N.
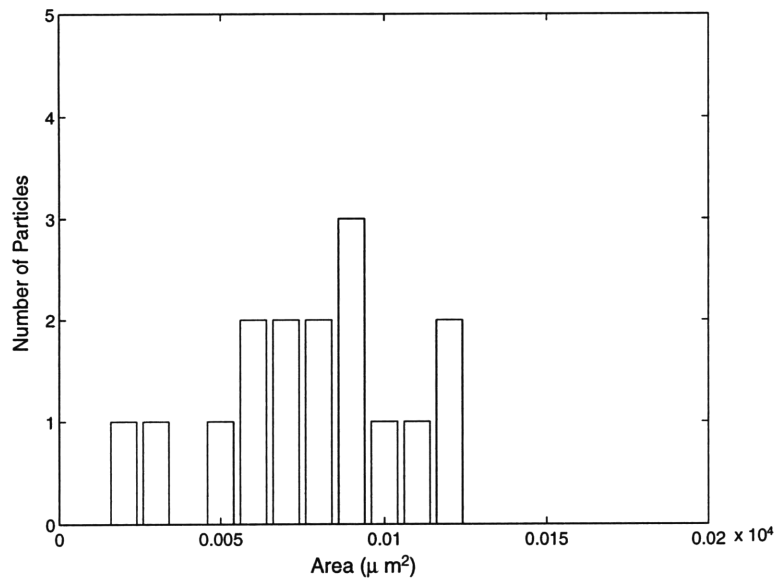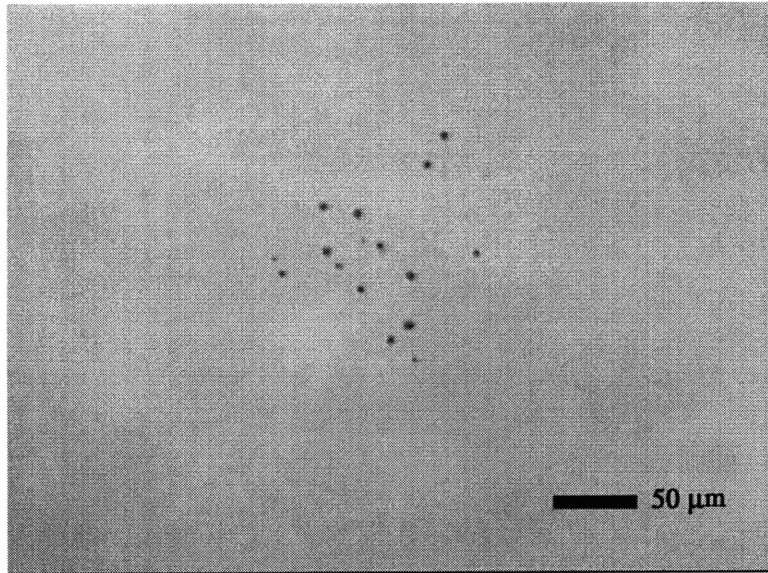
Figure 4-7: Material transfer from KEL-F. Load = 1.1 N.
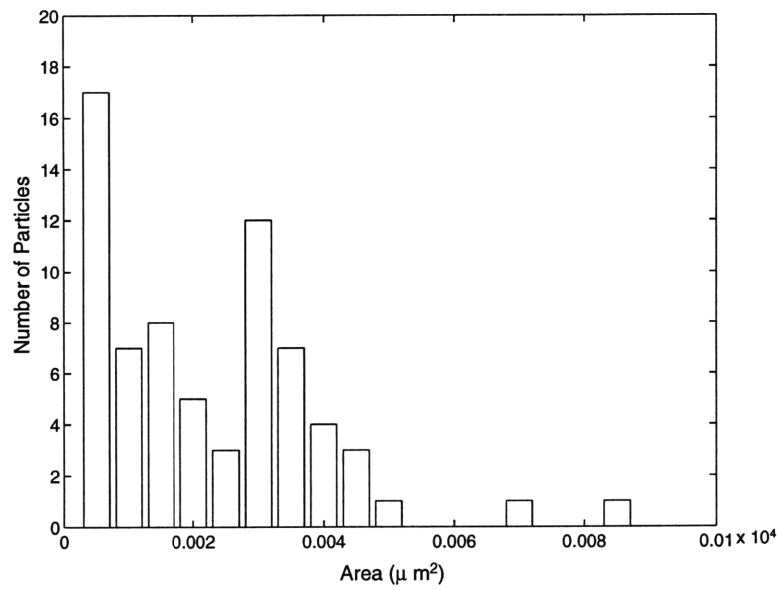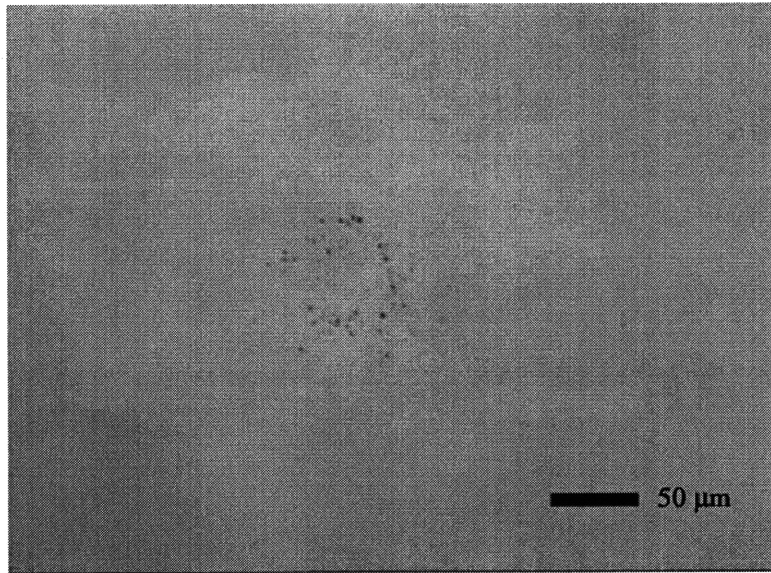
Figure 4-8: Material transfer from PMMA. Load = 1.1 N.
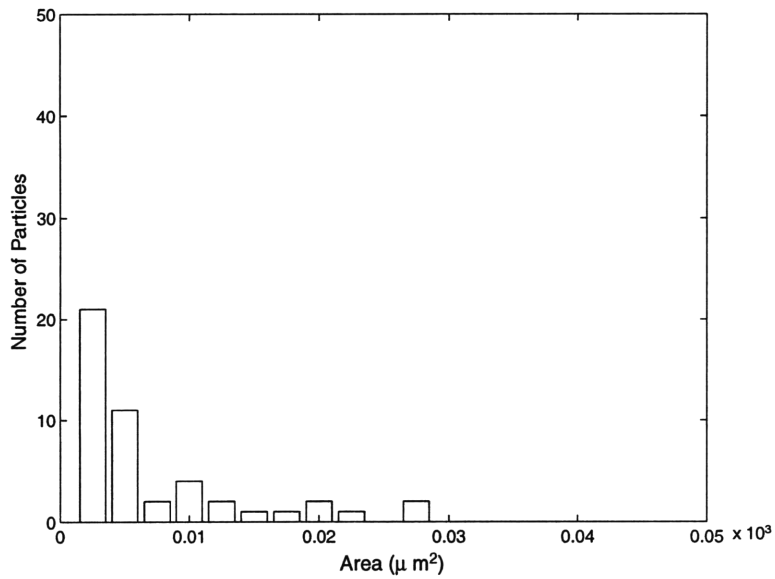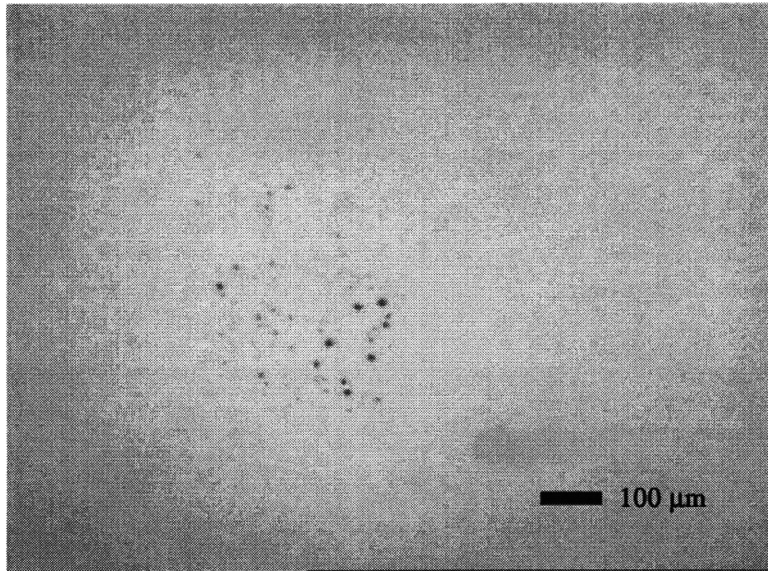
Figure 4-9: Material transfer from Nylon 66. Load = 1.1 N.
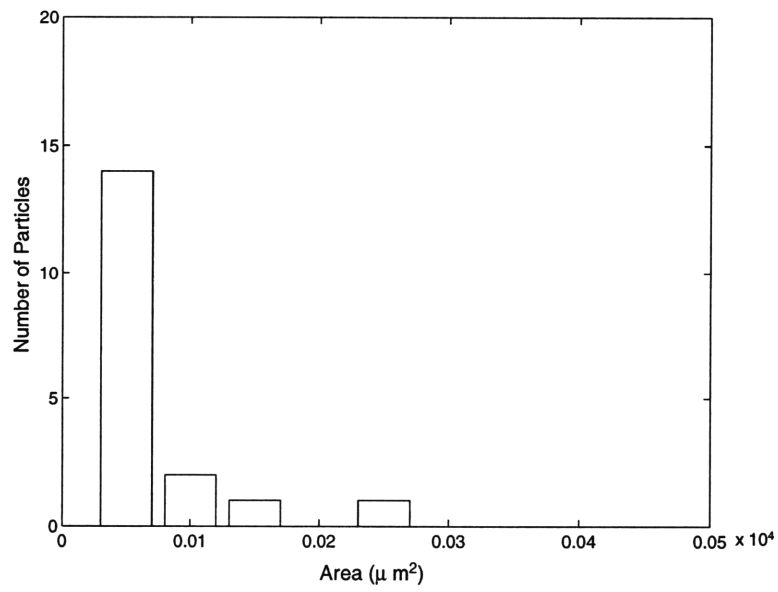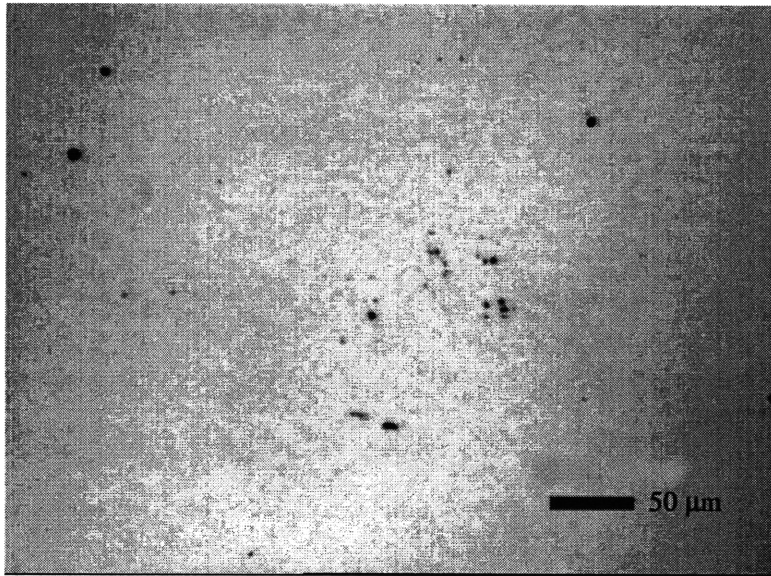
Figure 4-10: Material transfer from PEEK. Load = 1.1 N.

Table 4.1: Statistics of particle area. Normal load = 1.1 N.

Material	Number of Particles	Maximum Particle Area (μm^2)	Minimum Particle Area (μm^2)	Mean Particle Area (μm^2)	Median Particle Area (μm^2)	Standard Deviation (μm^2)
Ultra High Molecular Weight Polyethylene (UHMWPE)	415	524.80	2.25	51.80	30.10	63.24
Polytetrafluoroethylene (Teflon)	187	1003.30	2.25	33.83	6.07	99.48
Polychlorotrifluoroethylene (KEL-F)	16	127.70	2.25	77.61	81.25	30.06
Polymethylmethacrylate (PMMA)	69	83.60	2.25	22.38	18.50	16.49
Polyhexamethylene adipaide (Nylon 66)	47	27.00	0.64	6.82	3.86	7.22
Polyetheretherketone (PEEK)	18	232.00	2.25	47.93	19.87	62.00

In all cases, a large number of particles fall within a circular area. This circular area is defined as the experimental contact area. The figures suggest that the real contact area between the polymer pin and silicon occurs perhaps at the tips of the asperities of the asperities of the polymer pin. If so, at the point where asperity contact occurs, there is material transfer.

The histograms indicate that the distribution of the particle area is non-gaussian. It can be seen that for some of the polymers (UHWMPE, Teflon, Nylon 66 and, PEEK), the standard deviation of the particle area is larger than the mean particle area (Table 4.1). This occurs because of the clustering of particles as described in (*Chapter 3*). Due to the limitations of the image analysis software, particles that are very close each other are counted as one large particle. When this happens, the value of the mean particle area reported is large and the standard deviation is larger than the mean.

It can be seen that the histograms are skewed to the lower end (left side), indicating that there are a large number of small particles in each case. The minimum particle area is limited to the spatial resolution of the software. Hence the smallest particle area reported is always 2.25 μm^2 when the lower magnification lens is used and 0.64 μm^2 when the higher magnification lens is used. Due to this limitation, particles that are smaller than the spatial resolution are still reported to be either 2.25 μm^2 or 0.64 μm^2 depending on the magnification. This explains why the histograms are skewed to the left.

At a glance, it is evident that there is a variation in the material transfer with different polymers. First, there is variation in the experimental contact area and second, a variation in the number and size of particles. The physical properties of the polymers such as the Young's Modulus, tensile yield strength, or the surface energy may be responsible for this variation. The dependency of these quantities on material transfer is discussed in *Chapter 5*.

4.3   Scanning Electron and Atomic Force Microscopy

Figure 4-11 and 4-12 are SEM micrographs of Teflon particles on silicon. The bright spots on the surface are Teflon particles. Figure 4-13 and 4-14 are the images of a couple of KEL-F particles on silicon obtained by Atomic Force Microscopy. The normal load applied in this case was 1.1 N. In these micrographs, it is evident that the particles are shaped like "pancakes". The diameter of the particles is approximately 4.2 μm and the vertical height is 0.03 μm.

Figure 4-11: Scanning Electron Micrographs of Teflon particles on silicon. Normal load: 2 N. Magnification: 330.

Figure 4-12: Scanning Electron Micrographs of Teflon particles on silicon. Normal load: 2 N. Magnification: 1000.

NanoScope   Tapping AFM
Scan size   30.00 µM
Setpoint   2.813 V
Scan rate   0.5003 Hz
Number of samples   256

µM

20

10

X   10.000 µM/div
Z   10.000 µM/div
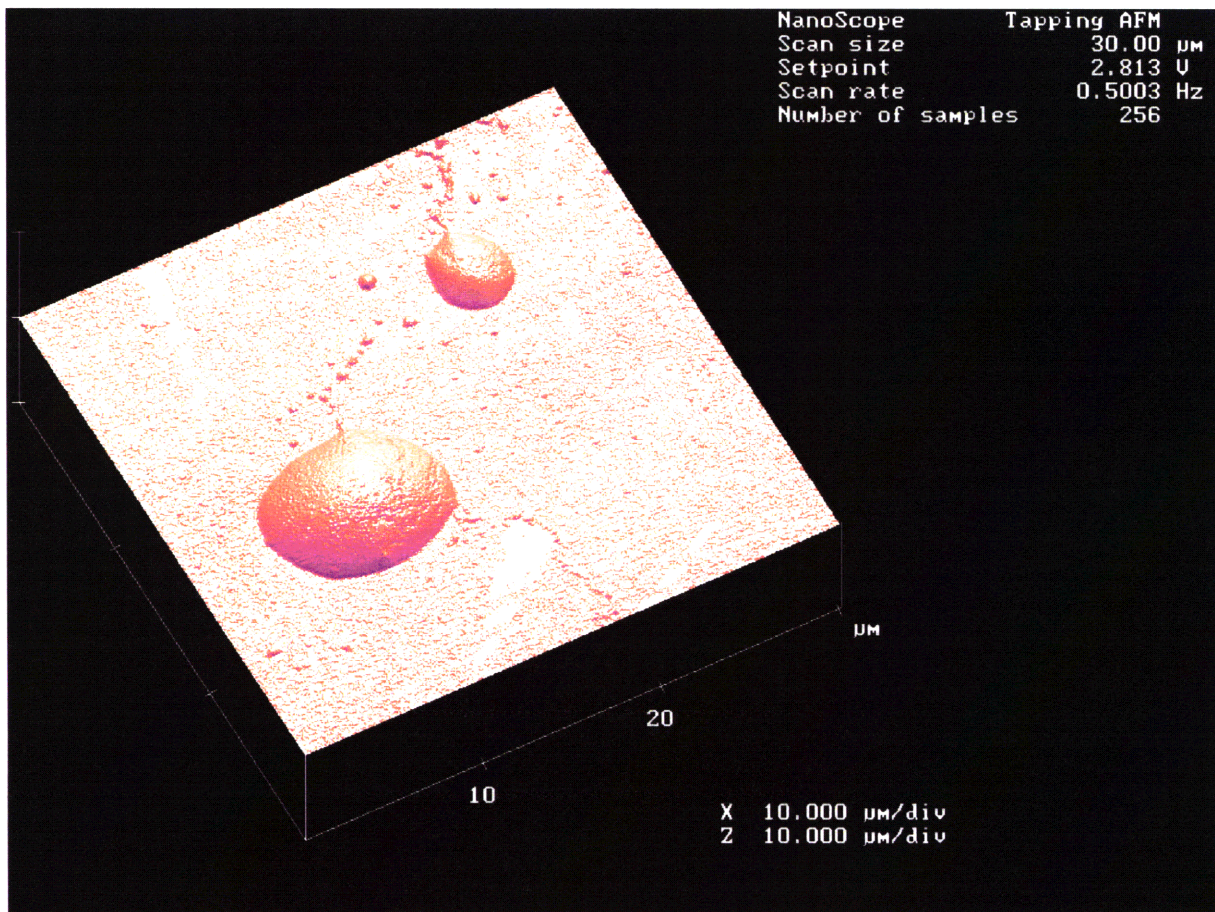
Figure 4-13: Atomic Force Micrograph of KEL-F particles on silicon.
Normal load: 1.1 N.
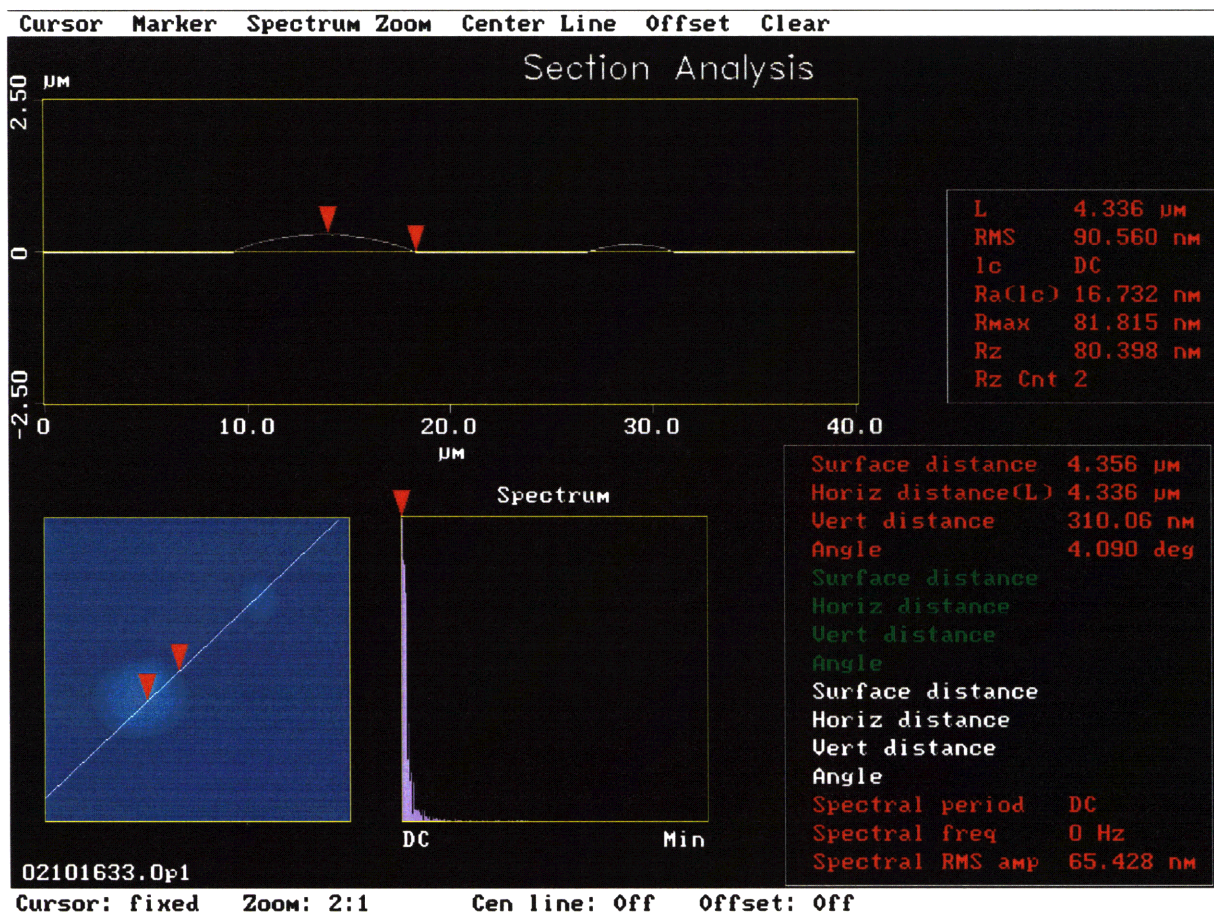
Figure 4-14: Analysis of KEL-F particles on silicon by AFM. Normal load: 1.1 N.

4.4 Summary

The preliminary results indicate that the contact area formed between the polymer pin and silicon is circular. However, particle transfer occurs at the points where the asperity tips touch the silicon surface. The distribution of the particle area is non-gaussian. The transferred fragments consist of a large number of small particles which are "pancake" like. It is evident that there is a variation in the number and size of particles deposited for different polymers. In the following chapter, the effects of varying the experimental parameters and material properties of interest are studied.

Chapter 5

Results and Discusssion

The variables of interest in backside contamination have been identified by the theoretical studies on elastic contacts and adhesion. In this chapter, the effects of varying some of the parameters of the problem are studied. First, the trends in the material transfer with variation in load are characterized. This is done by analyzing the material transfer from KEL-F, as an example. This is followed by a more complete investigation of the parameters of the problem using UHMWPE, Teflon, KEL-F, PMMA, Nylon 66, and PEEK.

5.1 Effect of Load on Material Transfer

In this part of the study, all other parameters except the normal load were kept fixed. The polymer used was KEL-F. Hertzian analysis predicts that the load at which the maximum shear stress, τ_{MAX} in KEL-F approaches the shear strength, τ_Y, of the polymer is 3.4 N. In these experiments, normal loads up to 5.0 N were used so as to identify any changes that may occur in the the material transfer from KEL-F when loads large enough to initiate plastic deformation are applied. Table 5.1 lists the experimental conditions of this study.

The effect of an increase of normal load N for constant E and R, is to increase the radius of Hertzian contact (Equation 2.1). The maximum Hertzian contact pressure, p_0, also increases (Equation 2.2).

$$a = \left(\frac{3NR}{4E^*}\right)^{\frac{1}{3}},$$

$$p_0 = \frac{3}{2} \cdot \frac{N}{\pi a^2}.$$

Hence, this study reveals how the contact area and pressure affects the material

Table 5.1: Experimental conditions

Test Conditions	
Pin Material	KEL-F
Diameter of Pin	6.35 mm
Radius of Curvature	3.175 mm
Substrate	Silicon
Normal Load	0.2 - 5.0 N
Temperature	25^0 C
Relative Humidity	18 - 26 %

transfer phenomenon.

Figure 5-1 is a plot of the experimental contact radius versus the Hertzian contact radius. It is evident that there is a difference in the experimentally measured radius compared with that predicted by Hertzian analysis. The experimentally measured contact radius is approximately 1.3 times greater than that predicted by Hertzian equations (Equation 2.1). As described by Greenwood and Tripp (1967), elastic contact between surfaces that are not smooth produces a contact radius that is greater than that predicted by Hertzian analysis. However, Hertzian analysis remains valid if the non-dimensional parameter α falls below 0.05. Figure 5-2 indicates the variation in the non-dimensional parameter α with load for KEL-F. Since α is less than 0.05, the effect of surface roughness is minimal and Hertzian analysis for frictionless, smooth solids can be used. Hence, although the experimentally measured contact radius deviates from Herzian, Hertzian analysis is assumed to be valid. This is true for loads at least below 3.4 N. At the larger loads (4.0 - 5.0 N) however, the contact may no longer be elastic due to subsurface plastic deformation in the pin.
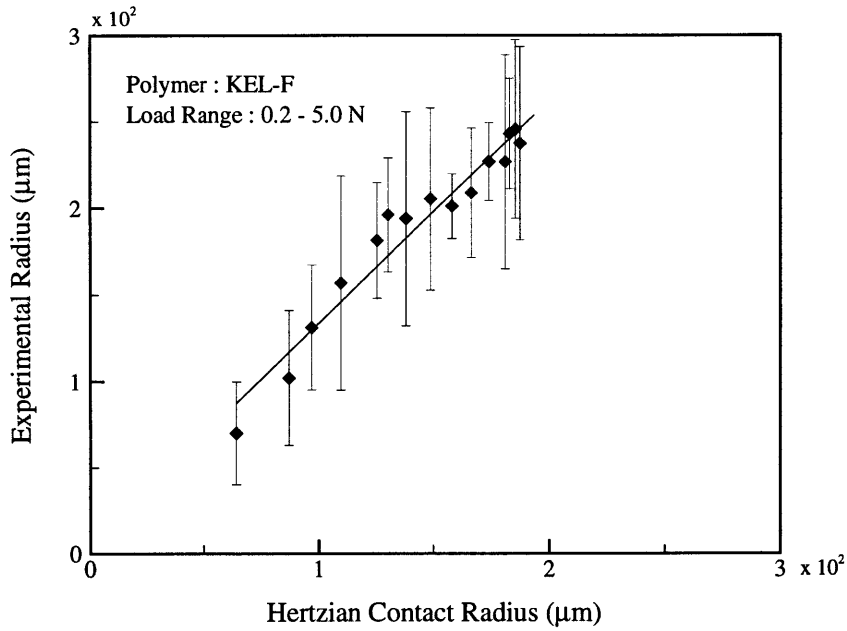
Figure 5-1: Experimental contact radius compared with the Hertzian contact radius.
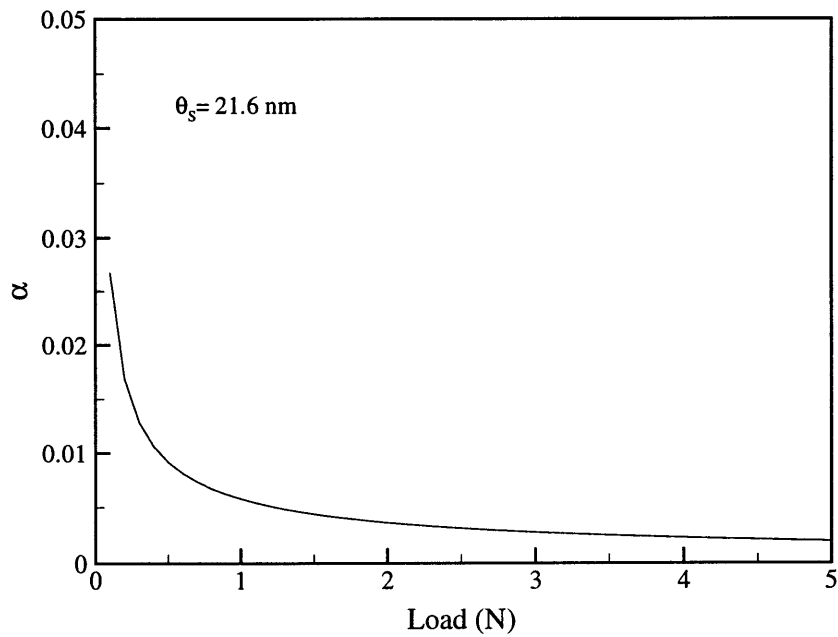
Figure 5-2: Variation of α with load for KEL-F. $\theta_S = 21.6$ nm. The standard deviation in asperity heights θ_S was measured on a profilometer.
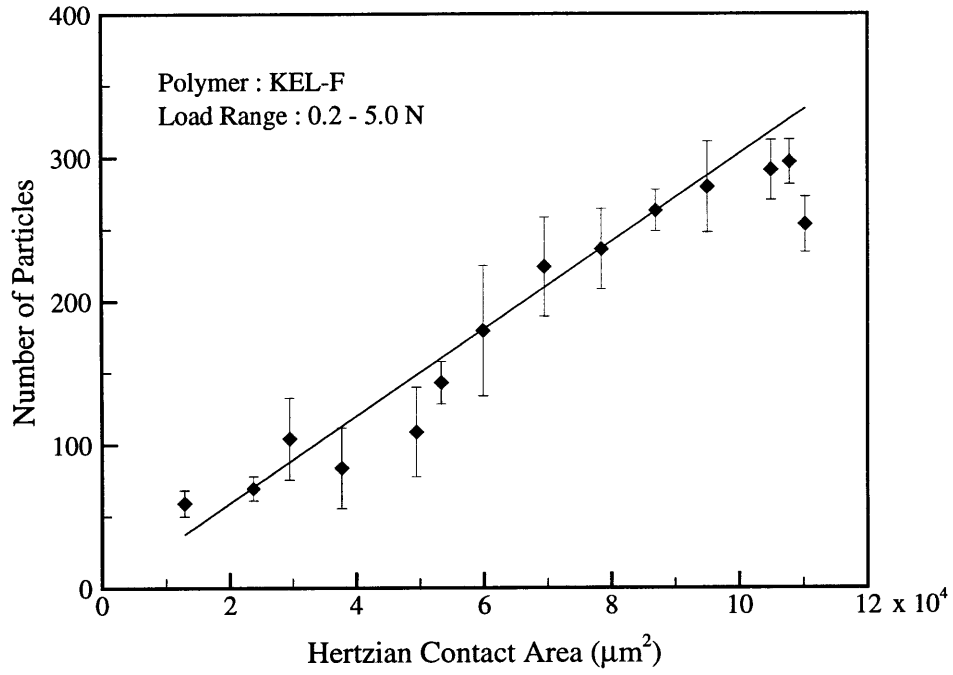
Figure 5-3: Number of particles versus Hertzian contact area.
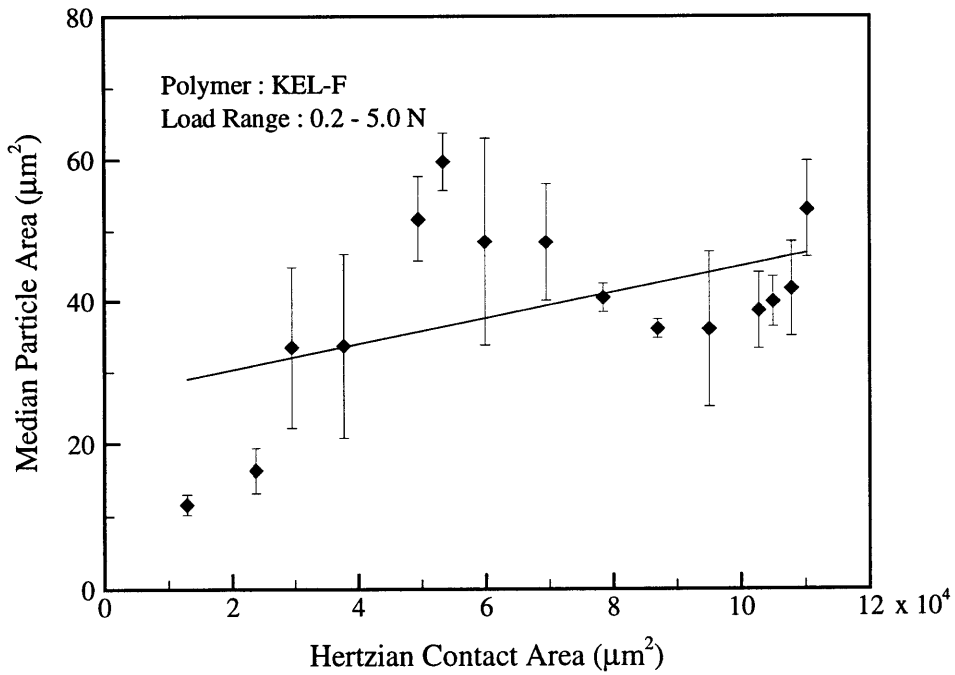
Figure 5-4: Median particle area versus Hertzian contact area.

59
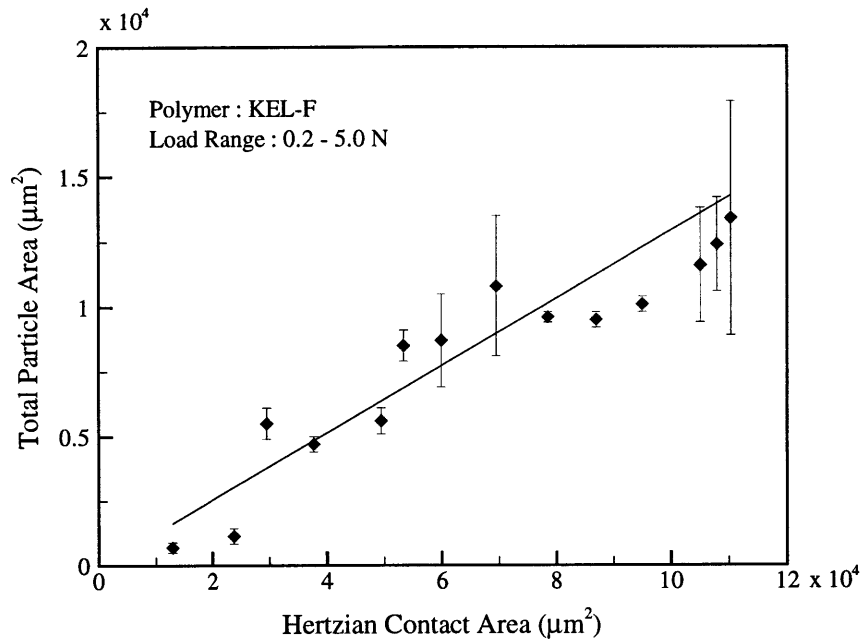
Figure 5-5: Total particle area versus Hertzian contact area.
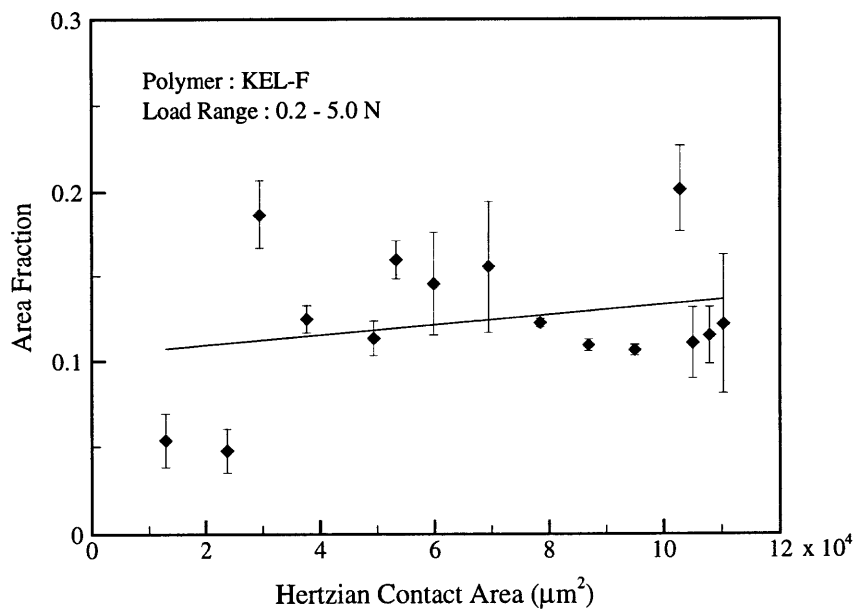
Figure 5-6: Area fraction (Total particle area/Hertzian contact area) versus Hertzian contact.

Figure 5-3 depicts the variation in the number of particles transferred with Hertzian contact area. There appears to be a linear relationship between the quantities. A straight line drawn through the points has a gradient equals to 30×10^{-4} μm^{-2}. An increase in contact area results in an increase in the number of asperities that touch the surface of the silicon as more of the pin is in contact with the substrate. The increase in contact pressure with load also may contribute to the increase in the number of particles deposited. At a specific contact pressure, a certain number of asperities are in contact with the silicon surface. The asperities that are in contact are those that are high enough to touch the silicon surface. An increase in the contact pressure allows the shorter asperities to touch the surface as well, resulting in more contact spots.

Figure 5-4 depicts the variation in median particle area with Hertzian contact area. The gradient of a straight line drawn through the points is about 1.8×10^{-4} μm^{-2}. There is a slight increase in the area of the particles deposited with increase in Hertzian contact area. This increase may be more dependent on the effect of load on the Hertzian contact pressure rather than the effect on Hertzian contact area. As explained previously, an increase in the contact pressure allows the shorter asperities to touch the surface and at the same time the area of contact between the asperities that were already touching the silicon surface increases. This increase in the individual asperity contact area results in an increase in the median area of the particles.

The total particle area is plotted against the Hertzian contact area in Figure 5-5. It is evident that the total particle area increases steadily with the Hertzian contact area. An interesting point to note is that for a particular Hertzian contact area, the spread in the data is minimal compared with the number of particles and median particle area plotted against the Hertzian contact area. This suggests that for a particular Hertzian contact area, the total area of the transferred fragments does not vary. Another important feature is observed in the plot of area fraction of the particles against the Hertzian contact area (Figure 5-6). The curve is almost a constant horizontal line. This suggests that for a given polymer, there is a linear relationship between the total particle area and the Hertzian contact area. Hence, for a given Hertzian contact area, the total area of the transferred fragments can be predicted. Knowing either the number of particles deposited or the median size of the particles, the particle transfer for a given Hertzian area is completely characterized. This is because, for these experiments, the median particle size is a reflection of the size of the particles deposited. The total particle area is the product of the total number of particles and the median particle area.

5.2 Effect of Surface Energy

In the JKR model, the Herzian analysis for elastic contact was modified to account for adhesion. Surface energy interactions were included in the analysis by considering the terms γ_p, γ_{Si}, and $\gamma_{p/Si}$, the surface energies of polymer, silicon, and the interfacial energy between polymer and silicon, respectively. Surface energy interactions produce a contact radius, a_1, given by

$$a_1 = \frac{3R}{4E^*}\left(N + 3\pi\gamma R + \sqrt{6\pi\gamma NR + (3\pi\gamma R)^2}\right),$$

where

$$\gamma = \gamma_p + \gamma_{Si} - \gamma_{p/Si}.$$

The JKR equation was rearranged so that the work of adhesion, γ, could be calculated. This is given by

$$\gamma = \frac{1}{3\pi R}\left(\frac{2E{a_1}^3}{3R} - N\right) + \frac{N^2}{8\pi E{a_1}^3}. \tag{5.1}$$

The JKR contact radius, a_1 was set as the experimentally measured contact radius and the value of γ was then used to calculate $\gamma_{p/Si}$ as γ_p and γ_{Si} are known. Knowing $\gamma_{p/Si}$ would allow the effect of the surface energy of the polymers, γ_p, on the material transfer phenomenon to be determined. The force of adhesion was also computed by

$$F = -\frac{3}{2} \cdot \pi\gamma R.$$

Table 5.2 lists an example of the values obtained for γ and $\gamma_{p/Si}$ using Equation 5.1 for KEL-F. The estimates for $\gamma_{p/Si}$ using Equation 5.1 produced negative results in certain cases, which is infeasible. A similar exercise was carried with the other polymers used. Negative values for $\gamma_{p/Si}$ were computed for the other polymers as well. It is evident from Table 5.2 that the largest value for the force of adhesion is 0.23 N (23 g) which occurs when the applied normal load, N, is 2.70 N. Attempts were made to measure this force using a strain gage which can measure forces as low as 1 g. However, no force could be detected by the strain gage. These results suggest that there is an error in the calculated value of γ using Equation 5.1, and that the experimentally measured contact radius does not approximate the JKR contact radius. Negative values for $\gamma_{p/Si}$ were obtained because the calculated values for γ were too large. Large values for γ were calculated as the the experimentally measured contact radius is larger than that predicted by JKR model. It appears that the effect of surface energy on material transfer cannot be readily determined. Moreover, the variation in the values for γ_p of the polymers selected is small. γ_{Si}, which is 1.27

62

J/m^2 at room temperature, overshadows the small variations in γ_p. Hence, the effect of surface energy on the material transfer phenomenon is weak.

Table 5.2: Calculated values for γ and $\gamma_{p/Si}$. Polymer: KEL-F. $\gamma_p = 0.028$ J/m^2 and $\gamma_{Si} = 1.27$ J/m^2

Load (N)	γ (J/m²)	$\gamma_{p/si}$ (J/m²)	Adhesive Force F (N)
0.3	1.706	-0.408	-0.026
0.5	0.722	0.576	-0.011
1.1	0.177	1.121	-0.003
2.2	10.34	-9.042	-0.150
2.7	15.18	-13.882	-0.230

5.3 Effect of Surface Roughness on Material Transfer

Surface roughness becomes important if the surfaces are too rough for Herzian analysis to be valid. This occurs if the nondimensional roughness parameter, α, is greater than 0.05. The parameter α depends on the topography of the surfaces, the load and the elastic constants of the materials. It is expressed by

$$\alpha = \theta_S \left(\frac{16RE^{*2}}{9N^2} \right)^{\frac{1}{3}} .$$

α was calculated for the polymers used. The standard deviation in the asperity heights, θ_S, was measured using a profilometer. Table 5.3 lists the calculated value for the non-dimensional parameter α for $N = 0.3$ N which is the lowest normal load applied.

The values of α fall below 0.05 in all cases except for UHMWPE. This is because the surface of the UHMWPE pin is rougher than that of the other pins. The standard deviation in asperity heights, θ_S, is almost a hundred times larger than that of the other polymers. Table 5.4 lists the Root-Mean-Square surface roughness for the poly-

Table 5.3: Values for the non-dimensional parameter α for the lowest load of 0.3 N. $\alpha > 0.05$ for UHMWPE.

Material	Standard Deviation θ_S (Å)	α
Ultra High Molecular Weight Polyethylene (UHMWPE)	1853.5	0.1
Polytetrafluoroethylene (TEFLON)	84.5	0.002
Polychlorotrifluoroethylene (KEL-F)	216.3	0.01
Polymethylmethacrylate (PMMA)	455.0	0.04
Polyhexamethylene adipaide (Nylon 66)	84.5	0.006
Polyetheretherketone (PEEK)	102.2	0.01

mer pins. The RMS surface roughness value of UHMWPE is about a hundred times larger than the RMS surface roughness values for the other polymers. These results suggest that the Hertzian analysis may not be appropriate for the UHMWPE pin.

Table 5.4: RMS surface roughness values for the polymers.

Material	Root-Mean-Square Surface Roughness R_a (Å)
Ultra High Molecular Weight Polyethylene (UHMWPE)	1459.4
Polytetrafluoroethylene (Teflon)	308.4
Polychlorotrifluoroethylene (KEL-F)	437.5
Polymethylmethacrylate (PMMA)	691.8
Polyhexamethylene adipaide (Nylon 66)	478.0
Polyetheretherketone (PEEK)	560.1

It is prescribed in theory that surface roughness increases the contact radius compared with that calculated by Hertzian analysis. Figure 5-7 is a plot of the variation of the experimentally measured contact radius with that predicted by Hertzian for all the polymers in the load range 0.3 - 2.7 N. It is clear that the results using UHMWPE fall outside the range of results of the other polymers. The most probable reason for the high surface roughness value may be that the surface was not polished as well as the other polymer pins after the machining operation.

The effect of surface roughness was further investigated by studying the material transfer from six different PMMA pins of different surface roughnesses. The spherical tips of the PMMA pins were roughened to varying degress using sandpaper. For all the pins, the value for the non-dimensional parameter α is below 0.05. Hence, the effect of rough surfaces when contact is still elastic can be ascertained. The normal load applied was fixed at 1.1 N. Table 5.5 lists the experimental results obtained for each pin.

Table 5.5 indicates that no specific trend can be identified with surface roughness when $\alpha < 0.05$. However, by comparing the last row of the table with the rest, there
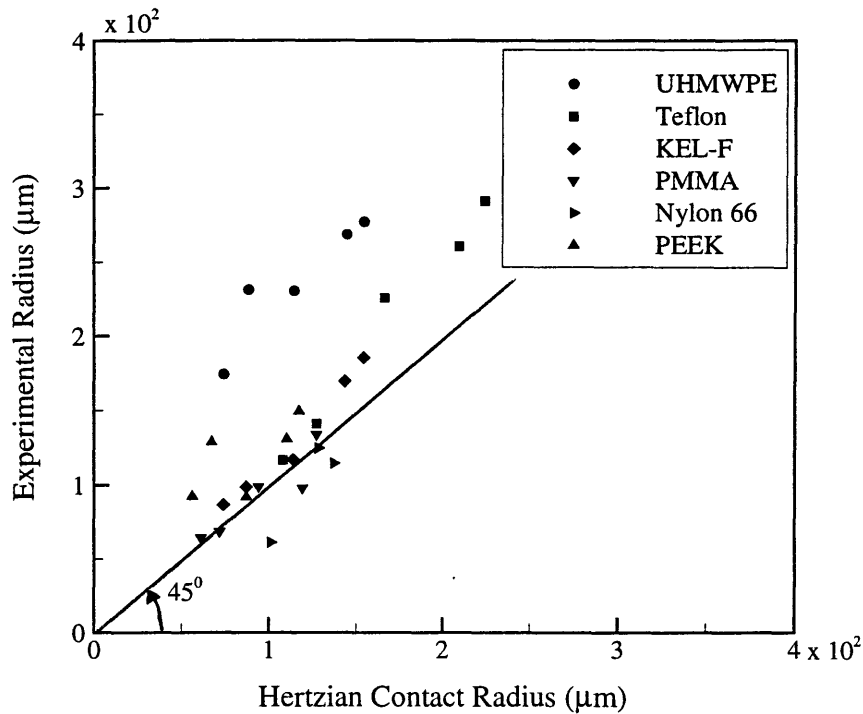
Figure 5-7: Variation of the experimentally measured contact radius with Hertzian radius.

is an indication that for rougher surfaces, the area frction increases because of an increase in the size of the particles deposited. A rougher surface has larger asperities and this increases the asperity contact area when the surfaces touch. Hence, the size of the particles increase, resulting in an increase in total particle area.

Table 5.5: Experimental results with PMMA pins of different surface roughnesses. Normal load = 1.1 N. Hertzian contact radius = 2.83×10^4 μm^2.

Root-Mean-Square Surface Roughness R_a Å	α	Particle Density ($1x10^4$ cm$^-$2)	Area Fraction	Median Particle Size (μm^2)
283.0	0.011	26.1	0.03	10.02
437.5	0.015	19.4	0.06	31.64
526.9	0.018	38.2	0.03	6.34
527.9	0.017	32.9	0.03	5.09
540.0	0.018	10.6	0.02	18.54
599.2	0.020	15.9	0.09	54.44

5.4 The Effect of Friction

The friction coefficient for all the polymers investigated was measured using the pin-on-flat friction tester (Appendix A). These are listed in Table 5.6.

Table 5.6: Coefficient of friction between polymer and silicon. Normal load = 1.0 N.

Material	Coefficient of Friction μ
Ultra High Molecular Weight Polyethylene (UHMWPE)	0.16
Polytetrafluoroethylene (Teflon)	0.08
Polychlorotrifluoroethylene (KEL-F)	0.16
Polymethylmethacrylate (PMMA)	0.43
Polyhexamethylene adipaide (Nylon 66)	0.23
Polyetheretherketone (PEEK)	0.21

In the regions where slip occurs, the tangential traction is given by

$$q = |\mu p|.$$

where p is the normal pressure distribution. Tangential traction opposses slip. When the friction coefficients are small, the slip region is larger. When slip occurs, wear particles may be generated resulting in material transfer.

Figure 5-8 is a plot of area fraction against the friction coefficient of the polymers. The load range used was 0.3 - 2.7 N. The data points are scattered and no definite trend can be identified. Theoretically, at larger friction coefficients, slip is inhibited and this may decrease the total particle area and hence the area fraction. The trends

68

exhibited are not distinct because the friction coefficients for the polymers are very close to each other. Hence, the slight differences in the amount of slip may not be large enough to affect the material transfer. However, it is possible that more definite trends may be identified at higher temperatures as the friction and wear of polymers increase with temperature (Appendix A).
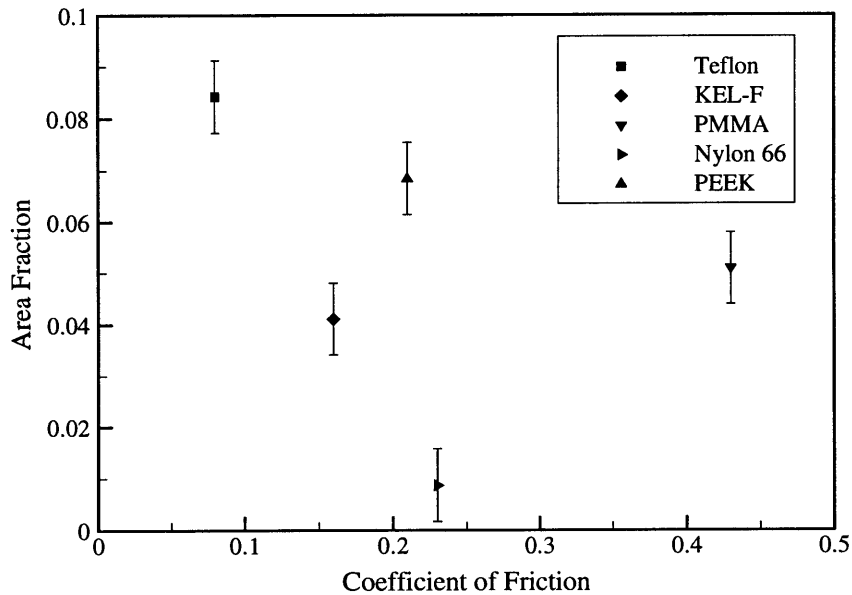
Figure 5-8: Area fraction versus the friction coefficient of the polymers. The load range applied was 0.3 - 2.7 N.

5.5 Effects of Young's Modulus, Yield Strength and Hardness

For a constant value of N, the effect of an increase in E is to decrease the Hertzian contact radius (Equation 2.1). At the same time, the maximum Hertzian contact pressure increases with an increases in E. The Hertzian equations for contact radius, a, and maximum pressure, p_0, are:

$$a = \left(\frac{3NR}{4E^*}\right)^{\frac{1}{3}},$$

and

$$p_0 = \frac{3}{2} \cdot \frac{N}{\pi a^2}.$$

69

Tables 5.7 to 5.11 list the experimental data for all the polymers in the load range of 0.3 - 2.7 N. For Nylon 66, the results only for loads greater than 1.10 is provide. This was because no material transfer could be observed for the lower loads. Also, experimental data for UHMWPE were not used as it has been assumed that UHMWPE was subject to plastic deformation at the asperities.

Table 5.7: Number of particles.

Material	Load (N)				
	0.3	0.5	1.1	2.2	3.0
Ultra High Molecular Weight Polyethylene (UHMWPE)	199	278	415	310	361
Polytetrafluoroethylene (Teflon)	53	138	187	235	227
Polychlorotrifluoroethylene (KEL-F)	11	27	16	62	75
Polymethylmethacrylate (PMMA)	28	42	69	42	99
Polyhexamethylene adipaide (Nylon 66)	0	0	47	56	146
Polyetheretherketone (PEEK)	34	34	18	45	82

Table 5.8: Particle density ($1x10^4$ cm^{-2}).

Material	Load (N)				
	0.3	0.5	1.1	2.2	3.0
Ultra High Molecular Weight Polyethylene (UHMWPE)	115.7	114.3	101.6	47.6	48.4
Polytetrafluoroethylene (Teflon)	14.5	27.3	21.6	17.1	14.4
Polychlorotrifluoroethylene (KEL-F)	6.4	8.8	3.9	9.7	10.1
Polymethylmethacrylate (PMMA)	24.0	25.8	24.9	9.4	19.5
Polyhexamethylene adipaide (Nylon 66)	0	0	14.7	10.9	24.7
Polyetheretherketone (PEEK)	34.5	24.1	7.6	11.8	19.1

Table 5.9: Total particle area ($1x10^4 \mu m^2$).

Material	Load (N)				
	0.3	0.5	1.1	2.2	3.0
Ultra High Molecular Weight Polyethylene (UHMWPE)	0.84	1.93	2.15	1.87	3.62
Polytetrafluoroethylene (Teflon)	0.14	0.31	0.63	2.95	0.54
Polychlorotrifluoroethylene (KEL-F)	0.02	0.10	0.12	0.28	0.58
Polymethylmethacrylate (PMMA)	0.07	0.12	0.15	0.09	0.26
Polyhexamethylene adipaide (Nylon 66)	0	0	0.01	0.05	0.08
Polyetheretherketone (PEEK)	0.13	0.08	0.09	0.20	0.29

Table 5.10: Area fraction.

Material	Load (N)				
	0.3	**0.5**	**1.1**	**2.2**	**3.0**
Ultra High Molecular Weight Polyethylene (UHMWPE)	0.48	0.79	0.52	0.28	0.48
Polytetrafluoroethylene (Teflon)	0.03	0.06	0.07	0.21	0.03
Polychlorotrifluoroethylene (KEL-F)	0.01	0.03	0.03	0.04	0.07
Polymethylmethacrylate (PMMA)	0.05	0.07	0.05	0.02	0.05
Polyhexamethylene adipaide (Nylon 66)	0	0	0.003	0.01	0.01
Polyetheretherketone (PEEK)	0.13	0.08	0.09	0.20	0.29

Table 5.11: Median particle size (μm^2).

Material	Load (N)				
	0.3	0.5	1.1	2.2	3.0
Ultra High Molecular Weight Polyethylene (UHMWPE)	32.5	29.0	30.1	39.4	58.0
Polytetrafluoroethylene (Teflon)	18.5	12.8	7.0	62.7	7.0
Polychlorotrifluoroethylene (KEL-F)	13.9	30.1	81.1	41.8	67.3
Polymethylmethacrylate (PMMA)	22.1	18.5	18.5	21.0	21.0
Polyhexamethylene adipaide (Nylon 66)	0	0	3.86	1.29	2.25
Polyetheretherketone (PEEK)	17.1	10.4	3.5	5.4	8.6

In order to ascertain the effect of Young's moduli of the polymers on the material transfer phenomenon, the number of particles, particle density, total particle area, area fraction and, median particle size were plotted against $(\frac{N}{ER^2})^{\frac{1}{3}}$. This quantity can be described as the strain at the surface associated with the average contact pressure. The strain, $\bar{\epsilon}$, can be written as,

$$\bar{\epsilon} = \frac{\bar{\sigma}}{E}.$$

(5.2)

$\bar{\sigma}$ can be written as being equal to $\frac{N}{\pi a^2}$. a is the Hertzian contact radius defined by Equation 2.1. Using these relationships for $\bar{\sigma}$, and a, Equation 5.2 becomes,

$$\bar{\epsilon} = \frac{16}{9\pi} \cdot \frac{N^{\frac{1}{3}}}{E^{\frac{1}{3}}R^{\frac{2}{3}}}.$$

(5.3)

Reducing Equation 5.3 further gives,

$$\bar{\epsilon} = \frac{16}{9\pi} \cdot \left(\frac{N}{ER^2}\right)^{\frac{1}{3}}.$$

Hence, $(\frac{N}{ER^2})^{\frac{1}{3}}$ is the non-dimensional parameter plotted on the x axis. This non-dimensional term, takes into account the effect of load on material transfer. Thus the effect of Young's modulus on material transfer can be studied for various combinations of loads and moduli.

Figures 5-9 and 5-10 indicate the variation of the number of particles deposited and the particle density with $(\frac{N}{ER^2})^{\frac{1}{3}}$. The normal load range is 0.3 - 2.7 N. In the previous study on KEL-F, it was evident that there existed a linear relationship between the number of particles and the Hertzian contact area. Therefore,

$$Number\ of\ particles \propto \left(\frac{3NR}{4E^*}\right)^{\frac{2}{3}}.$$

Factoring out $(\frac{N}{ER^2})^{\frac{1}{3}}$ from the relationship above gives,

$$Number\ of\ particles \propto \left(\frac{3}{4}\right)^{\frac{2}{3}} R^2 \left(\frac{N}{ER^2}\right)^{\frac{2}{3}}.$$

A quadratic curve was fitted to the data points in Figure 5-9. It is evident that this is an appropriate fit. This confirms that the number of particles is proportional to the Hertzian contact area. In Figure 5-10, based on the assumption that the number of particles is proportional to the Hertzian contact area, the data points should fall on a constant horizontal line. However, a least squares line fit to the data points indicates that the curve has a negative gradient.

Also, in previous studies with KEL-F, the total particle area increased linearly with the Hertzian contact area. Carrying out a similar exercise to that done with the number of particles, it is evident that the total particle area would be proportinal to $(\frac{N}{ER^2})^{\frac{2}{3}}$. Again, a quadratic curve fit appears to be the appropriate choice as seen in Figure 5-11. The plot of area fraction against $(\frac{N}{ER^2})^{\frac{1}{3}}$, should theoretically be a constant horizontal line. However, the least square line fit has a positive gradient equal to 0.7 (Figure 5-12).

No significant trend can be identified in Figure 5-13 which is is a plot of the median particle area against $(\frac{N}{ER^2})^{\frac{1}{3}}$. The data points are scattered and the effect of E on the size of the particles appear to be marginal.

The increase in the number of particles and total particle area with increase in Hertzian contact area is because more asperities on the surface of the polymers make contact with the surface, resulting in greater transfer. The effect of Young's modulus on the material transfer is significant because the Young's modulus sets the Hertzian contact area when N and R are fixed. Hence, at high values of Young's modulus, the number of particles and total particle area decreases.
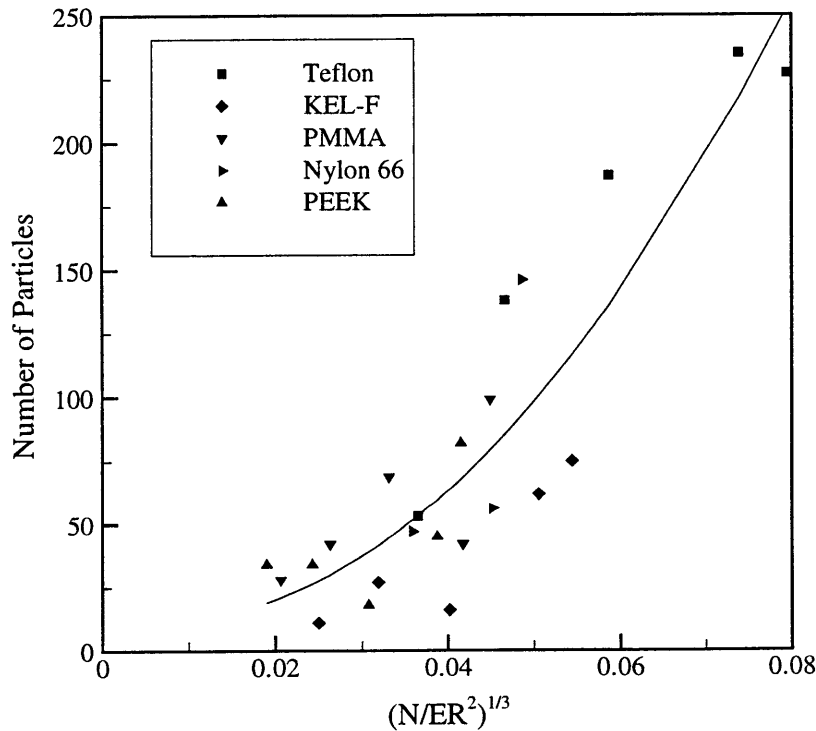
Figure 5-9: Number of particles versus $(\frac{N}{ER^2})^{\frac{1}{3}}$.
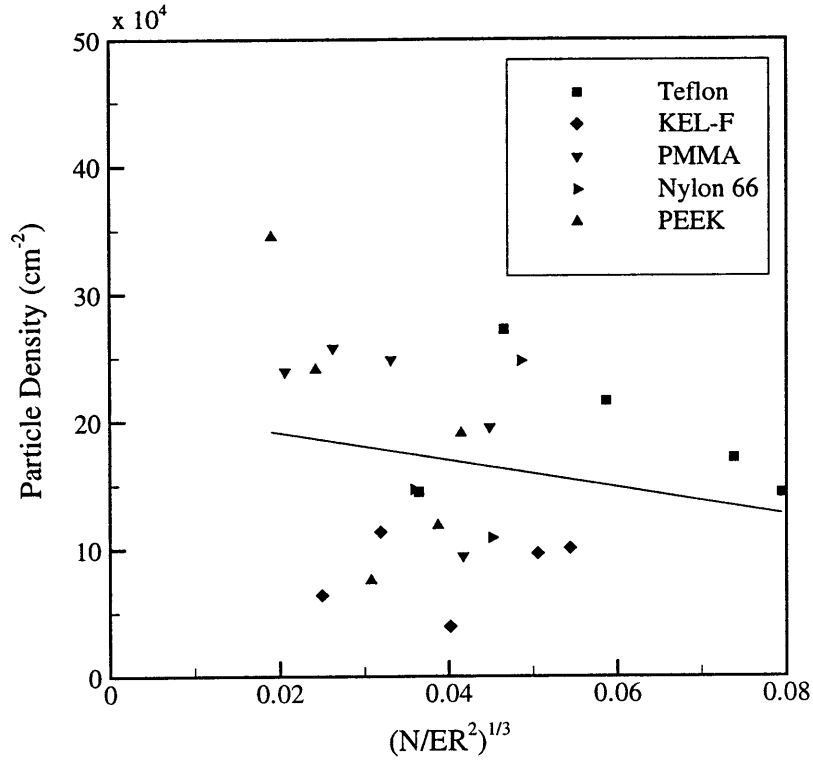
Figure 5-10: Particle density versus $\left(\frac{N}{ER^2}\right)^{\frac{1}{3}}$.
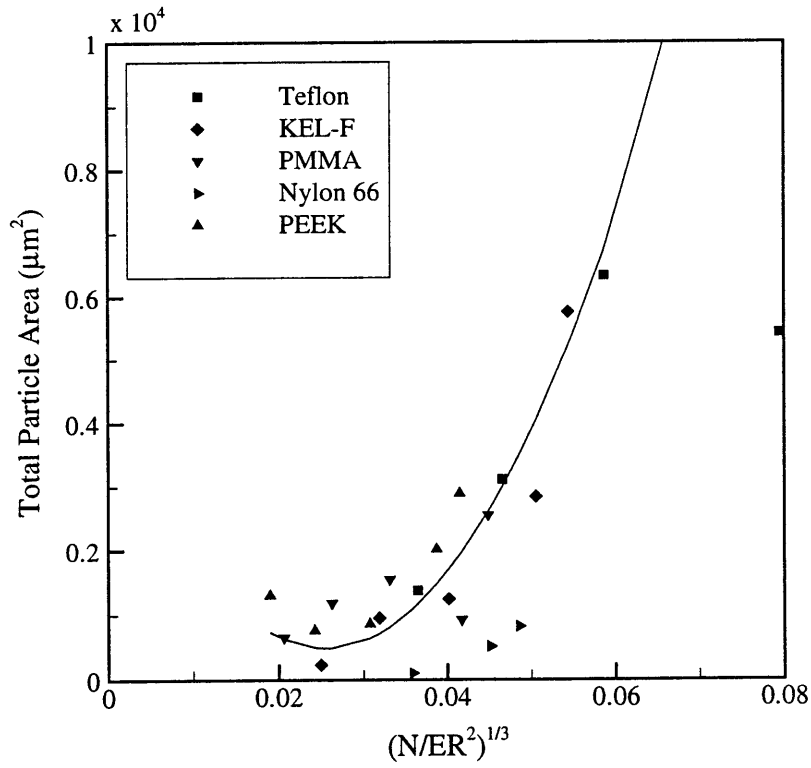
Figure 5-11: Total particle area versus $\left(\frac{N}{ER^2}\right)^{\frac{1}{3}}$.
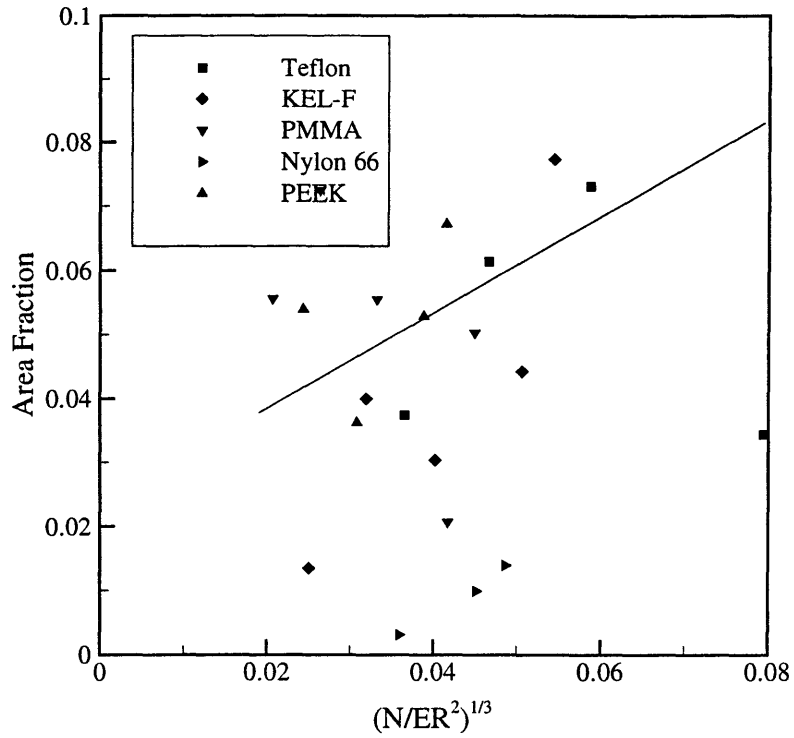
Figure 5-12: Area fraction versus $\left(\frac{N}{ER^2}\right)^{\frac{1}{3}}$.
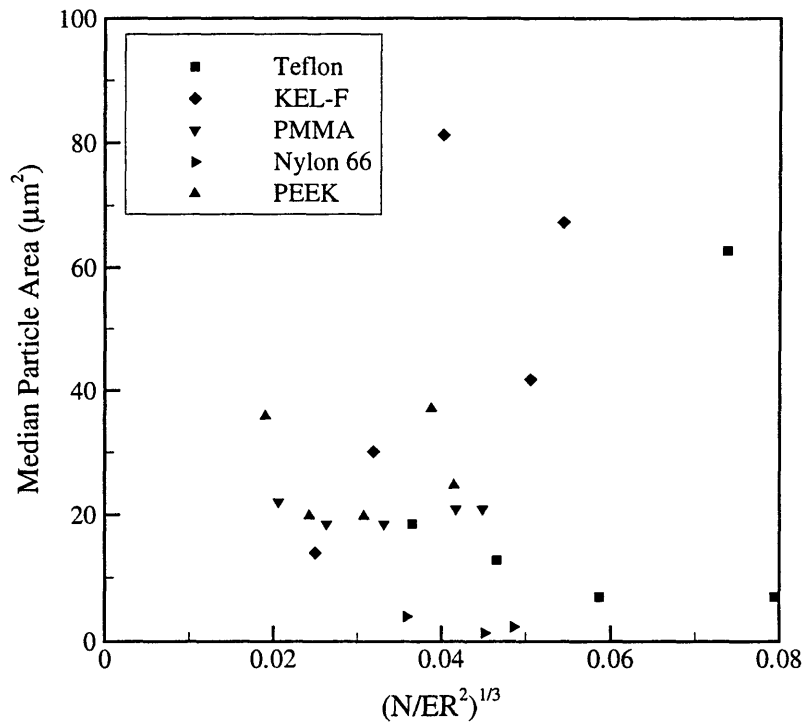
Figure 5-13: Median particle area versus $\left(\frac{N}{ER^2}\right)^{\frac{1}{3}}$. No definite trend is visible.

The tensile yield strength of the polymers, σ_Y is obtained using the relationship,

$$\sigma_Y = \frac{H}{3}$$

Therefore any trends exhibited with H will be similar to those exhibited with σ_Y. The tensile yield strength is the criterion that sets the initiation of plastic flow. All through this investigation, it is assumed that the contact between the polymer pins and silicon was elastic. Except in the case of UHMWPE, where it was shown that Hertzian elastic analysis is no longer valid as the non-dimensional roughness parameter, α was calculated to be larger than 0.05 (Section 5.3). The value of α for the other polymers was smaller than 0.05. This indicates that the contact between the polymer pin and silicon is elastic and Hertzian analysis is still valid. However, in the Greenwood-Williamson model (1966), the possibility that plastic deformation occurs at the asperities is addressed. Although, on a global scale, the contact is elastic, locally, at the asperities, there might have been plastic deformation due to the high concentration of pressure at these contact points.

If plastic deformation does occur, the real area of contact can be calculated as

$$A_{REAL} = \frac{N}{H}.$$

Particles are deposited at the contact points; therefore,

$$A_{REAL} = \text{Total Particle Area.}$$

The theoretical area fraction, which may be defined as the ratio of the total particle area and the Hertzian contact area, can be written as

$$A.F = A_{REAL} \ / \ \text{Hertzian Contact Area.}$$

Hence,

$$A.F = \frac{N}{H} \cdot \frac{1}{\pi a^2}.$$

Using the Hertz relationship for the contact radius, a, the quantity, $A.F$ is,

$$A.F = \frac{1}{\pi} \left(\frac{4}{3}\right)^{\frac{2}{3}} \cdot \left(\frac{E^*}{H}\right)^{\frac{2}{3}} \cdot \left(\frac{N}{HR^2}\right)^{\frac{1}{3}}.$$

The quantity $A.F$ was compared with the area fractions calculated from the experimental data. Figure 5-14 shows that in all cases, with the exception of UHMWPE,

the particle area fractions are smaller than that estimated by the theoretical relationship outlined above. However, in the case of UHMWPE, the particle area fractions are comparable with the theoretical values. This means that the asperities on the surface of the UHMWPE pin were deforming plastically under load. This confirms the earlier assumption that Hertzian analysis cannot be applied to UHMWPE as it is subject to plastic deformation.
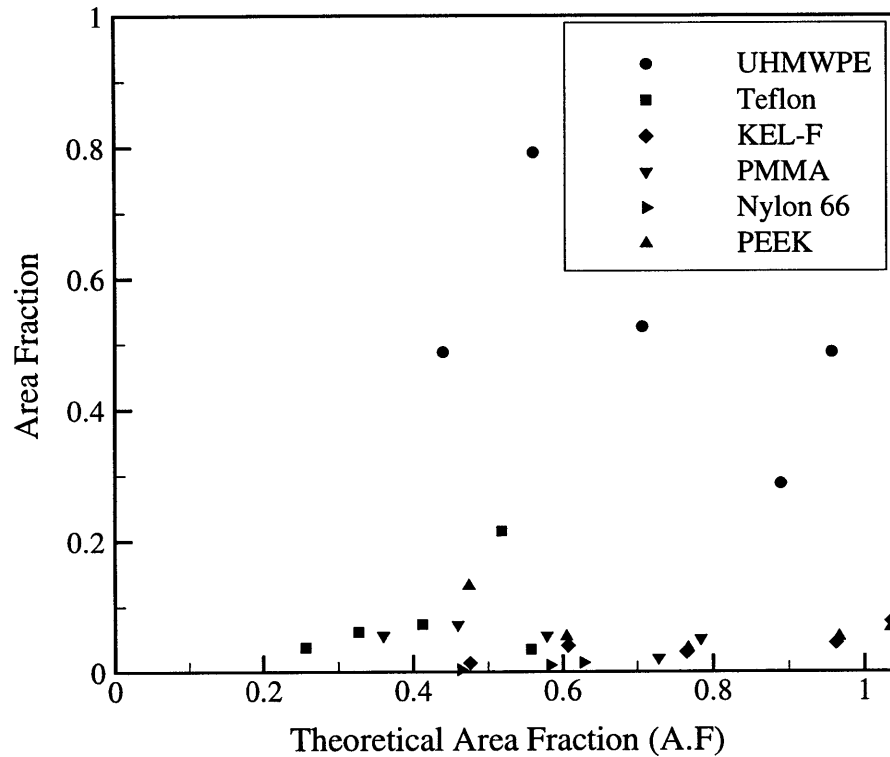
Figure 5-14: Theoretically calculated area fraction compared with that obtained from experiments.

The tensile yield strength and hardness are important if the polymers are subject to plastic deformation. It is obvious that larger loads will be required before a harder polymer deforms plastically compared with a polymer that is softer. Hence, it will be useful to use polymers with higher values of σ_Y or H so that the stresses required to initiate plastic deformation will be larger.

5.6 Summary

The material transfer from a given polymer is effected by both Hertzian contact area and pressure. The number of particles increases with load. The increase in Hertzian contact area allows more asperities touch the silicon surface. An increase in the size of the particles deposited is also observed. This may be due to the increase in Hertz pressure. The asperities are pressed further onto the surface when the pressure increases resulting in an increases in the asperity contact areas. This results in an increase in the size of the particles transferred. It appears that the total particle area is proportional to the Hertzian contact area. The slope for a straight line drawn through the points has a gradient of about 0.13.

The results suggest that surface energy is a weak variable in the material transfer phenomenon. This is because the values of surface energy of the polymers are very close to each other. Similarly, the effect of friction on material transfer could not be determined as the friction coefficient of the polymers with silicon do not vary by amounts large enough to cause discernable changes in the material transfer phenomneon.

Surface roughness is important when the non-dimensional parameter, α is greater than 0.05. In that case, as in UHMWPE, plastic deformation occurs even when the loads applied are within the elastic loading regime. When contact is elastic, slight differences in surface roughness does not affect the material transfer by large amounts. There is some indication that the size of the particles are larger when the surfaces are rougher.

The friction coefficients of the polymers are very close to each other and any variation in slip for the polymers is too small to be distinguished. It is assumed that slip may increase the amount of material transferred due to the generation of wear particles. However, no trends could be identified in this investigation.

It appears that the Young's moduli of the polymers affects the material transfer phenomenon. The number of particles decreases with higher values of Young's moduli. The total particle area also decreases with Young's modulus. This is because of a decrease in the Hertzian contact area as the Young's modulus increases. The number of asperities that touch the silicon decrease and hence the number of particles deposited decreases. No significant trend in the median particle size could be identified with the Young's modulus.

The tensile yield strength and hardness are important when plastic deformation is initiated. However, it will be useful to use polymers that have high values of tensile yield strength and hardness so that the stresses required to initiate plastic deformation are higher.

Chapter 6

Mitigating Material Transfer

Several measures that mitigate material transfer have been investigated. Experiments were carried out to determine the effects of placing polymeric films between the polymer pin and the silicon substrate. Thin films of Polyethylene, Teflon and Kapton (Polyimide) were used.

In addition, the effects of contacting the silicon substrate with ceramics, such as quartz, sapphire, and, ruby were examined. The Young's moduli of ceramics are almost two orders or magnitude greater than the Young's moduli of the polymers. Ceramics are also approximately two hundred times harder compared with the polymers.

Finally, the effect of smearing a small quantity of lubricant on the silicon substrate was also investigated.

6.1 Polymeric films

The material transfer that occurs when a Kapton film was inserted between a polymer pin and the silicon substrate was investigated. Kapton is a polyimide film manufactured by DuPont. The polymer used was KEL-F and the loads applied ranged from 0.20 N to 5.0 N. The thickness of the film used was 0.13 mm. Table 6.1 lists the properties of the film. These properties were obtained directly from DuPont. Figure 6-1 represents the scheme of the experiment.

Figure 6-2 and 6-3 indicate that no material transfer occurs from the Kapton film onto the silicon for loads of 0.2 N and 5.0 N. Similar results were obtained for the intermediate load values. Kapton is a high strength polymer. The Kapton film itself does not contaminate silicon surface but protects the silicon surface from contamination. SEM analysis was performed on the silicon substrate after a test with Kapton film at 2.0 N (Figure 6-4). Although some foreign objects are evident (bright spots on the figure), the EDX test carried out on the substrate indicates that the only element present on the substrate is silicon (Figure 6-5). Kapton which is composed

Table 6.1: Physical properties of Kapton.

Kapton	
Young's Modulus, E (GPa)	2.5
Poisson's Ratio	0.34
Tensile Yield Strength, σ_Y, (MPa)	231
Hardness, H, (MPa)	693

of hydrogen, carbon, and nitrogen, was not detected using EDX.

One of the reasons for the lack of transfer from Kapton may be because of its high strength. The tensile yield strength values for the other polymers are approximately 30 MPa. However, the tensile yield strength for Kapton is about ten times greater than this. The effect of using other polymeric films which are weaker than Kapton was investigated. Polyethylene (cling-film) and Teflon films were tested for material transfer at a load of 5.0 N. Figures 6-7 and 6-8 indicate that there is transfer from these films onto the substrate. The effect of using a polyimide pin was also tested. Figure 6-6 indicates that there is transfer from the polyimide pin to the substrate under a normal load of 5.0 N. This suggests that material transfer is mitigated if a thin film is used compared to a polymer pin. However, using thin films alone will not mitigate material transfer. The effect of using other polymeric films which are weaker than Kapton was investigated. Polyethylene (cling-film) and Teflon films were tested for material transfer at a load of 5.0 N. Figures 6-7 and 6-8 indicate that there is transfer from these films onto the substrate. These results suggest that material transfer may be mitigated with the use of a thin film of high strength.

The reason for the importance of thin films for mitigation may be due to the smoothness and homegeneity of thin films. The cohesive forces in the smooth Kapton film are more uniform compared with the polymer pins which may have areas where the forces are weaker due to material inhomogeneity. Hence, it will be more difficult to "pluck" material from the surface of the smooth Kapton film compared with that the other polymer pins.

Figures 6-9 and are AFM pictures of the surface of a Kapton film. Figures 6-11 and 6-12 are AFM pictures of the spherical tip of a KEL-F pin. The figures indicate that the Kapton film is smoother (RMS Roughness = 319 Å) and more homogeneous than the curved surface of the KEL-F pin (RMS Roughness = 4766 Å). The scan size for both figures are 20 μm x 20 μm. Figure 6-13 is an AFM image of the Kapton film for a smaller scan size (1.0 μm x 1.0 μm). Again, the surface appears to be smooth and homogeneous.

The results obtained for Kapton suggest that a combination of high strength and

material homogeneity will effectively mitigate material transfer.
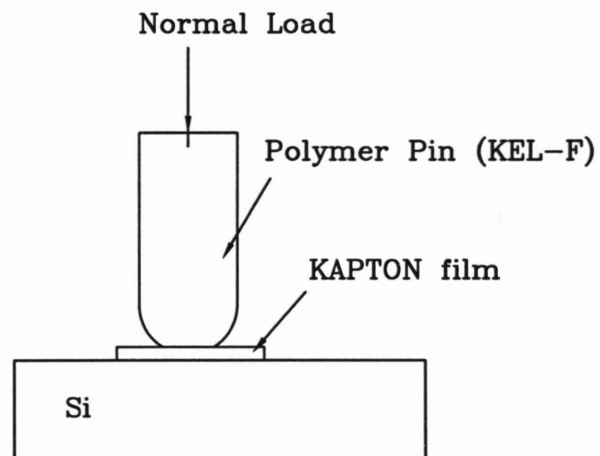
Figure 6-1: Schematic of experiment with Kapton.
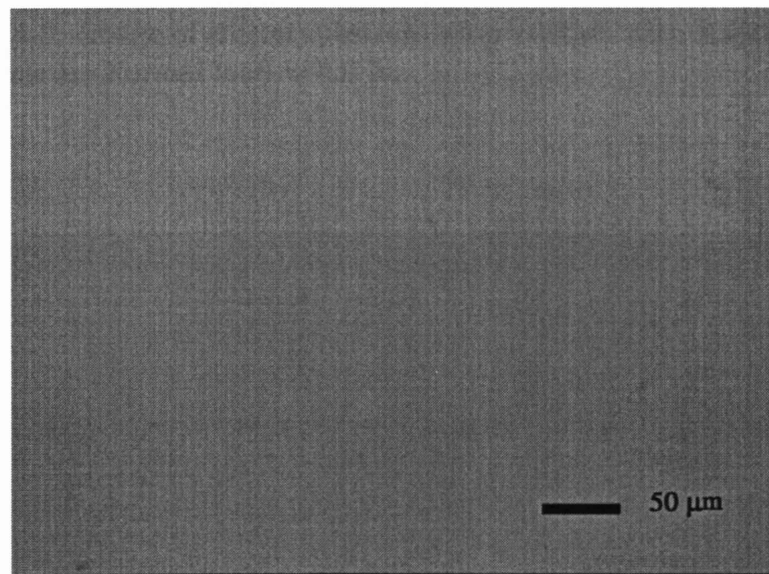
Figure 6-2: Image of silicon substrate after contact with Kapton. Normal load = 0.2 N.
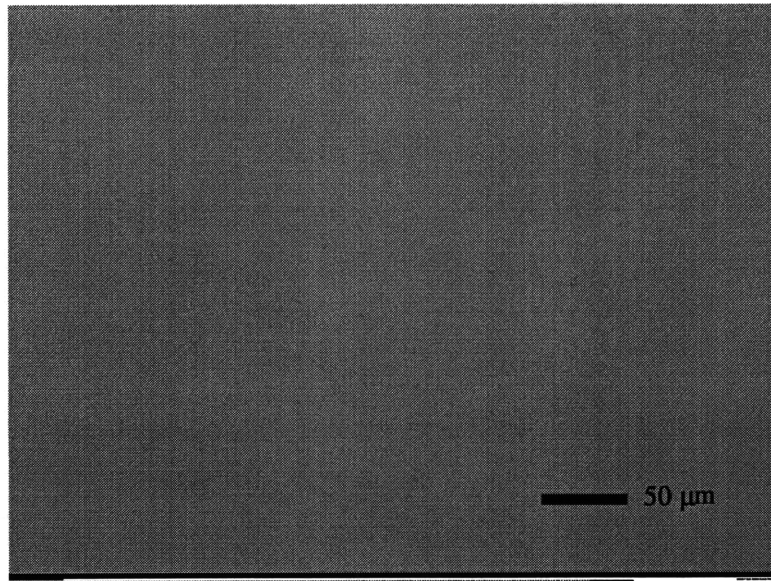
Figure 6-3: Image of silicon substrate after contact with Kapton. Surface is clean. Normal load = 5.0 N.
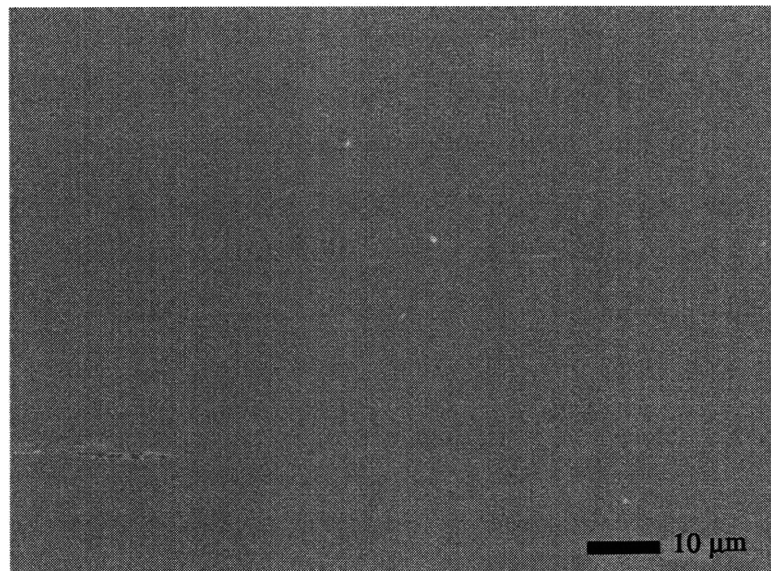
Figure 6-4: SEM micrograph of silicon surface after test using Kapton film. Normal load = 2.0 N. The bright spots indicate that some foreign objects were present on the surface. However, EDX analysis confirmed that no material transfer from Kapton had occured.
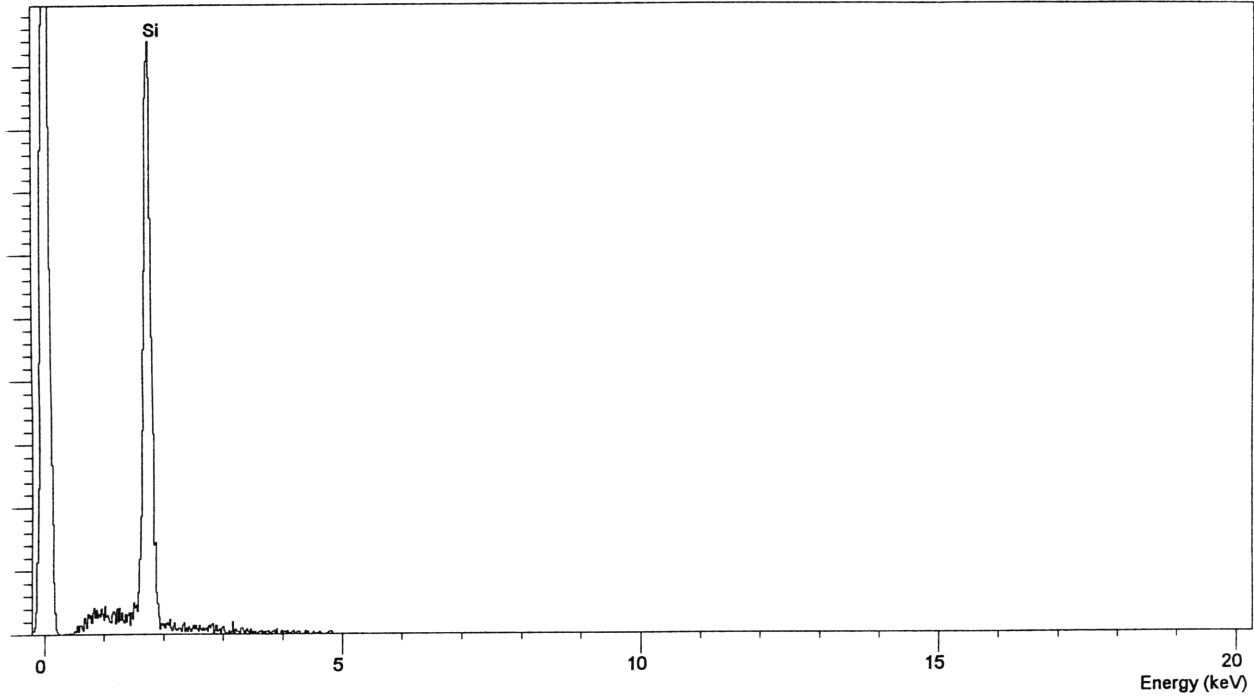
Figure 6-5: EDX analysis of silicon surface after test using Kapton film. Silicon is the only element detected.
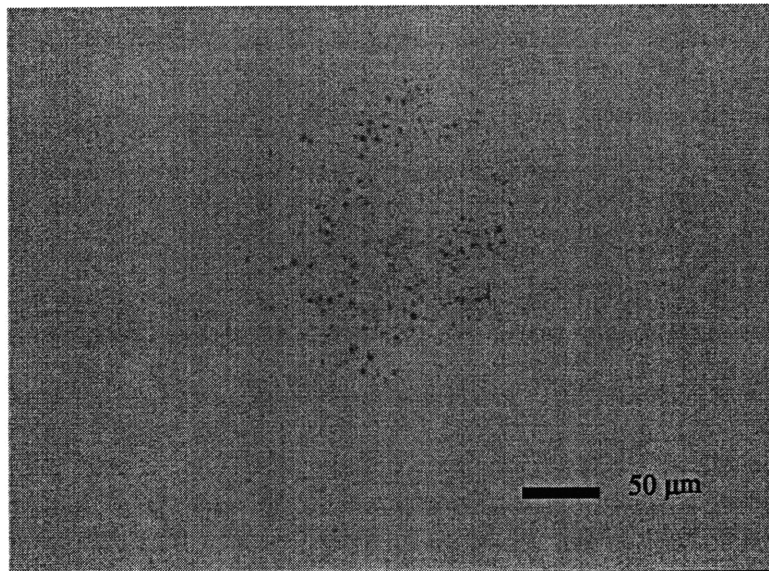
Figure 6-6: Image of silicon substrate after contact with a polyimide pin. There are traces of material transfer on silicon. Normal load = 5.0 N.
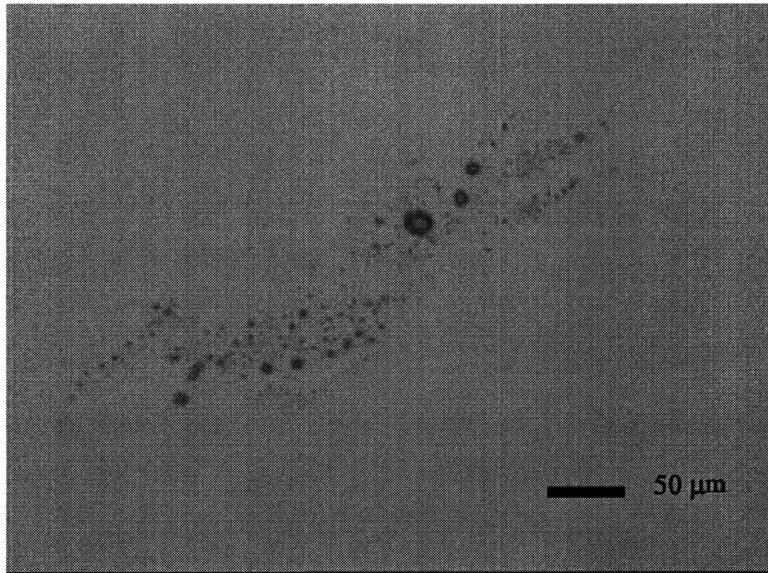
Figure 6-7: Image of silicon substrate after contact with Polyethylene film (cling-film). Thickness of film used was 0.05 mm. There are traces of material transfer on silicon. Normal load = 5.0 N.
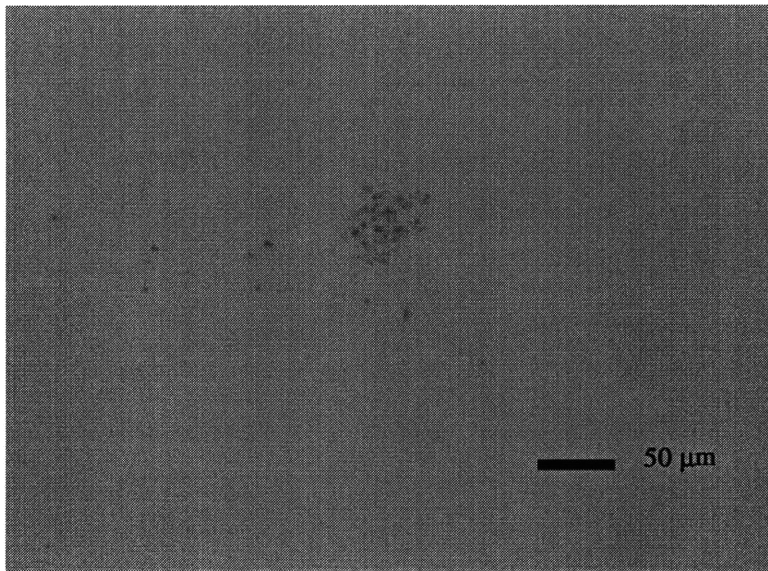
Figure 6-8: Image of silicon substrate after contact with Teflon film. Thickness of film used was 0.20 mm. There are traces of material transfer on silicon. Normal load = 5.0 N.
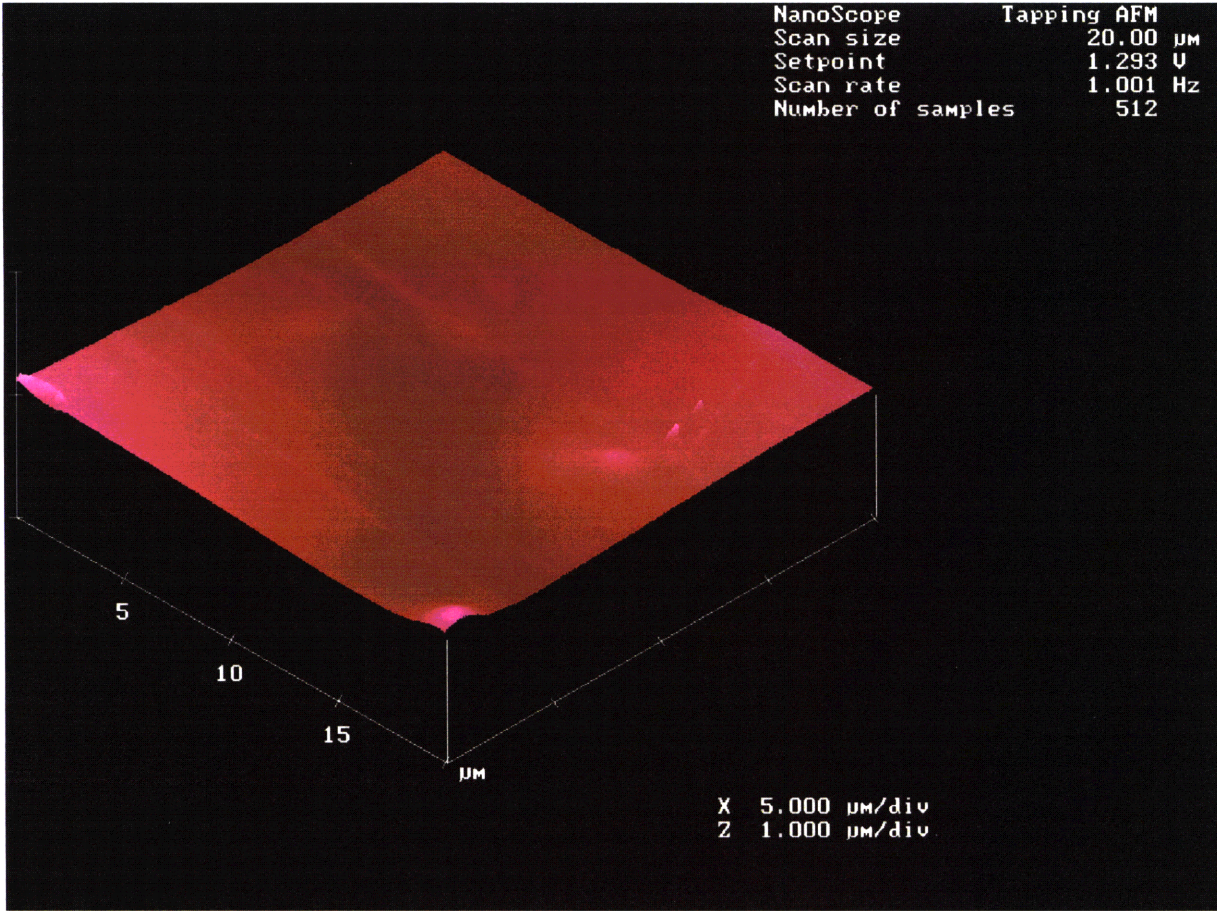
Figure 6-9: AFM image of the surface of Kapton film.
Scan size = 20 μm x 20 μm.
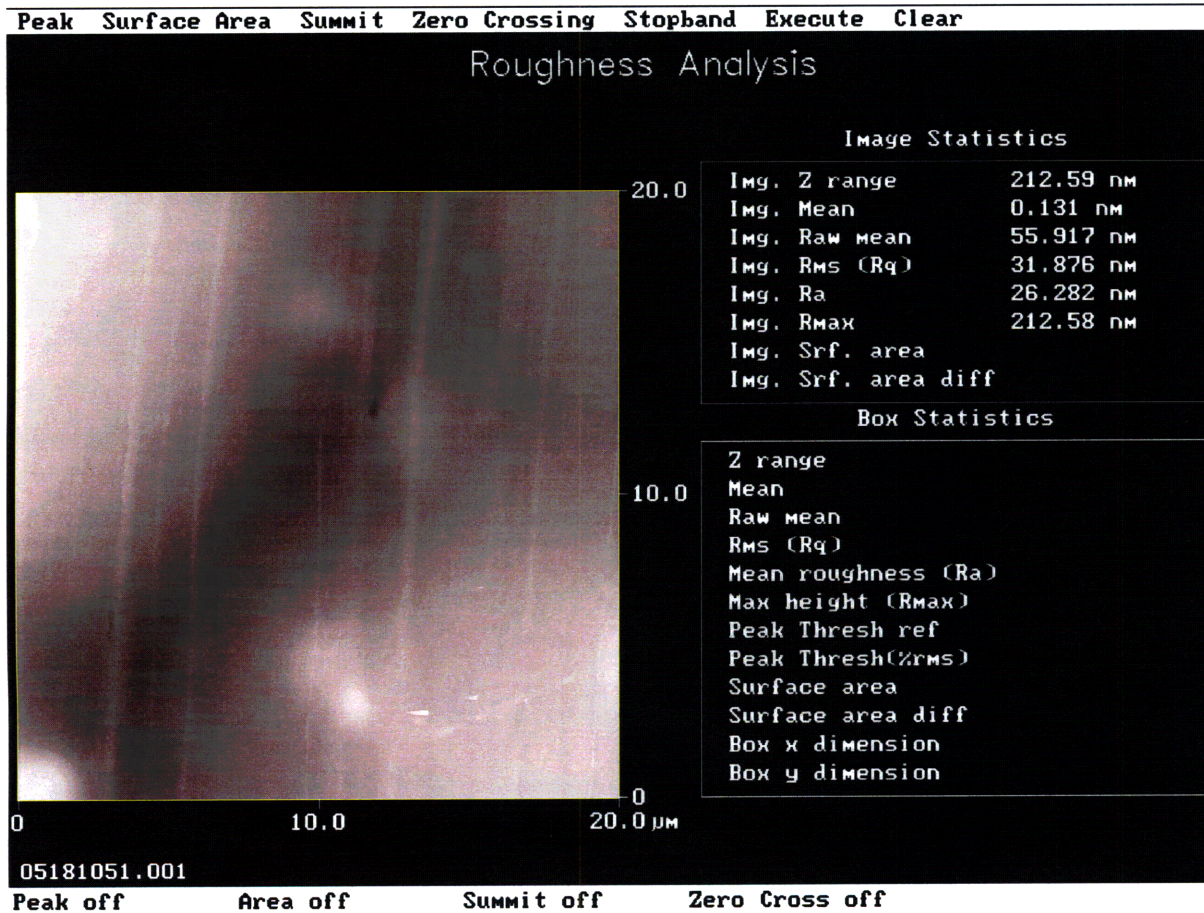
Figure 6-10: Roughness analysis of the surface of Kapton film. Scan size = 20μm x 20μm.

NanoScope   Tapping AFM
Scan size   20.00 µm
Setpoint   0.6637 V
Scan rate   0.2001 Hz
Number of samples   256

X 5.000 µm/div
Z 1.000 µm/div
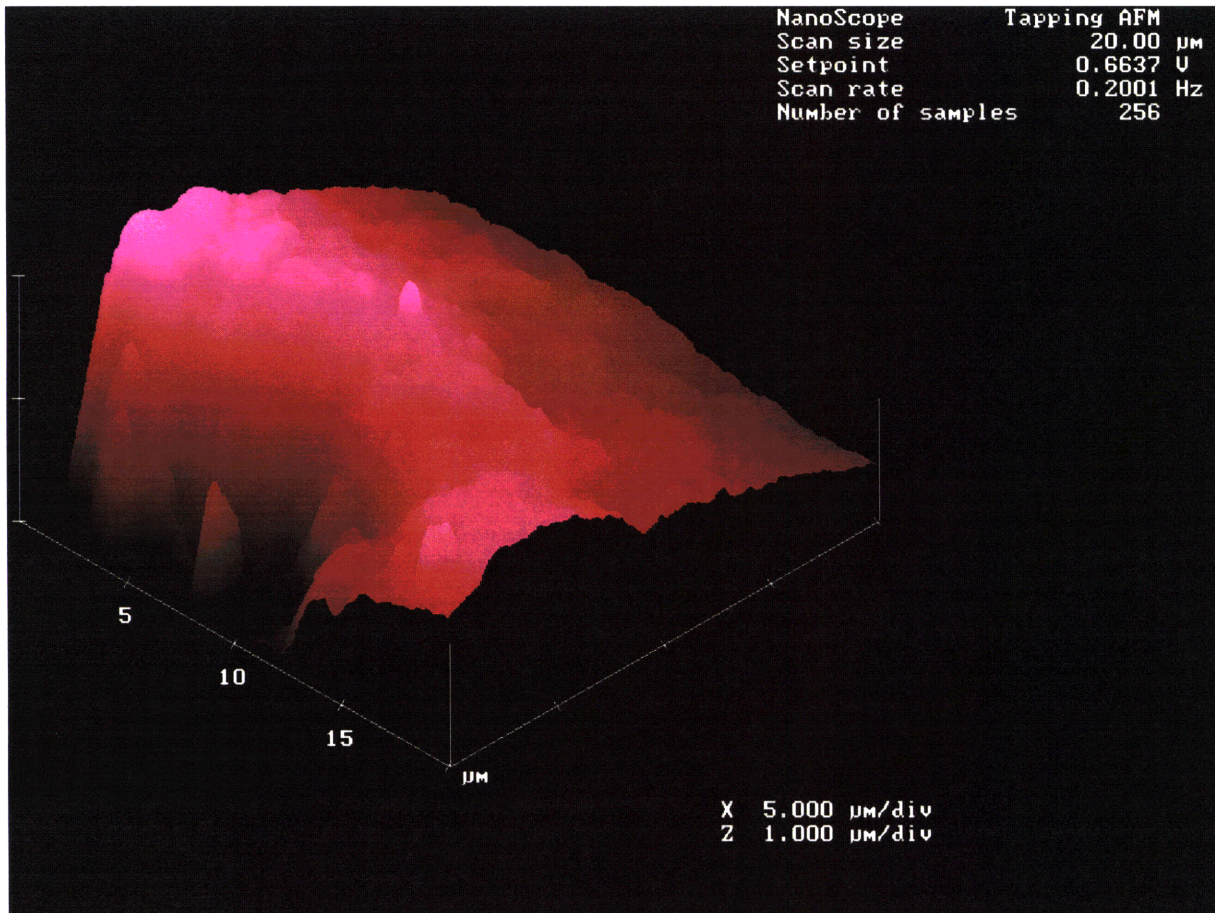
Figure 6-11: AFM image of the spherical tip of KEL-F pin.
Scan size = 20 µm x 20 µm.
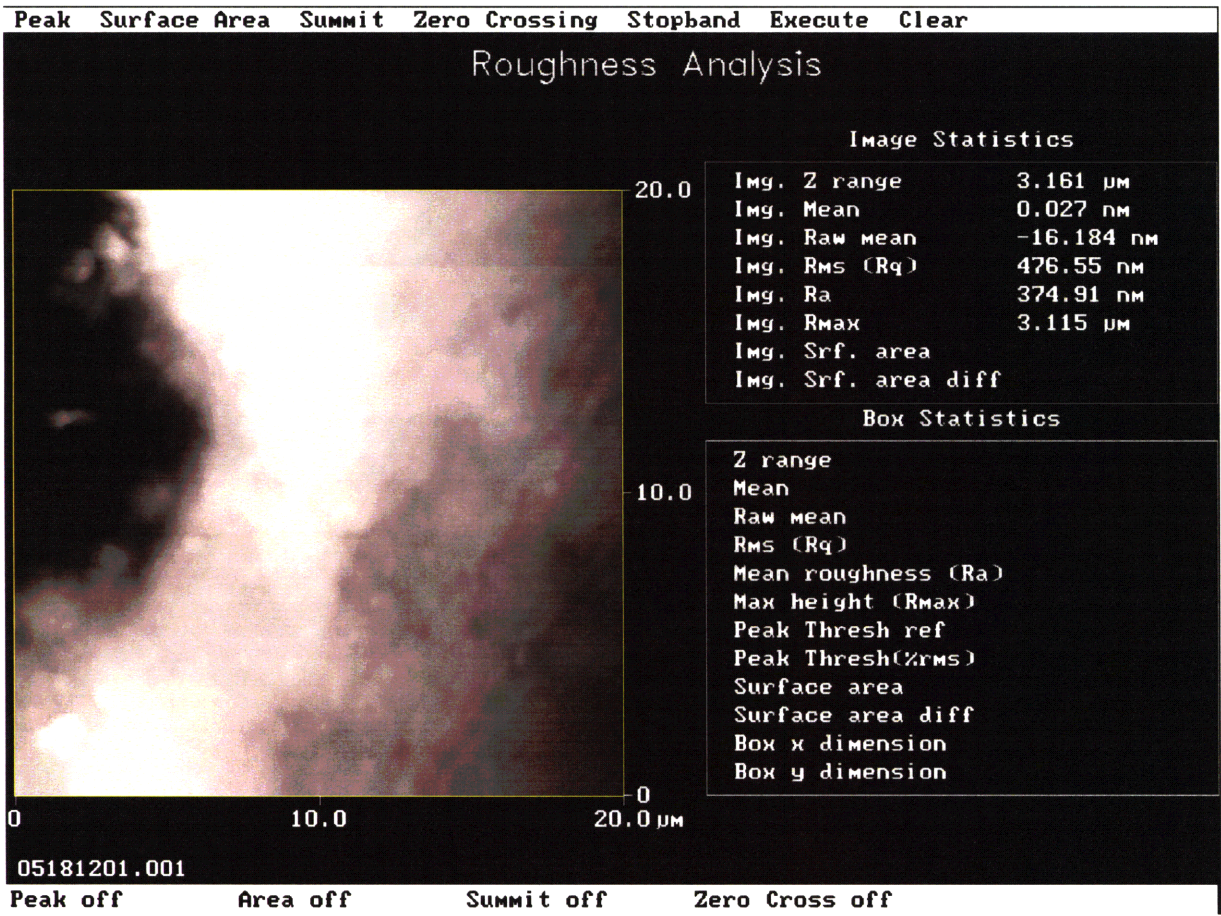
Figure 6-12: Roughness analysis of spherical KEL-F pin tip.
Scan size = 20 μm x 20 μm.
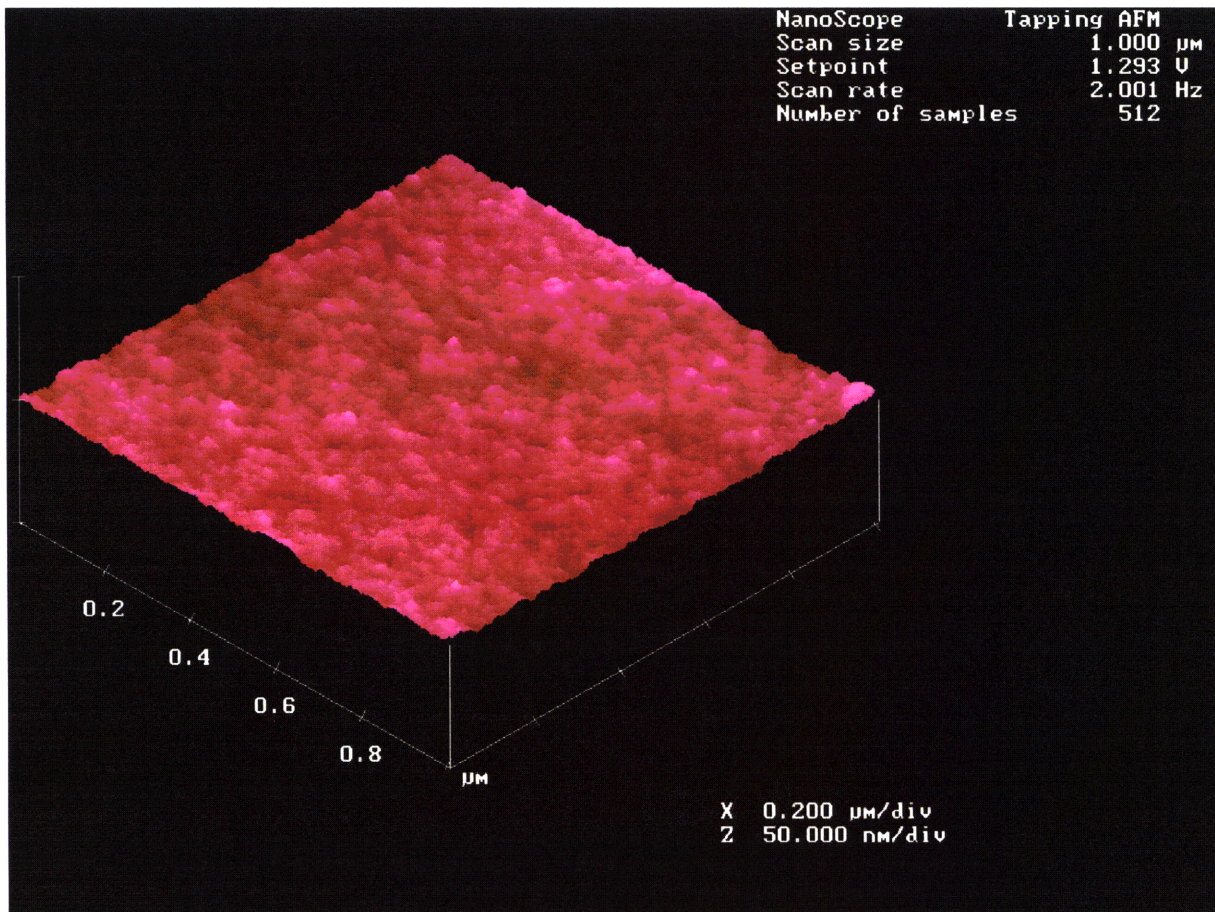
Figure 6-13: AFM image of the surface of Kapton film.
Scan size = 1.0 μm x 1.0 μm.

6.2 Ceramics

The plano convex quartz lenses (diameter = 12.70 mm, radius of curvature = 22.923 mm) were purchased from Edmund Scientific and have been manufactured using research grade synthetic fused silica (SiO_2). The sapphire and ruby are highly polished ball lenses (6.35 mm in diameter, purchased from Edmund Scientific) consist of Al_2O_3. Ruby owes its red color to traces of chromium oxide. While the physical and chemical properties of both are the same, sapphire and ruby are distinguishable by their optical properties. Table 6.2 lists the properties of the ceramics used. These properties were obtained directly from Edmund Scientific and were comparable to those found in handbooks on ceramic properties [American Society for Metals, 1987]. The hardness of the fused silica lens, however, was measured using a Vickers hardness tester.

Table 6.2: Physical properties of quartz, sapphire, and, ruby.

Fused Silica (SiO_2)	
Young's Modulus, E, (GPa)	72.9
Poisson's Ratio	0.17
Hardness, H, (MPa)	$9,967 \pm 1,246$
Sapphire, Ruby (Al_2O_3)	
Young's Modulus, E, (GPa)	346.9
Poisson's Ratio	0.3
Hardness, H, (MPa)	20,600

Figures 6-14, 6-15, 6-16, are the images of the silicon substrate after contact with the fused silica lens at 0.5, 2.5, and, 3.0 N respectively. Tests done at 1.5 N and 2.0 N yielded similar results to those conducted at 0.5 N. It is clear that at low loads (< 2.0 N), no material transfer is evident but at higher loads, material transfer occurs. The hardness of the silica lenses are comparable to the hardness of the silion substrates. Hence, no transfer of material from silica is evident at low loads. However, transfer does occur at loads of 2.5 N and 3.0 N. The transferred fragments appear to be distributed in the shape of a circular ring. Within the contact area, the stresses are all compressive except at the periphery where the radial stress is tensile. It is this area, from which, material transfer occurs.

Figures 6-17 and 6-18 are optical micrographs of the silicon substrate after contact with sapphire. The loads used were 1.0 N and 3.0 N respectively. No sapphire particles were present on the surface of the silicon. Similar results were observed using ruby

(Figure6-19, 6-20) under similar loading conditions. Sapphire and ruby have values of Young's Modulus, tensile yield strength and hardness which are higher than those of silicon. Hence, no transfer of sapphire or ruby particles occur. The silicon surfaces were inspected for any scratches caused by contact with sapphire and ruby. The surfaces, as depicted in the figures, were clean and scratch free.

Figure 6-14: Image of silicon substrate after contact with fused silica. Surface appears to be clean and free of transferred fragments. Normal load = 0.5 N. Estimated Hertzian contact radius = 55.4 μm.
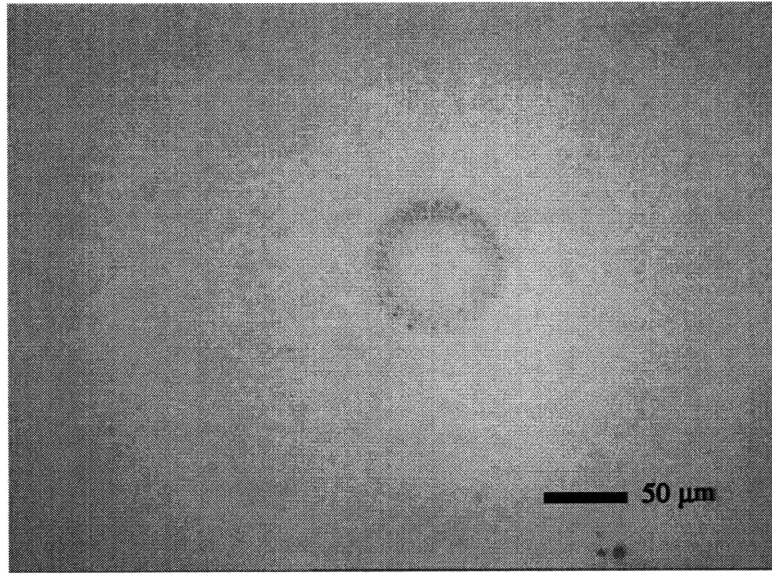
Figure 6-15: Image of silicon substrate after contact with fused silica. Some transferred fragments are observed, arranged in the shape of a ring. Normal load = 2.5 N. Experimental contact radius = 94.6 μm.
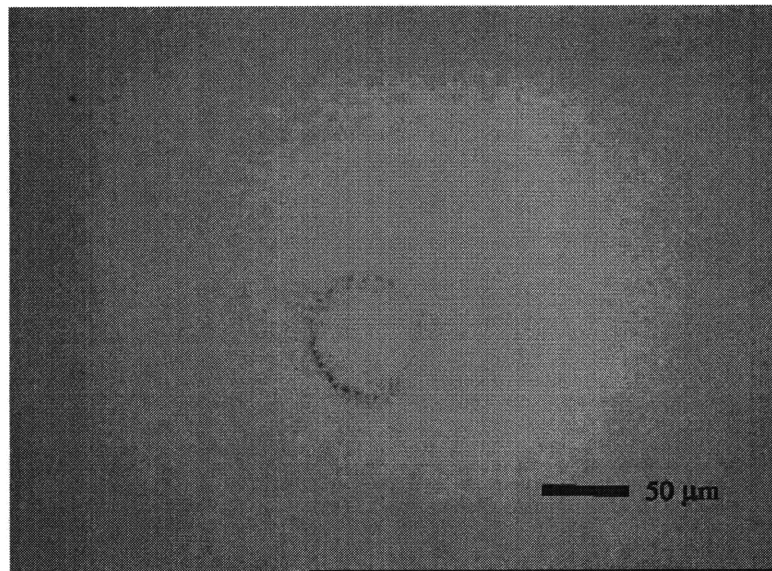
Figure 6-16: Image of silicon substrate after contact with fused silica. Some transferred fragments are observed, arranged in the shape of a ring. Normal load = 3.0 N. Estimated Hertzian contact radius = 100 μm.
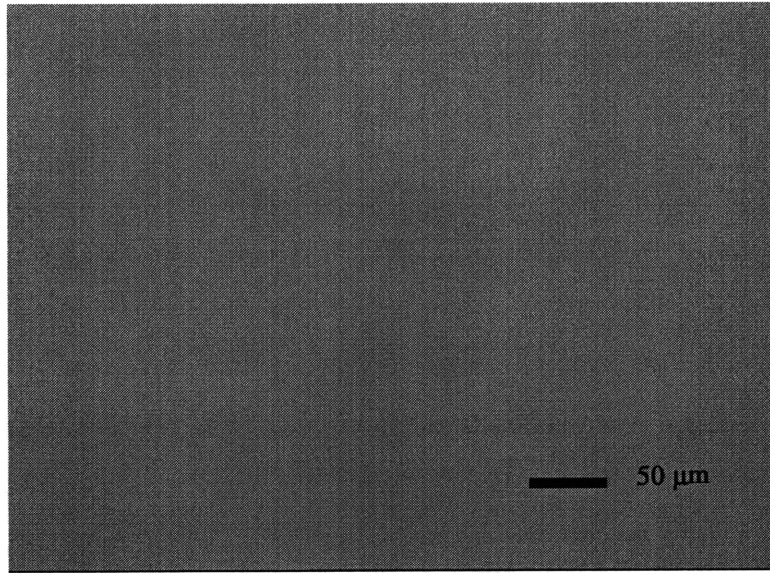
Figure 6-17: Image of silicon substrate after contact with sapphire. Surface appears to be clean and free of transferred fragments. Normal load = 1.0 N. Estimated Hertzian contact radius = 27.2 μm.
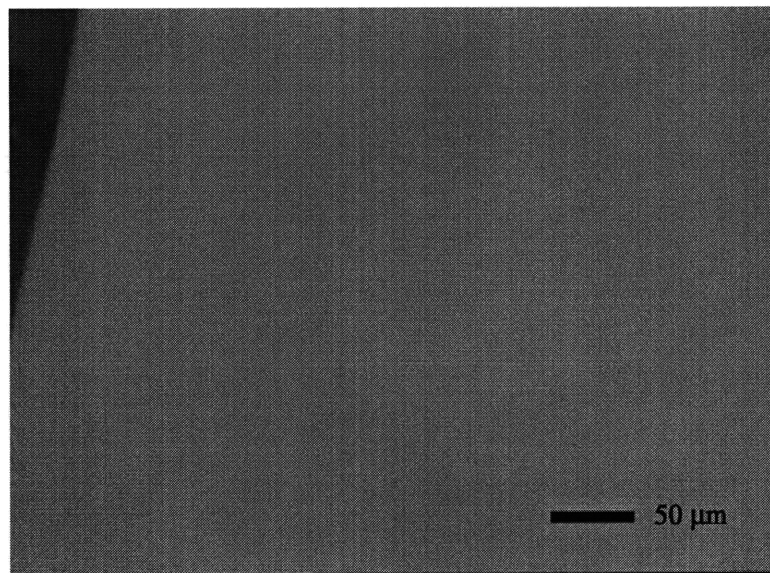
Figure 6-18: Image of silicon substrate after contact with sapphire. Surface appears to be clean and free of transferred fragments. Normal load = 3.0 N. Estimated Hertzian contact radius = 39.3 μm.
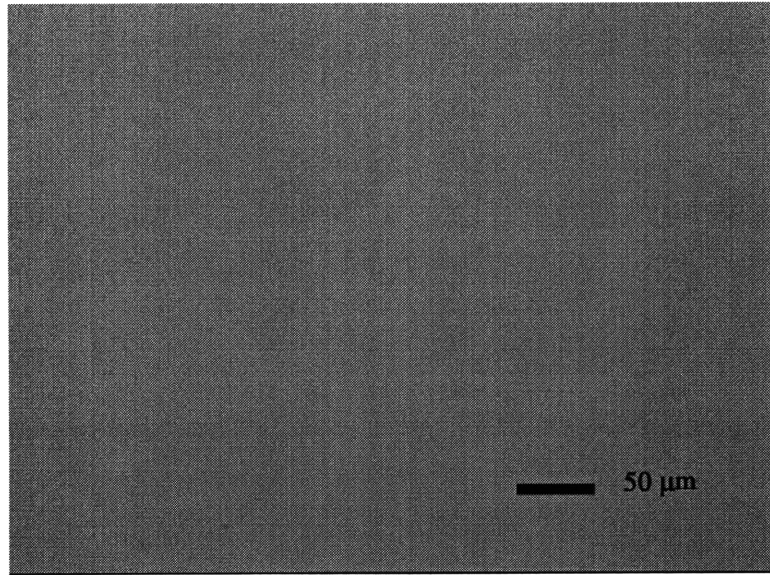
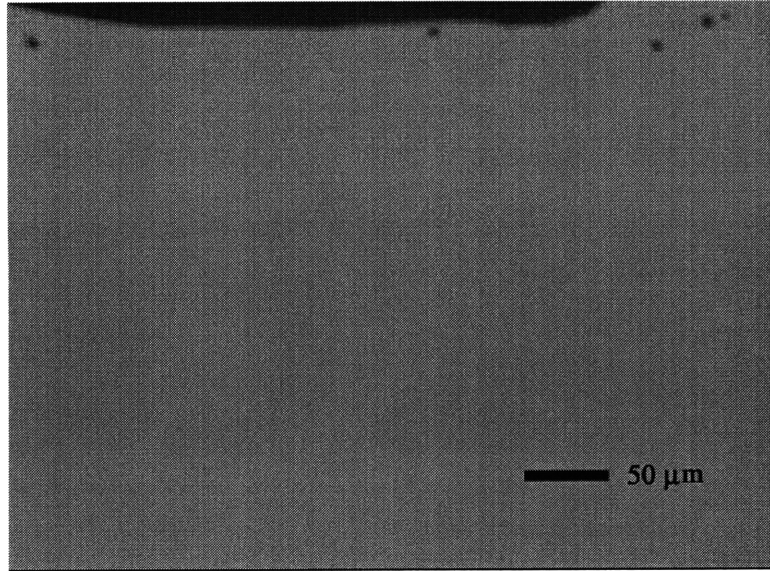Figure 6-19: Image of silicon substrate after contact with ruby. Surface appears to be clean and free of transferred fragments. Normal load = 1.0 N. Estimated Hertzian contact radius = 27.2 μm.
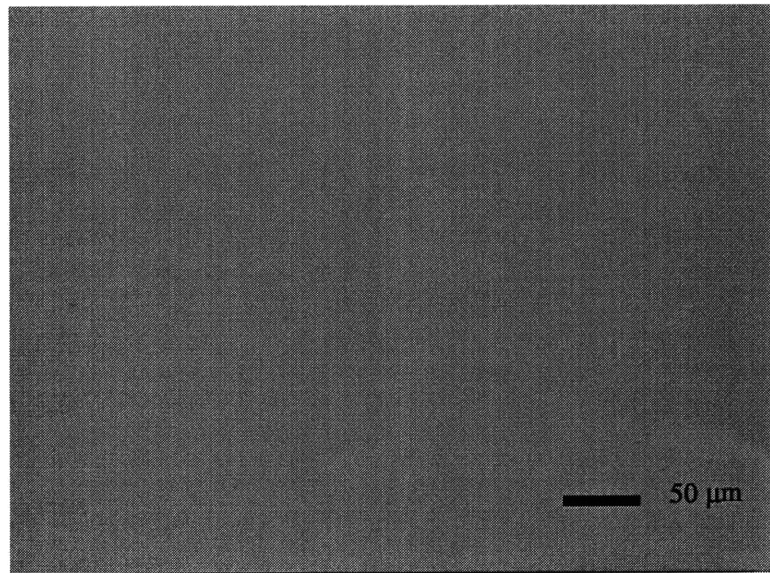
Figure 6-20: Image of silicon substrate after contact with ruby. Surface appears to be clean and free of transferred fragments. Normal load = 3.0 N. Estimated Hertzian contact radius = 39.3 μm.

6.3 The Use of Lubricant

The use of lubrication to mitigate material transfer from polymer to silicon surfaces has also been investigated. The experimental results obtained using a KEL-F pin and dodecane as the lubricant, indicate that the use of lubricant effectively reduced the material transfer. Figure 6-21 is the image of the material transfer from the KEL-F pin when lubrication had not been applied. In Figure 6-22, the image obtained with the use of lubrication is represented. Comparison of the figures suggests that material transfer has been mitigated; the KEL-F particles that can be seen in Figure 6-21 are not visible in Figure 6-22. Lubrication successfully mitigates material transfer because the polymer pin is no longer in direct contact with the silicon substrate. Similar to the comcept of using a polymeric film, the lubricant protects the silicon surface from contamination.

The success of this scheme depends largely upon the type of lubricant used, and the manner in which the method is incorporated into the photoresist spin coating process. A proposed method to implement the use of lubrication is to use the vacuum chuck itself as the source of lubrication. The idea is to fabricate the vacuum chuck so that it can store lubricant. A thin film lubricant layer forms when the silicon wafer makes contact with the chuck. Hence, the need to continuously supply lubrication from an external source is eliminated. This scheme can be realized if the chuck consists of small pores, of the order of micrometers, in which the lubricant is stored. Due to capillary action, the lubricant film spreads, continuously replenishing the supply of lubrication on the surface of the chuck.

The mitigation scheme has been tested using a porous polyurethane pad. The experimental scheme is similar to that in Figure 6-1 except that the Kapton film is replaced with a lubricant soaked polyurethane pad. The material transfer from a small piece of polyurethane pad was studied (Figure 6-23). This material transfer was compared with that from a polyurethane pad that was soaked in dodecane (Figure 6-24). The images indicate that there is a reduction in the material transfer with the use of a lubricant soaked pad.
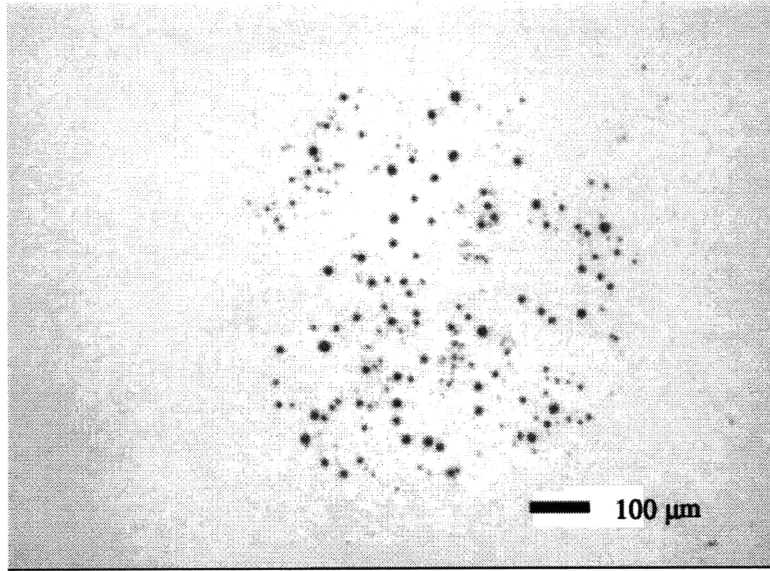
Figure 6-21: Material transfer from KEL-F to silicon. Normal load = 5.5 N.
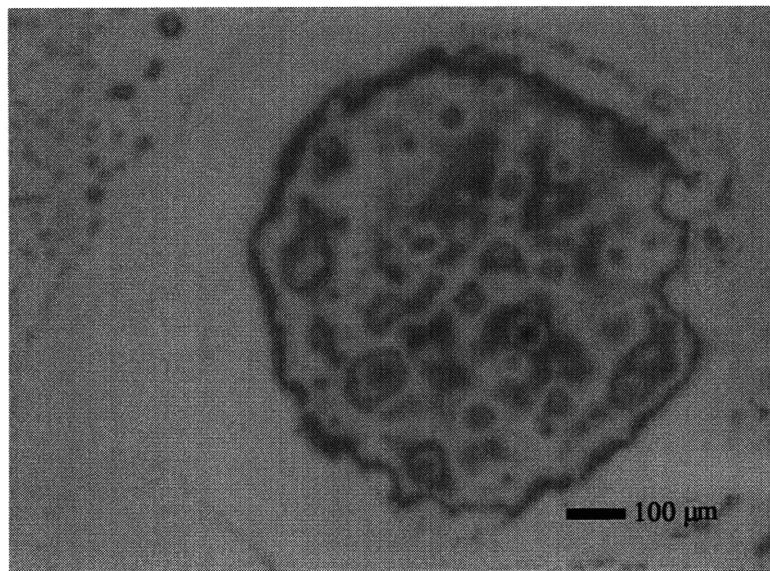
Figure 6-22: Material transfer from KEL-F to silicon with dodecane. Normal load = 5.5 N.
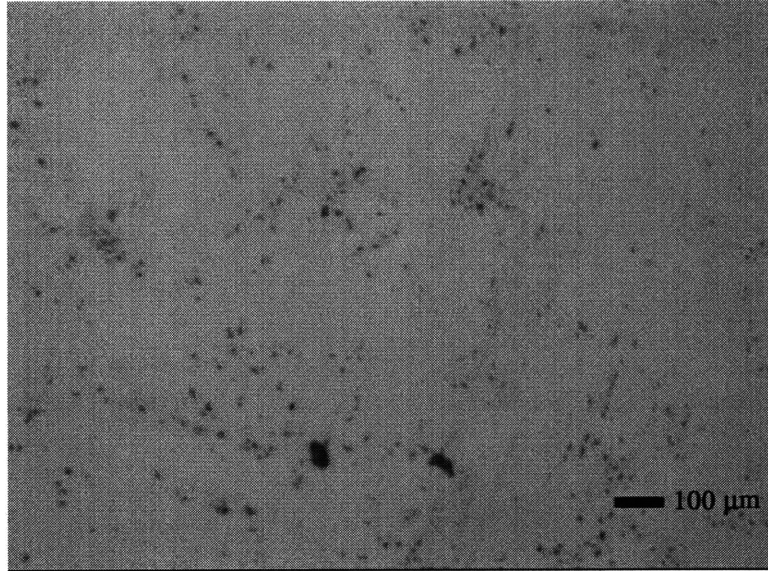
Figure 6-23: Material transfer from a polyurethane pad to silicon. Normal load = 5.5 N.
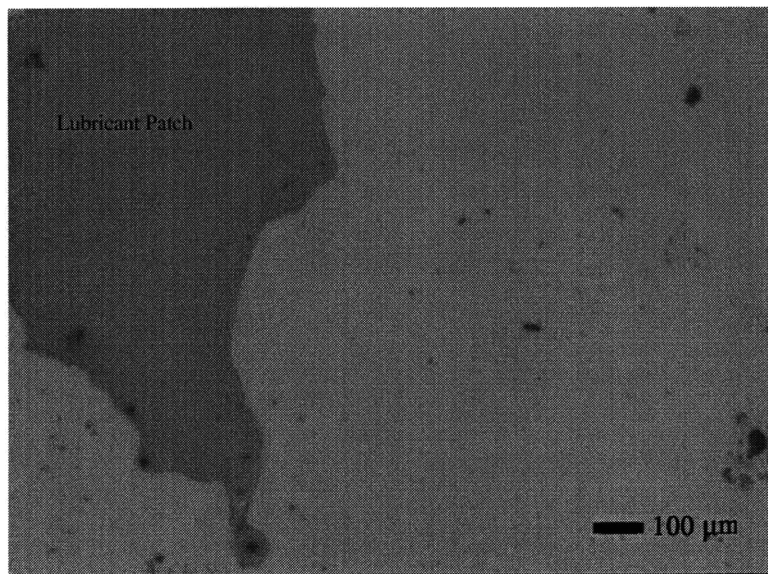
Figure 6-24: Material transfer from a polyurethane pad soaked in dodecane to silicon. Normal load = 5.5 N.

6.4 Summary

Several steps can be taken to reduce, if not completely eliminate, the problem of backside contamination. Experiments with Kapton suggest that Kapton films could be inserted in between the polymer vacuum chuck and the silicon wafer. As observed in the experiments, neither KEL-F particles nor Kapton particles were deposited on silicon. Thus, the use of a thin Kapton film can prevent particle deposition on the backside of the silicon wafer.

The vacuum chuck could be fabricated from a very strong, hard material such as a ceramic. However, this may not be economically feasible nor is easily manufactured. The use of ceramics could be implemented by coating the surface of the chuck with a ceramic. As demonstrated in the experiments, at large loads, material transfer does occur from silica while no transfer was detected, even at large loads, from sapphire and ruby. Hence, chucks coated with Al_2O_3 will more effectively mitigate transfer compared with those coated with SiO_2. Alternatively, the chuck may be lubricated, provided the lubrication scheme can be successfully implemented without interfering with the photoresist process itself.

Chapter 7

Conclusions

Experimental results have identified certain trends in the material transfer phenomenon. Also, several measures that mitigate material transfer have been proposed and experimentally verified.

- The measured contact radius is comparable to that predicted by Hertzian analysis. UHMWPE is an exception, however. The contact radius is almost 1.5 times greater than the Hertzian contact radius. This deviation is due to the plastic deformation of the UHMWPE pin.

- Images of the material transferred to the silicon surface suggest that contact occurs between the asperities on the curved surface of the polymer pins and silicon. The distribution of the particle area from a particular polymer is non-gaussian. There are a large number of small particles. The size of these small particles approach the resolution of the image analysis system. This is 1.5 μm for low magnification and 0.8 μm for high magnification. The distribution of the particle area from a particular polymer is non-gaussian.

- SEM and EDX confirmed that the material transfer consists of micrometer sized polymer particles. The average diameter of the transferred fragments are about 8 μm. AFM investigation has revealed that the transferred fragments are pancake-like; the height of the particles is almost a hundred times smaller than the diameter.

- Material transfer from KEL-F with variation in load indicates that there is an increase in the number as well as the size of the particles at higher loads. At higher loads, the Hertzian contact area is greater and thus more asperities make contact with the silicon. The slight increase in the median particle size may be due to the increase in the Hertzian contact pressure. There is an increase in the asperity contact area when the asperities are pressed further onto the surface of the silicon. The total particle area increases linearly with the Hertzian contact area with a slope of 0.13. The plot of area fraction against Hertzian contact area produces a constant horizontal line.

- The effect of surface energy on material transfer appears to be weak. The surface energies of the polymers are very close to each other, in the range 0.02 - 0.05 J/m^2, and the surface energy of silicon at room temperature is 1.27 J/m^2. Since the surface energy of silicon is so much higher than those of the polymers, surface energy effects of the polymers on the material transfer cannot be easily discerned.

- Surface roughness is important only when the non-dimensional roughness parameter, α is greater than 0.05, in which the Hertzian analysis is no longer valid. This was the reason for plastic deformation of UHMWPE although the loads applied were in the elastic regime. The RMS surface roughness of UHMWPE was 1459.4 Å. The RMS surface roughness of the other polymers were in the range 300 - 700 Å. The value of α for UHMWPE was calculated to be 0.1, which is larger than 0.05. The assumption that UHMWPE was subject to plastic deformation was further confirmed when the total particle area deposited was comparable to the theoretical real area of contact that was computed on the basis thatasperity plastic deformation had been initiated. For the other polymers, the total particle area was about ten times smaller than the theoretically predicted real area of contact.

- The effect of variations in surface roughness on material transfer when contact was still elastic was investigated. PMMA pins were roughened to varying degrees with sandpaper. For all the pins, the parameter α was kept below 0.05. The results suggest that there is not a great deal of variation in the material transfer with surface roughness when contact is elastic. However, in general, there appears to be an increase in the area fraction for rougher surfaces. For example, the area fraction of the material transfer from a PMMA pin of RMS roughness of 283 Åwas 0.03. For a rougher pin, with a RMS roughness of 599 Å, the area fraction increased to 0.09. This increase in area fraction was due to the increase in the size of the particles deposited. For the material transfer from the smoother pin, the median particle area was 10.02 μm^2. This increased to 54.44 μm^2 for the material transfer from the rougher pin.

- The results suggest that the effect of friction is marginal. The primary reason for this is that the friction coefficients of the polymers are very close to each other. in the range 0.1 to 0.4. A better idea of the effects of friction may possibly be determined by conducting experiments at elevated temperatures, for friction and wear coefficients of polymers increase with an increase in temperature (Appendix A).

- It has been observed that there is a decrease in the number of particles transferred and the total particle area, with an increase in Young's modulus because an increase in the Young's modulus decreases the Hertzian contact. Therefore, the number of particles and the total particle area decrease for the number of asperities that make contact decreases. No significant trend could be identified for the median particle size when plotted against the Young's modulus. The

effect of yield strength and hardness are negligble as elastic deformation occcrs in all the polymers except UHMWPE.

- Kapton did not cause material transfer. Kapton is a high strength polymer with a tensile yield strength of about 231 MPa, which is approximately ten times greater than the tensile yield strength of the other polymers. The results were confirmed using SEM. The lack of material transfer is due to the homogeneity of the Kapton film. In a bulk polymer, there may be areas where the polymer is weak. Hence, material can be easily "plucked" from these areas. However, homogeneity alone will not mitigate transfer as tests on Polyethylene and Teflon films exhibited material transfer had occurred. Thus, a combination of high strength and homogeneity can successfully reduce material transfer. There is no material transfer from ceramics and when a small amount of lubricant is smeared on the silicon surface.

Based on the present research, several measures that will mitigate backside contamination are proposed. Using low loads can reduce the number and the size of the particles transferred. Also, it will be useful to fabricate the chuck from a material with high Young's modulus. This will reduce the Hertzian contact area and minimize transfer. The surface of the chuck must be fairly smooth. Steps must be taken to ensure that the RMS roughness of the chuck is not greater than 100 Åmay reduce the total particle transfer. High-strength, homogeneous polymers can also be used. For instance, covering the vacuum chuck with a layer of Kapton will mitigate transfer. Alternatively, the chuck may be coated with a ceramic. Lubrication is also viable, if only it does not interfere with the application of the photoresist film.

Appendix A

Friction and Wear of Selected Polymers

A study on the friction and wear behavior of certain polymers was conducted at and above room temperature. There is a critical temperature for polymers above which there is a drastic change in mechanical properties of the polymers such as Young's modulus and tensile yield strength. The polymers tested were polymethylmethacrylate (PMMA), polytetrafluoroethylene (Teflon), polypropylene and a glass-reinforced polyester. The substrate was silicon. A pin-on-disk friction testing apparatus was used to determine the friction and wear coefficients. For Teflon and PMMA, there was a sudden jump in the friction coefficient when the temperature exceeded the glass transition temperature of these polymers. However, the increase of the wear coefficient with temperature was more gradual. This gradual increase in the wear coefficient was observed for all the polymers tested. It is proposed that the friction mechanism is adhesion and the wear rate mechanism is delamination. At the glass transition temperature, the hardness of the polymer undergoes a large change and this causes a sudden increase in friction. The increase in wear coefficient is more gradual as hardness does not affect delamination to the extent that it does adhesion.

A.1 Introduction

This work is concerned with the change in the mechanical properties of polymers with temperature and the effects of this change on friction and wear. At a certain temperature, termed the glass transition temperature T_g, a high density amorphous polymer changes from a rigid solid or glass to a rubbery form. At this point, the Young's Modulus, shear modulus and yield strength can decrease by a factor of about a thousand [Nielsen, 1962].

This change in the shear modulus of polymethylmethacrylate (PMMA) is shown in Figure A-1. There is a distinct drop in the shear modulus at approximately 120^0C which is the glass transition temperature for PMMA. There is also an increase in the mechanical damping of the polymer at 80^0C due to the transition of the polymer to a more viscous state than that at room temperature. The curves displayed in Figure A-2 illustrate the stress-strain curves of PMMA for six typical temperatures. As the temperature increases, the general features of the curve correspond to stress-strain behavior in a rubbery material.
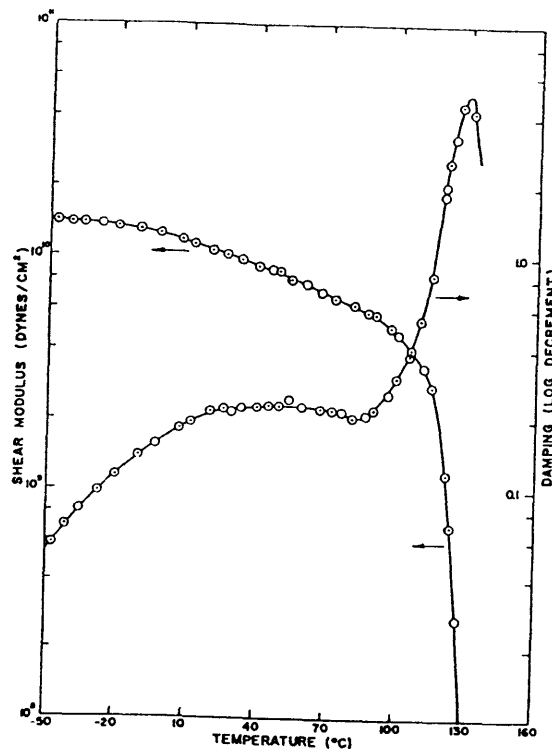
Figure A-1: Dynamic mechanical properties of polymethylmethacrylate [Nielsen, 1960].

Typical polymers consist of molecules made up of long chains of CH_2 groups. The changes in the mechanical properties of a polymer with temperature is attributed to the molecular motion of these long groups. Below the glass transition temperature T_g, the molecules are frozen and have limited freedom of motion. However, when

106
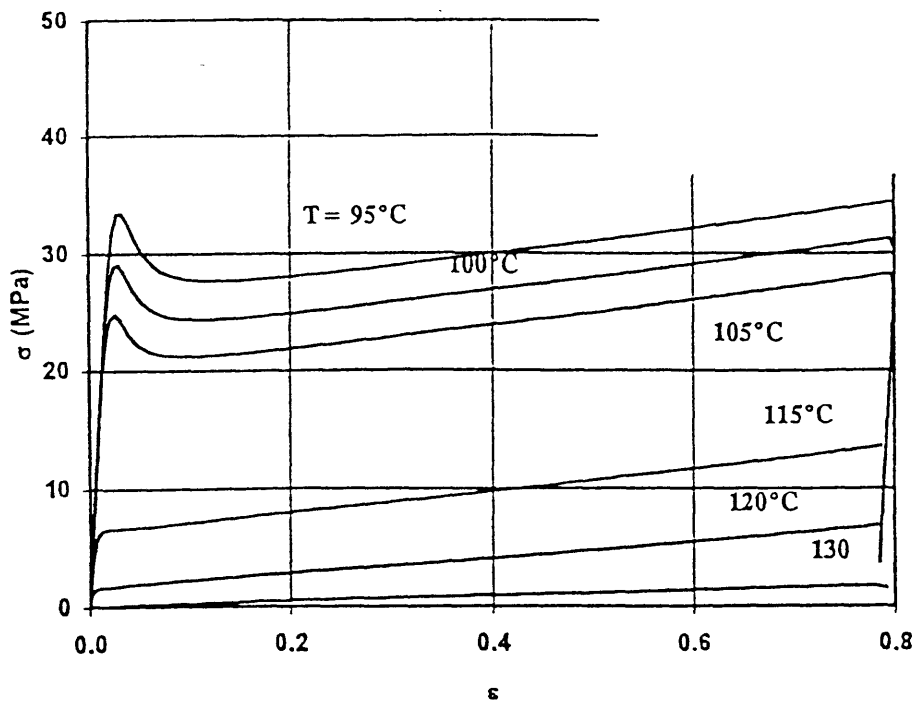
Figure A-2: Typical stress-strain curves for PMMA at various temperatures ranging from 368 K (95⁰C) to 403 K (130⁰C) [Gauthier, et al., 1997].

the glass transition temperature is attained, the polymer expands and there is now enough free volume for molecular motion to begin. This change in the mobility of the molecules increases its viscosity and causes a change in the mechanical properties of the polymer.

The friction and wear behavior of solids is strongly influenced by their mechanical properties. The three basic friction mechanism are asperity deformation, plowing and adhesion [Suh, 1986]. In the asperity deformation model, friction force is the resistance to motion that arises when asperities of the sliding bodies come into contact and deform. Another mechanism responsible for friction is plowing. Plowing occurs when hard abrasive particles or asperities dig into the softer surface. Friction due to adhesion is the resistance to motion that occurs when the two bodies which are in relative motion adhere to each other. The exact nature of this adhesive force is still unknown but it is proposed that surface energy interactions may be responsible.

The removal of material in the form of small particles of the order of micrometers from a sliding surface is the process of wear. In most cases, where there is friction, there is wear and therefore wear generating mechanisms are similar to those of friction generation. The primary modes of wear are adhesion, plowing and delamination.

In the adhesive theory of wear, it is proposed that wear particles are created when the adhesive junction is torn apart as the surfaces continue to slide over each other.

107

Shear or fractures takes place and wear particles are created. Wear is also thought to occur when plowing of a softer surface by hard particles or asperity occurs. The plowing action by itself creates wear particles. In the delamination theory of wear, repeated loading of a surface results in subsurface plastic deformation. This promotes crack nucleation and propagation. As opposed to wear particles created by other wear generating mechanisms, delamination wear usually results in the formation of thin wear sheets. Despite these different classifications of wear generating mechanisms, in most cases, any wear process is a combination of all the different modes of wear with one predominant mechanism of wear.

In polymer bearing applications, friction force is primarily due to plowing of the polymer surfaces. This is because the hardness of metals is an order of magnitude greater than that of polymers, and when metal particles or asperities come in contact with polymers there is severe plowing. It is proposed that the wear mechanism for polymers is delamination wear [Suh, 1986]. This being the case, it is hypothesized that there will be an increase in both friction and wear beyond the glass transition temperature. The mechanical properties of the polymer changes beyond the glass transition temperature and the polymer becomes rubbery and soft. It is postulated that plowing and subsurface plastic deformation will be promoted when this happens. A previous study proposes that wear rate of thermoplastics increase drastically when the contacting surface of the material reaches a critical temperature related to its melting or softening temperature [Kennedy, and, Tian, 1994]. The materials investigated in that study were PMMA and Ultra High Molecular Weight Polyethylene (UHMWP). The temperatures that were recorded for the drastic increase in wear rate were close to the melting point of the polymers. The increase in wear is attributed to the increase in the wear generating mechanism which is proposed to be plowing. The changes in friction and wear as the glass transition temperature is exceeded received little attention in that study, however.

In this study, the variations in the coefficient of friction and wear with increase in temperature up to and beyond the glass transition temperature are determined. The polymers used were PMMA, polytetrafluoroethylene (Teflon), polypropylene and a glass-reinforced polyester. This study determines the changes in friction and wear with temperature and also identifies the relationship between friction generating and wear generating mechanisms in polymers.

A.2 Experimental

The objective of the experimental study is to measure the friction and wear coefficient of the four polymers with variation in temperature.

A.2.1 Apparatus and Procedure

A pin-on-flat friction testing apparatus was used for the tests. Figure A-3 schematically illustrates the experimental apparatus.
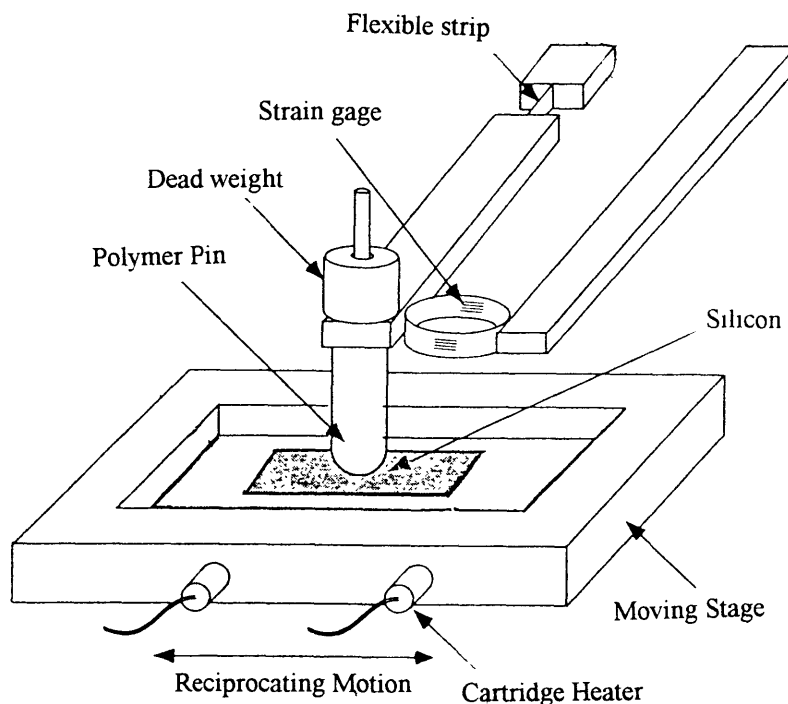
Figure A-3: Schematic of friction testing apparatus.

A stationary polymer pin was in contact with an oscillating flat specimen. The pins were 6.35 mm in diameter and were machined to have spherical tips of radius 3.175 mm. The spherical tips of the polymer pins were polished and examined microscopically before being mounted in the friction testing apparatus to ensure that the pins were free from irregularities and have a smooth surface finish. The pins were then carefully weighed on a sensitive microbalance with a resolution of 0.00001 g. The substrate was silicon. Silicon was used as it provides a smooth, flat, hard surface.

The substrate was clamped to a sliding stage and cartridge heaters were inserted into the stage for high temperature friction testing. A thermocouple and temperature controller measured and controlled the temperature of the silicon flat. The slider stage was heated to the required temperature and the polymer pin was then contacted with the silicon surface. The pin was allowed to equilibrate with the substrate. The temperature equilibrium time was estimated to be about 10 minutes. Each test was run for 10 minutes. The friction force, F, was measured by a sensitive strain gage ring and was displayed on a chart recorder. Two values of friction coefficient were measured. The initial friction coefficient μ_i, was measured after one complete oscillation and the second value μ_k, was measured at the end of each test

Table A.1: List of experimental conditions

Experimental Conditions	
Sliding Speed	1.17 cm/s
Sliding displacement	4.7 cm
Diameter of Pin	6.35 mm
Normal Load	2 N (200 g)
Diameter of Pin	6.135 mm
Radius of Curvature	3.175 mm

run. On completion of a friction experiment, the polymer pin was re-weighed using the microbabalnce to determine the amount of mass loss in the pin. The values for the friction coefficient $\mu = \mu_i$ and the wear coefficient, k, were then plotted against temperature. The experimental conditions are listed in Table A.1.

A.2.2 Materials

The polymers used in this experimentwere PMMA, Teflon, polypropylene and thermalcure polyester. The thermalcure specimen is unique in that it consists of unidirectionally oriented polyester fibers with glass reinforcements. The fibers were oriented perpendicular to the sliding direction.

Table A.2 provides the molecular structure of the polymers and Table A.3 lists the physical properties of the materials used. Table A.4 lists the properties of silicon.

A.2.3 Calculation of friction coefficient and wear coefficient

In these experiments it is assumed that the friction force, F, is proportional to the normal load N. Hence the friction coefficient μ is given by,

$$\mu = \frac{F}{N}.$$ (A.1)

Figure A-4 is a time trace of the friction force measured by the strain gage ring for a PMMA pin sliding against a silicon substrate at 40^0C.

The wear rate, W, is given by,

$$W = \frac{V}{S},$$ (A.2)

110

Table A.2: Molecular structure of the polymers

Material	Molecular Structure
Polypropylene	$\begin{array}{cc} H & CH_3 \\ | & | \\ -C- & -C- \\ | & | \\ H & H \end{array}$
Polytetrafluoroethylene (TEFLON)	$\begin{array}{cc} F & F \\ | & | \\ -C- & -C- \\ | & | \\ F & F \end{array}$
Polymethylmethacrylate (PMMA)	$-CH_2-\overset{\displaystyle CH_3}{\underset{\displaystyle \overset{|}{C}-O-CH_3}{\overset{|}{C}}}$
Polyester	$-O-\overset{O}{\overset{\|}{C}}-\bigcirc-\overset{O}{\overset{\|}{C}}-O-CH_2-CH_2-$

Table A.3: Physical properties of polymers

Material	T_g (^{0}C)	T_m (^{0}C)	Young's Modulus E (GPa)	Tensile Yield Strength σ_Y (MPa)	Hardness H (MPa)
Polypropylene	-10, -18	176	1.55	35.0	105.0
Polytetrafluoroethylene Teflon	126	327	0.53	28.2	84.72
Polymethylmethacrylate PMMA	105, 120	> 200	2.94	68.0	203.97
Polyester composite	-	-	40.80	680	96.30

111

Table A.4: Physical properties of silicon

Silicon	
Melting Point (^{0} C)	1410
Young's Modulus, E (GPa)	156.7
Poisson's Ratio, ν	0.28
Hardness (MPa)	9800

where V, is the wear volume and S is the distance slid. Now,

$$S = ut, \tag{A.3}$$

where u, is the sliding speed and t, the time taken for one complete run. In this case, t is always 10 minutes. Also,

$$V = \frac{m}{\rho}, \tag{A.4}$$

where m, is the mass loss in a polymer pin and ρ, the density of the polymeric material.

Substituting (A.3) and (A.4) into (A.1) gives,

$$W = \frac{m}{\rho ut}. \tag{A.5}$$

The wear coefficient k, is a dimensionless quantity given by,

$$k = \frac{WH}{N}. \tag{A.6}$$

Using (A.5), this becomes

$$k = \frac{mH}{N\rho ut}. \tag{A.7}$$
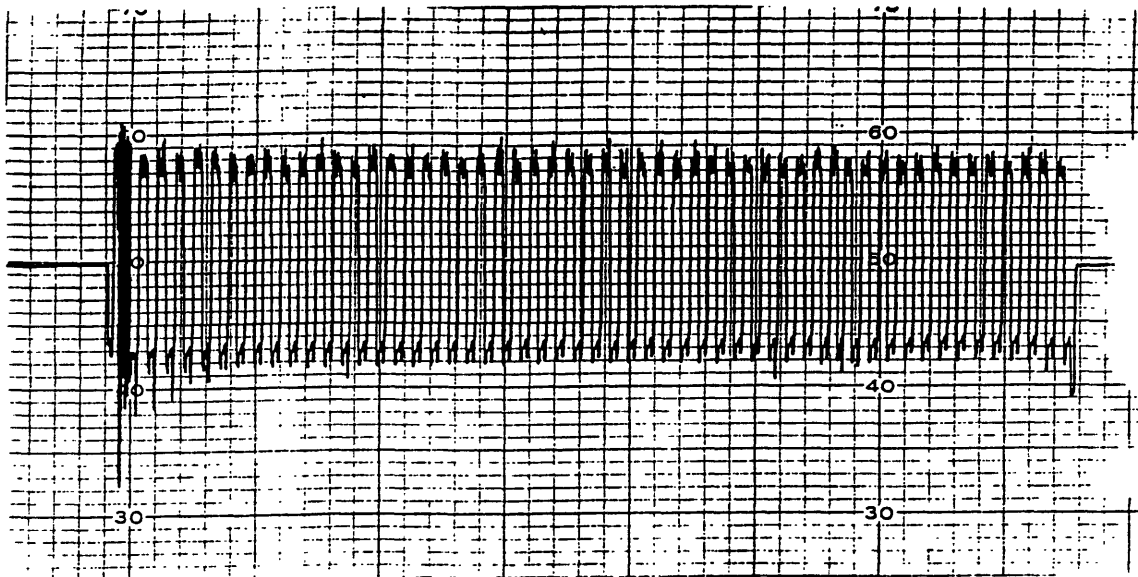
Figure A-4: Actual time trace from chart recorder for PMMA sliding on silicon at 40°C. $\mu_i = 0.7$.

A.3 Results

The experimental results indicate a definite trend in the friction and wear behavior of some of the polymers used in this project. Outlined below is an analysis of the results obtained for each polymer tested. In all plots of friction coefficient with temperature, the value used is the initial friction coefficient obtained after one complete oscillation of the slider. The steady state friction coefficient, however, was usually higher than the initial friction coefficient due to the formation of wear particles. Table A.5 lists the initial friction coefficients, μ_i, for all the materials tested.

A.3.1 Polymethylmethacrylate (PMMA)

The results for PMMA are shown in Figures A-5 and A-6. It can be seen that there is a considerable increase in friction coefficient when the temperature exceeds 100°C. Below this temperature, the friction coefficient lies in the range 0.70 to 0.90. At 100°C, the friction coefficient is 1.0 and this shoots up to 2.2 at 120°C. Above this temperature, the friction coefficient remains at a steady value.

The results suggest that in the case of a PMMA pin sliding on silicon, there is a sudden jump in friction as the glass transition temperature is exceeded. The glass transition temperature, T_g, for PMMA is approximately in the range between 105°C

113

Figure A-5: Variation in friction coefficient with temperature. PMMA sliding on silicon. Normal load: 2 N (200 g).

Figure A-6: Variation in wear coefficient with temperature. PMMA sliding on silicon. Normal load: 2 N (200 g).

Table A.5: Initial friction coefficient between polymers and silicon. Normal load = 2.0 N.
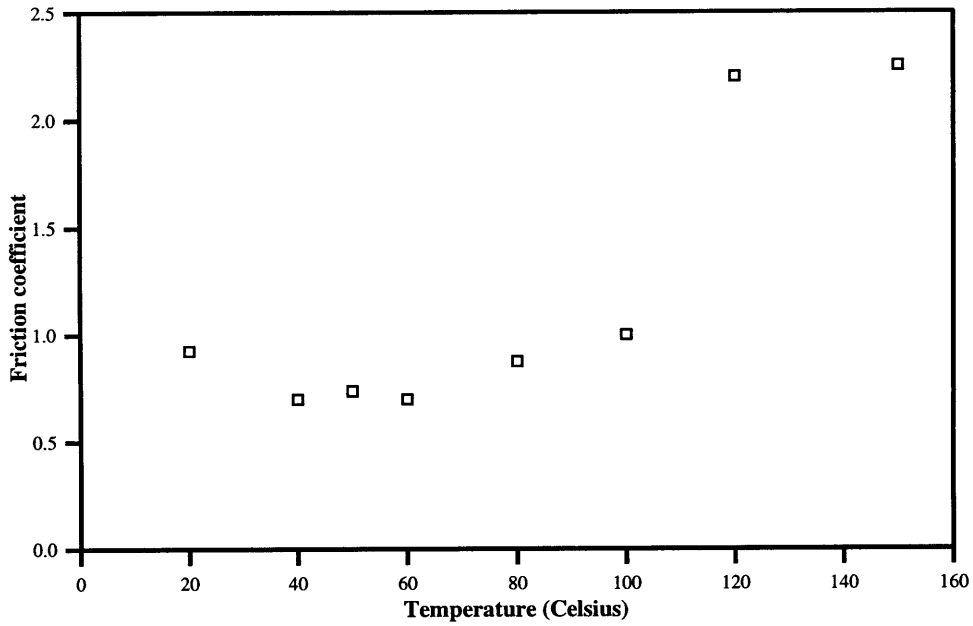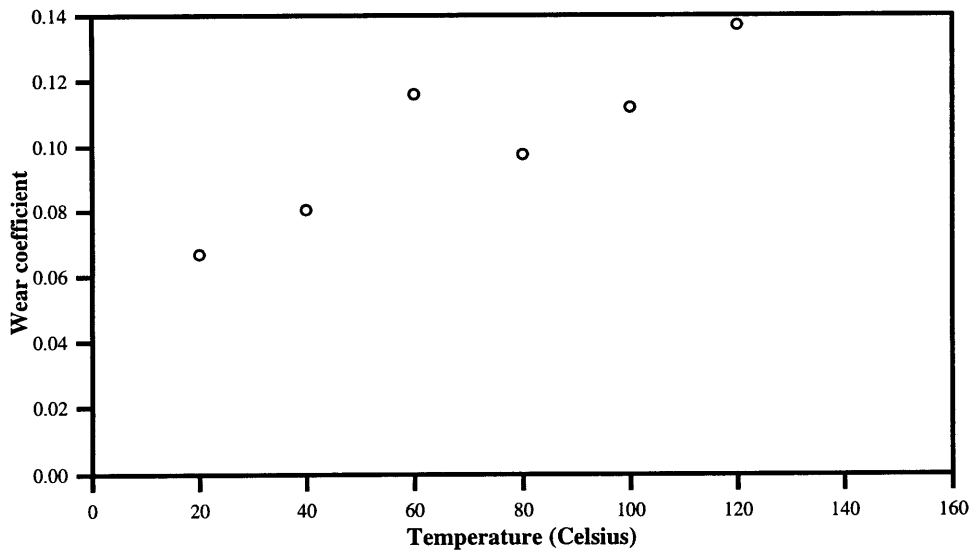
Material	Coefficient of Friction μ
Polypropylene	0.16
Polytetrafluoroethylene (Teflon)	0.08
Polymethylmethacrylate (PMMA)	0.9
Polyester Composite	0.23

and $120^{0}C$. However, the results depicted in Figure A-6 suggests that there is no corresponding jump in the wear coefficient at $100^{0}C$ to that at $120^{0}C$. The results are summarized in Table A.6.

However, there is only a steady rise in k with increase in temperature. These observations suggest that the there is no dependency between friction and wear for PMMA sliding on silicon and also that the mechanical properties which affect frictional behavior are not the same as those that affect the wear behavior of this polymer.

A.3.2 Polytetrafluoroethylene (Teflon)

A similar trend with the values for μ with change in temperature is exhibited by a Teflon pin sliding on silicon. The friction data for Teflon is rather erratic and fluctuates in between 0.08 and 0.09 for temperatures below $80^{0}C$. However, the value for m obtained at $120^{0}C$ is almost twice as great as that obtained for μ at $100^{0}C$. Figure A-7 indicates the variation of μ with temperature.

The T_g for Teflon is $126^{0}C$, and the increase in μ corresponds to this temperature. The results also indicate a drop in the value of μ at $140^{0}C$. A possible explanation for this is that at a temperature of $140^{0}C$, the viscous nature of the polymer becomes dominant and a thin film of Teflon coating forms on the substrate. This thin film acts like a lubricant and decreases friction at the interface. Similar behavior was not exhibited by PMMA as PMMA is almost twice as hard as Teflon and a higher
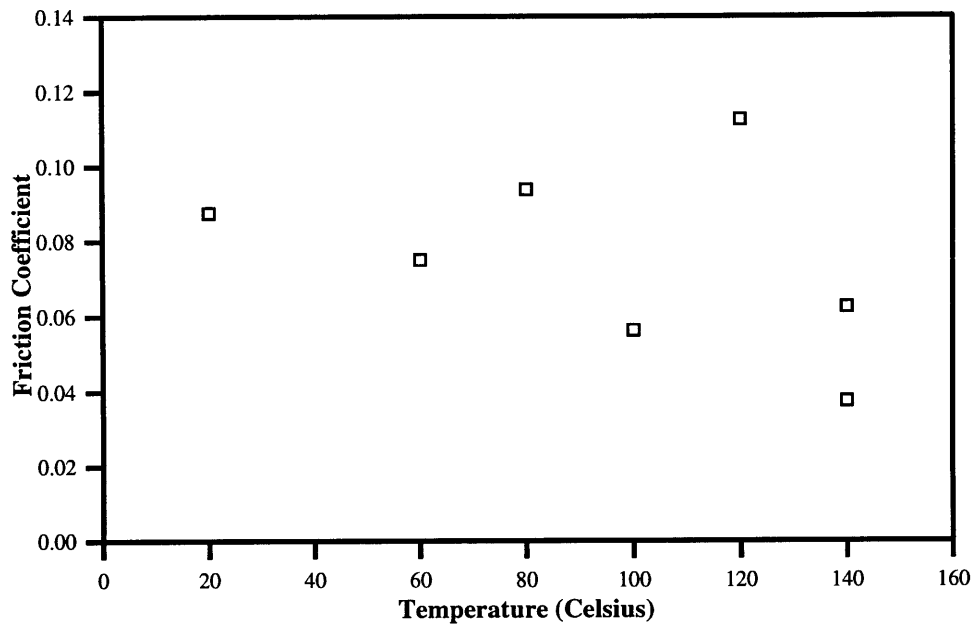
Figure A-7: Variation in friction coefficient with temperature. Teflon sliding on silicon. Normal load: 2 N (200 g).
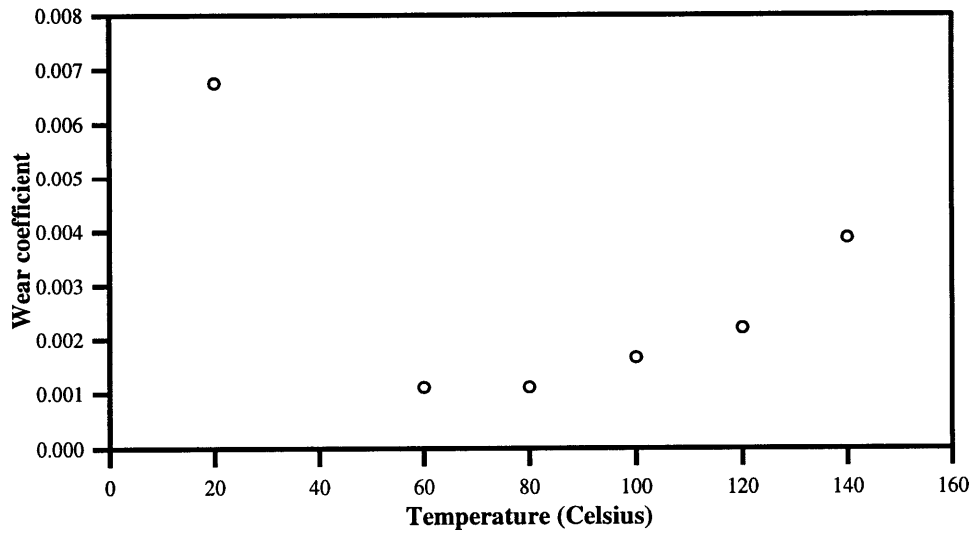

Figure A-8: Variation in wear coefficient with temperature. Teflon sliding on silicon. Normal load: 2 N (200 g).

Table A.6: Wear coefficient below and above T_g for PMMA.

PMMA	
Temperature (^{0}C)	Wear Coefficient k
80	0.0976
100	0.112
120	0.137

temperature would have to be attained before the viscous nature of PMMA becomes dominant.

The wear behavior of Teflon with increase in temperature is depicted in Figure A-8. The results show no indication of a rise in k with temperature corresponding to the jump in μ at about 120^{0}C. An interesting feature is the steady decrease in k as the temperature is increased from 20^{0}C to 60^{0}C. From 60^{0}C to 140^{0}C, there is a steady increase in k. It is proposed that the initial decrease in wear with increase in temperature occurs due to the increase in the viscous nature of the polymer with increase in temperature. A thin layer of lubricant forms and wear rate decreases. However, beyond 60^{0}C, the wear rate increase with increase in temperature as the thin layer starts to delaminate. The mechanical properties of the thin film change beyond the glass transition temperature and the coating becomes more susceptible to delamination wear.

A.3.3 Polypropylene

The results for polypropylene are depicted in Figures A-9 and A-10. The glass transition temperature for polypropylene is in the range between -18^0C and -10^0C. Results indicate that there is no change in μ with temperature in the range between 20^{0}C to 120^{0}C. The wear coefficient, k, is also observed to be constant within this range. There is a rise in both μ and k at 120^{0}C and 150^{0}C and this is because the polymer begins to melt between these temperatures. The polymer pin is observed to stick to the substrate and sliding was impeded. This brought about the rise in μ and k at these temperatures.
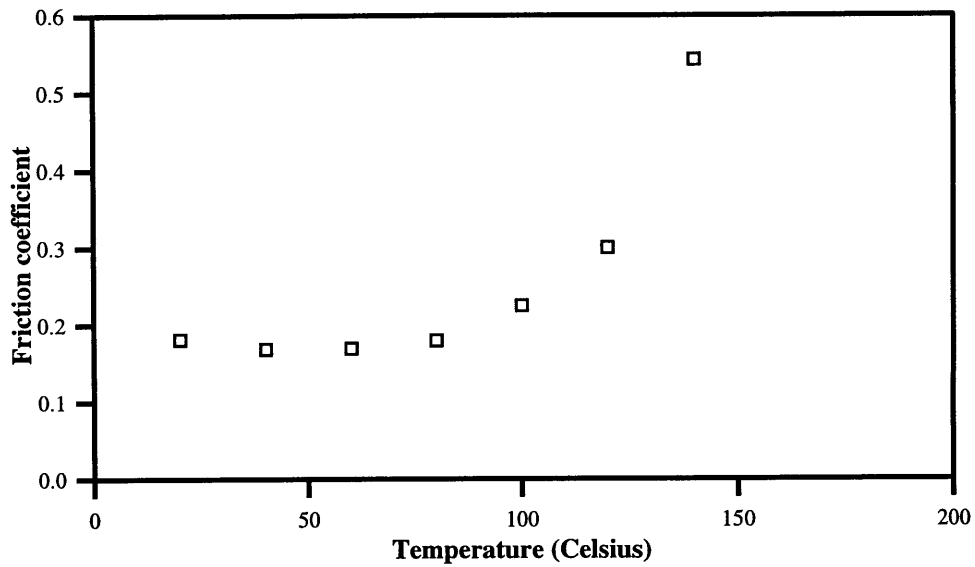
Figure A-9: Variation in friction coefficient with temperature. Polypropylene sliding on silicon. Normal load: 2 N (200 g).
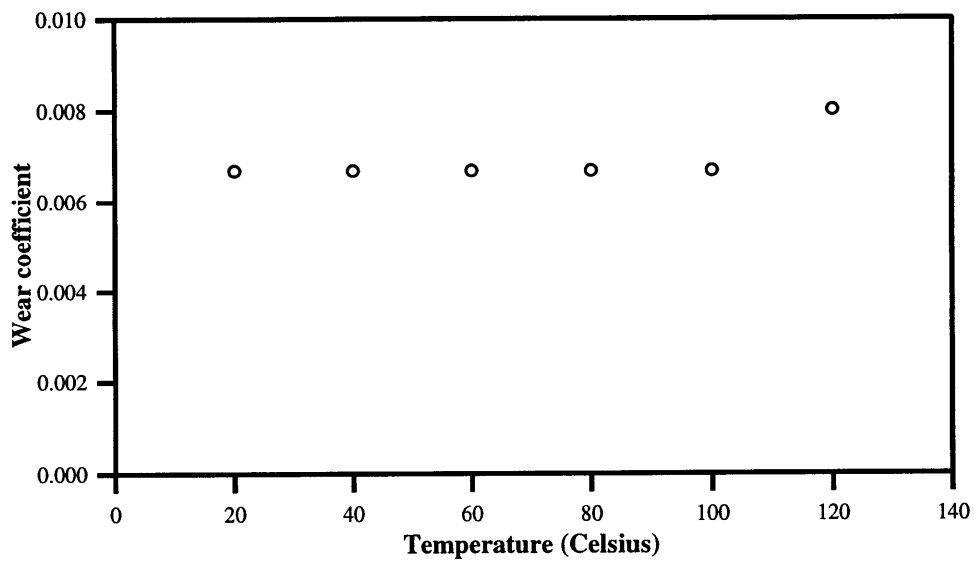

Figure A-10: Variation in wear coefficient with temperature. Polypropylene sliding on silicon. Normal load: 2 N (200 g).

118

A.3.4 Polyester Composite

The thermalcure polyester material consists of unidirectionally oriented polyester fibers reinforced with unidirectionally oriented glass fibers. There is no distinct value for the glass transition temperature. However, information obtained from the manufacturer (Strongwell, Virginia) specifies that the operating temperature for this material below 65^0C. At and above, 65^0C, the bonding between the polyester and glass starts to weaken and the material deforms. Figure A-11 indicate that the friction measurements are erratic although there is clearly an increase in wear with increase in temperature as indicated in Figure A-12. The wear coefficient at 60^0C is 0.254 and that at 80^0C is almost twice as great (see Table A.7). This suggests that the wear behavior is effected by the weakening of the bonding between the fibers at temperatures greater than 65^0C. However, friction does not seem to be affected by the weakening of the bonds at 65^0C as no definite rise in μ is observed from the experimental results.

Table A.7: Wear coefficient below and above 65^0C for polyester composite.

Polyester Composite	
Temperature (^{0}C)	Wear Coefficient k
60	0.254
80	0.419

A.4 Discussion

The first point that is noted from the results is that there is an increase in friction coefficient when the glass transition temperature, T_g, is exceeded. This is clearly observed with PMMA and Teflon pins slid against silicon in the temperature range 20^0C yo 140^0C. The glass transition temperature of both PMMA and Teflon are within this range. This is not the case for polypropylene which has a glass transition temperature well below room temperature. Similarly, there is no increase in friction with temperature for the polyester composite material. Figure A-13 depicts the fraction rise in μ for PMMA with increase in temperature. The jump at the transition temperature is clearly shown. The experimental results also suggest that there is an increase in wear
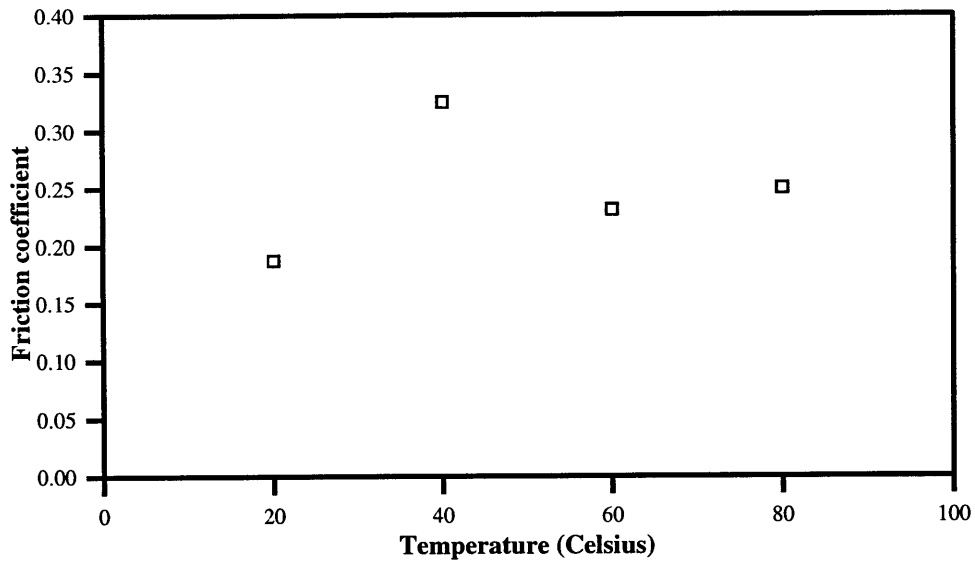
119

Figure A-11: Variation in friction coefficient with temperature. Polyester composite sliding on silicon. Normal load: 2 N (200 g).
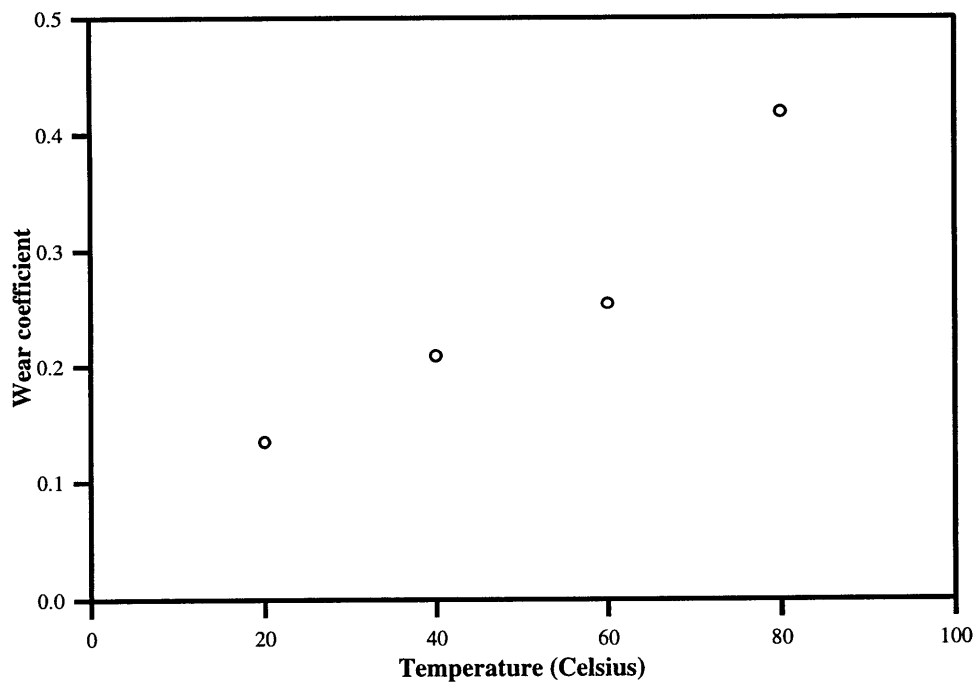

Figure A-12: Variation in wear coefficient with temperature. Polyester composite sliding on silicon. Normal load: 2 N (200 g).

with increase in temperature for all the polymers tested as indicated in Figure A-14. There is however no jump in the value for k at the glass transition temperature for PMMA and Teflon.

The friction and wear characteristics exhibited in this set of experiments can be explained by considering the friction and wear mechanisms for these materials. The experimental results seem to suggest that the dominant friction mechanism for these polymers sliding on silicon is adhesion. Both plowing and asperity deformation do contribute to the friction force generated at the interface but adhesion is the primary form for energy dissipation in the system. This assumption is made for the following reasons. First, the silicon substrate used in these experiments is highly polished and the root mean square value (RMS) for the surface roughness is approximately 1.15 nm [Silvestro, 1996]. The polymer pins were also polished and examined under the microscope for surface defects and irregularities. This being the case, it is assumed that asperity deformation plays a small role in friction generation as two polished surfaces are coming into contact and there are few asperities on both surfaces.

The hardness of the silicon substrate is an order of magnitude higher than those of the polymers tested. Thus, plowing would occur when the surface asperities on the silicon surface penetrate the polymer pin. As the surface of the silicon substrate is smooth, plowing does not occur readily in this system, at least in the early stages of sliding.

In the adhesion theory for friction generation, using a simple model, the tangential force, F required to shear an adhesive junction is given by [Rabinowicz, 1995],

$$F = \tau A_r, \qquad\qquad (A.8)$$

where τ is the shear strength of the polymer and A_r is the real area of contact of the polymer pin on the substrate.

At high temperatures, the polymer softens, and begins to stick to the silicon surface. The force required to shear the interface increases due to this stickiness. This increase in τ, impedes sliding and results in an increase in friction.

In some cases, the polymer softens to the extent that the viscous behavior of the polymer becomes dominant and this is clearly the case with Teflon where beyond 120^0C there is a decrease in the value of μ because a thin film of Teflon develops on the substrate.

However, it is important to note that although adhesion is the primary friction generating mechanism, wear behavior is determined by delamination. An amorphous polymer can be modeled as a random tangle of molecules as depicted in Figure A-15. Thus, when an amorphous polymer is stretched, the molecules may be preferentially aligned in the stretch direction [Ward, 1993]. At temperatures greater than the glass transition temperature, the molecular chains become more mobile and it becomes easier for the molecular chains to align themselves in the sliding direction. The shear strength of the material decreases and subsurface deformation occurs. This is
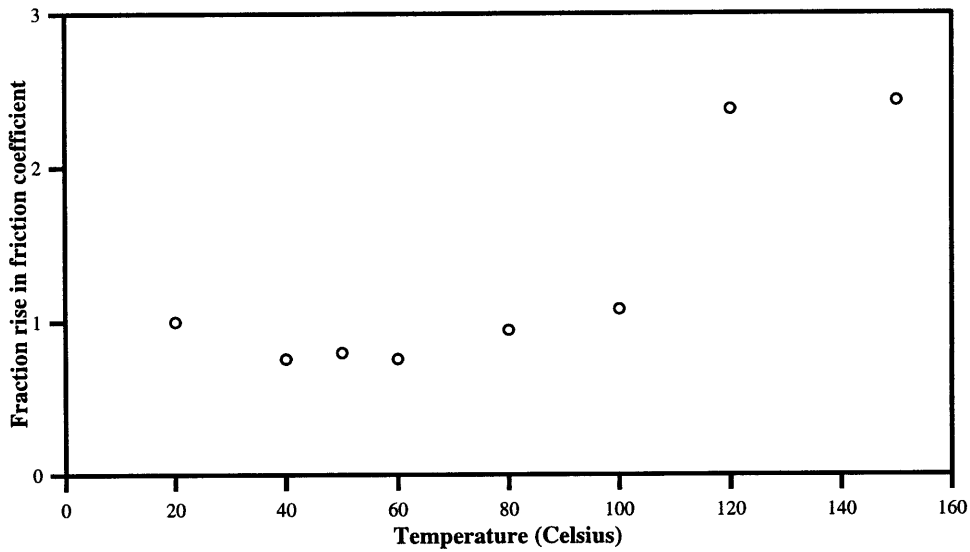
121

Figure A-13: Fraction rise in friction coefficient with temperature for PMMA. Normal load: 2 N (200 g)
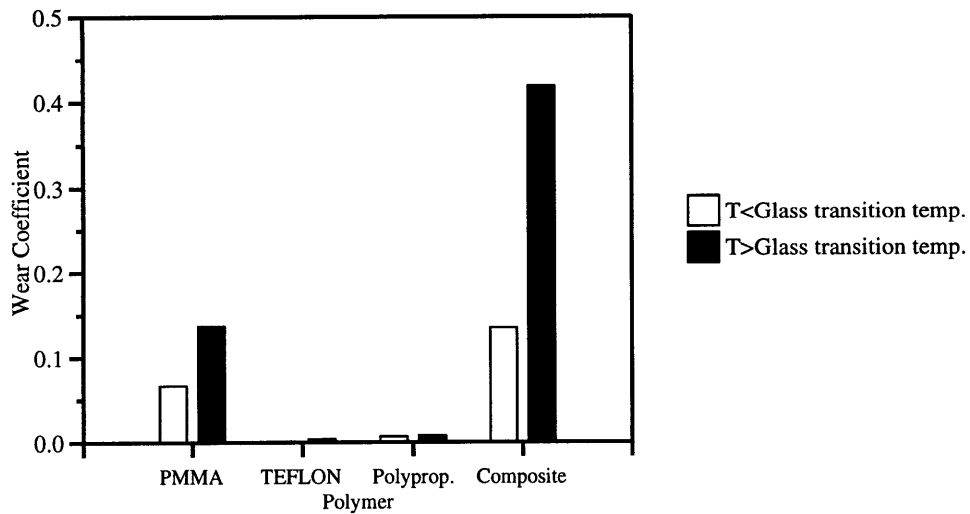

Figure A-14: Bar graph indicating the variation in wear coefficient with temperature for PMMA, Teflon, polypropylene and polyester composite. Normal load: 2 N (200 g)

followed by crack nucleation and propagation. As explained earlier this decrease in the shear strength of the polymer as the glass transition temperature is exceeded is more gradual and this is responsible for the more gradual and steady rise in k for PMMA and Teflon with temperature.
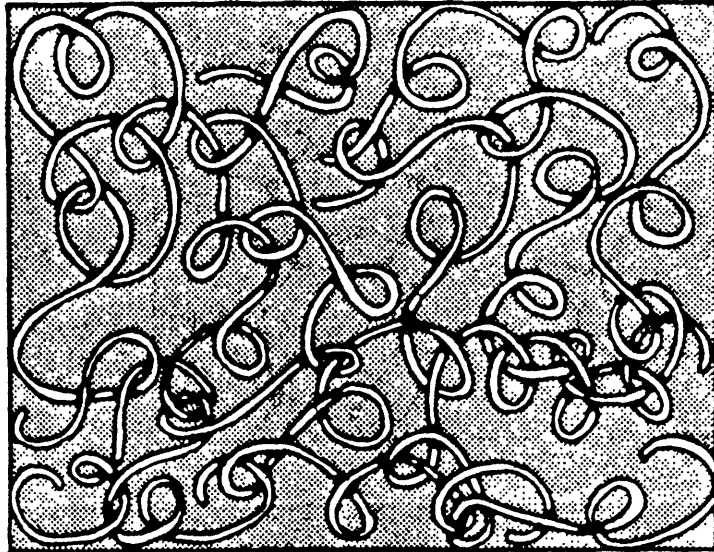
Figure A-15: Schematic diagram of amorphous polymer chains. [Ward, 1993]

In polypropylene, there is no change in the molecular mobility with increase in temperature as the glass transition temperature is below room temperature. The increase in wear at 150^0C is because polypropylene begins to melt and this causes an increase in the mass loss of polypropylene.

The wear rate in oriented polymers where the fibers are unidirectionally aligned to be perpendicular to the sliding direction have been shown to be far less than polymer which have fibers oriented randomly [Suh, 1986]. The rationale behind this is that in unidirectionally oriented polymers, crack propagation is decreased by preventing concentration of shear strain at the crack tip. However as the temperature increases, a certain point is reached when the material starts to deform as the bonding between the fibers and the glass reinforcements began to weaken. Subsurface deformation occurs leading to crack nucleation and propagation. Hence, there is an increase in wear rate as the temperature is increased. Another factor promoting wear are the glass fibers themselves. Glass wear particles created due to crack propagation worsen the wear rate by digging into the polyester and plowing its surface.

A.5 Conclusions

Outlined below is a summary of the conclusions drawn from this study.

1. There is a marked increase in friction coefficient when the glass transition temperature of amorphous polymers is exceeded.

2. This is accompanied by a more gradual and steady increase in wear rate with temperature. There is therefore very little dependency between friction and wear primarily because the friction generating mechanism is different from the wear generating mechanism.

3. The friction generating mechanism is adhesion, and as the glass transition temperature is exceeded, there is a decrease in certain mechanical properties namely the hardness of the polymer. Adhesion between the polymer pin and substrate is promoted and this contributes to an increase in the friction coefficient.

4. The wear determining mechanism is delamination wear. When the glass transition temperature is reached, there is an increase in wear rate. This is because it becomes easier for the molecules in the polymer to orient themselves in the sliding direction as discussed earlier. The shear strength of the polymer decreases and crack propagation is promoted.

A.6 References

Alexander, W.,Park, J.S., and Shackelford, J.F., 1996, **CRC Materials Science and Engineering Handbook**, CRC Press, Boca Raton, pp. 411–417.

Askadskii, A., 1996, **Physical Properties of Polymers: Prediction and Control**, Gordon and Breach Science Publishers, Amsterdam, p. 58.

Gauthier, C., Laurent, D., Ladouce, L., Quinson, R., Perez, J., 1997, "Nonlinear Mechanical response of Amorphous Polymers Below and through Glass Transition Temperature," *Journal of Applied Polymer Science*, Vol. 65, pp. 2517-2518.

Hunt, M.W., 1992, **Materials Engineering Applications, Materials Selector 1993**, Penton Publications, Cleveland, pp. 110–127.

Kennedy, F.E., Tian, X., 1994, "The Effect of Interfacial Temperature on Friction and Wear of Thermoplastics in the Thermal Control Regime," *Tribology Series*, Vol. 24, pp. 235-244.

Ma, T., 1987, "Stresses in Silicon Dioxide on Silicon Structures," **Properties of Silicon**, Institute of Electrical Engineers, London, INSPEC, London, pp. 650–661.

Nielsen, L.E., 1962, **Mechanical Properties of Polymers**, Reinhold Publishing, New York, pp. 12–21.

Silvestro, M., 1996, "Analysis of Boundary Lubricant Films Using Raman Spectroscopy," Masters Thesis, Department of Mechanical Engineering, Massachusetts Institute of Technology, p. 52.

Suh, N.P., 1986, **Tribophysics**, Prentice-Hall, Eaglewood Cliffs, NJ.

Ward, I.M., Hadley, D.W., 1993, **An Introduction to the Mechanical Properties of Solid Polymers**, John Wiley and Sons, Inc., Chichester, p. 12.

Yim, S., 1997, "Molecular Dynamics Simulation of Boundary Lubrication," S.M. Thesis, Massachusetts Institute of Technology, p. 13.

Bibliography

Alexander, W., Park, J.S., and Shackelford, J.F., 1996, **CRC Materials Science and Engineering Handbook**, CRC Press, Boca Raton, pp. 411–417.

American Society for Metals, 1987, **Engineered Materials Handbook, Ceramics and Glass**, American Society for Metals, Ohio, Vol. 4, pp. 747–892.

Askadskii, A., 1996, **Physical Properties of Polymers: Prediction and Control**, Gordon and Breach Science Publishers, Amsterdam, p. 58.

Bhushan, B., Israelachvili, J.N., and Landman, U., 1995, "Friction, Wear and Lubrication at the Atomic Scale," *Nature*, Vol. 374, pp. 607–616.

Bowden, F.P., and Tabor, D., 1950, **The Friction and Lubrication of Solids**, Oxford Clarendon Press, London, pp. 312–314.

Bowling, F.P., and Davis, C.J., 1994, "Managing Contamination During Advanced Wafer Processing," *Solid State Technology*, Vol. 37, pp. 45–50.

Busnaina, A., Taylor, J., and Kashkoush, I., 1993, "Measurement of the Adhesion and Removal Forces of Submicrometer Particles on Silicon Substrates," *Journal of Adhesion Science and Technology*, Vol. 7, pp. 441–445.

Davis, G.D., 1993, "Contamination of Surfaces: Origin, Detection and Effect on Adhesion," *Surface and Interface Analysis*, Vol. 20, pp. 368–372.

Demejo, L.P., Rimai, D.S., and R.C., Bowen, 1988, "Direct Observation of Deformations Resulting from Particle-Substrate Adhesion," *Journal of Adhesion*, Vol. 2, pp. 331–337.

Derjaguin, B.V., Aleinikov, I.N., and Toporov, Y.P., 1994, "On the Role of Electrostatic Forces in the Adhesion of Polymer Particles to Solid Surfaces," *Progress in Surface Science*, Vol. 45, pp. 119–125.

Derjaguin, B.V., Muller, V.M., and Toporov, Y.P., 1975, "Effect of Contact Defor-

mations on the Adhesion of Particles," *Journal of Colloid and Interface Science*, Vol. 53, pp. 314–326.

Derksen, J., 1997, "A New Coating Method for Semiconductor Lithography: Fluid Layer Overlap in Extrusion-Spin Coating," S.M. Thesis, Massachusetts Institute of Technology, pp. 16–24.

Douglas Frink, L.J., and Van Swol, F., 1997, "A Molecular Theory for Surface Forces Adhesion Measurements," *Journal of Chemical Physics*, Vol. 106, pp. 3782–3791.

Goodman, L.E., 1962, "Contact Stress Analysis of Normally Loaded Rough Spheres," *Transactions of the ASME, Series E, Journal of Applied Mechanics*, Vol. 34, pp. 515–522.

Greenwood, J.A., and Williamson, J.B.P., 1966, "Contact of Nominally Flat Surfaces," *Proceedings of the Royal Society of London*, Vol. A 295, pp. 300–319.

Greenwood, J.A., and Tripp, J.H., 1967, "The Elastic Contact of Rough Spheres," *Transactions of the ASME, Series E, Journal of Applied Mechanics*, Vol. 35, No. 153, pp. 153–159.

Hardy, S.C., 1986, "Surface Tension of Liquid Silicon," **Properties of Silicon**, Institution of Electrical Engineers, INSPEC, London, pp. 58.

Hertz, H., 1896, **Miscellaneous Papers**, Macmillan, London, pp. 146–184.

Hertz, H., 1956, **The Principles of Mechanics Presented in a New Form**, Dover Publications, New York.

Hunt, M.W., 1992, **Materials Engineering Applications, Materials Selector 1993**, Penton Publications, Cleveland, Ohio, pp. 110–127.

Israelachvili, J.N., Chen, Y.L., and Yoshizawa, H., 1994, "Relationship Between Adhesion and Friction Forces," *Journal of Adhesion Science and Technology*, Vol. 8, pp. 1231–1248.

Israelachvili, J.N., and McGuiggan, P.M., 1990, "Adhesion and Short-Range Forces Between Surfaces. Part I: New Apparatus for Surface Force Measurements," *Journal of Materials Research*, Vol. 5, pp. 2223–2231.

Johnson, K.L., 1976, "Adhesion at the Contact of Solids," *Proceedings of the Congress of Theoretical and Applied Mechanics*, W.T., Koiter, ed., North-Holland Publishing Company, Amsterdam, pp. 133–143.

Johnson, K.L., 1985, **Contact Mechanics**, Cambridge University Press, London,

pp. 84–104, pp. 119–125, pp. 397–416.

Johnson, K.L., 1997, "Adhesion and Friction Between a Smooth Elastic Spherical Asperity and a Plane Surface," *Proceedings of the Royal Society of London*, Vol. A 453, pp. 163–179.

Johnson, K.L., Kendall, K., and A.D., Roberts, 1971, "Surface Energy and the Contact of Elastic Solids," *Proceedings of the Royal Society of London*, Vol. A 324, pp. 301–313.

Kendall, K., 1974, "Kinetics of Contact Between Smooth Solids," *Journal of Adhesion*, Vol. 7, pp. 55–72.

Ketkar, A.B., and Keller, D.V., Jr., 1975, "Adhesion of Micron-Sized Limestone Particles to a Massive Coal Substrate," *Journal of Adhesion*, Vol. 7, pp. 235–250.

Kroninger, F., Streckfuss, N., Frey, L., Falter, T., and Ryzlewicz, C., 1993, "Application of Advanced Analysis for Qualification of Wafer Handling Systems and Chucks," *Applied Surface Science*, Vol. 63, pp. 93–98.

Krupp, H., 1967, "Particle Adhesion Theory and Experiment," *Advances in Colloid and Interface Science*, Vol. 1, pp. 111–239.

Lehmann, V., Gösele, U., and Mitani, K., 1990, "Contamination Protection of Semiconductor Surfaces by Wafer Bonding," *Solid State Technology*, Vol. 33, pp. 91–92.

Ma, T., 1987, "Stresses in Silicon Dioxide on Silicon Structures," **Properties of Silicon**, Institute of Electrical Engineers, London, INSPEC, London, pp. 650–661.

Maboudian, R., and R.T., Howe, 1997, "Critical Review: Adhesion in Surface Micromechanical Structures," *Journal of Vacuum Science and Technology. B, Microelectronics Processing and Phenomena*, Vol. 15, pp. 1–20.

Mark, J.E., 1996, **Physical Properties of Polymers Handbook**, American Institute of Physics, New York, pp. 313–334.

Marks, M.R., Kintrup, L., and Bittigau, K., 1994, " Small Area X-Ray Photoelectron Spectroscopy (SAXPS) Analysis of Microscopic Contamination in Semiconductor Manufacturing and Processes," *Vacuum*, Vol. 46, pp. 281–286.

McGuiggan, P.M., and Israelachvili, J.N., 1990, "Adhesion and Short-Range Forces Between Surfaces. Part II: Effects of Surface Lattice Mismatch," *Journal of Materials Research*, Vol. 5, pp. 2232–2243.

Moinpour, M., Tripathi, S., Li, J., and Fardi, B., 1995, "Detecting and Eliminating

Wafer Backside Contamination Sources," *Microcontamination*, Vol. 13, pp. 47–52.

Nielsen, L.E., 1962, **Mechanical Properties of Polymers**, Reinhold Publishing, New York, pp. 12–21.

Parks, H.G., and O'Hanlon, J.F., 1993, "The Evolving Role of Defects and Contamination in Semiconductor Manufacturing," *Microelectronics Journal*, Vol. 24, pp. 313–327.

Raevskii, V.G., 1973, "Some Aspects of the Theory of Adhesive Joints," *Journal of Adhesion*, Vol. 5, pp. 203–210.

Ranade, M., 1987, "Adhesion and Removal of Fine Particles on Surfaces," *Aerosol Science and Technology*, Vol. 7, pp. 161–167.

Savkoor, A.R., and G.A.D., Briggs, 1977, "The Effect of Tangential Force on the Contact of Elastic Solids'," *Proceedings of the Royal Society of London*, Vol. A 356, pp. 103–114.

Schut, J.H., 1992, "Plasma Treatment: The Better Bond," *Plastics Technology*, Vol. 38, pp. 64–72.

Tabor, D., 1977, "Surface Forces and Surface Interactions," *Journal of Colloid and Interface Science*, Vol. 58, pp. 54–66.

Timoshenko, S., and Goodier, J.N., 1951, **Theory of Elasticity**, McGraw-Hill Book Company, New York, pp. 372–377.

Tomlinson, G.A., 1928, "Molecular Cohesion," *Philosophical Magazine*, Vol. 6, pp. 695–712.

Ward, I N.., and Hadley, D.W., 1993, **An Introduction to the Mechanical Properties of Polymers**, John Wiley and Sons, Chichester, p. 12.